Endothelial metabolic response to catecholamine stimulation: towards a metabolic network model of endothelial health

Rósa Sólveig Sigurðardóttir

Thesis for the degree of Master of science
Faculty of medicine
School of health sciences

HÁSKÓLI ÍSLANDS

Efnaskiptasvörun æðaþels við katekólamín örvun: hönnun efnaskiptareiknilíkans fyrir heilsu æðaþels

Rósa Sólveig Sigurðardóttir

Ritgerð til meistaragráðu í Líf- og læknavísindum

Umsjónarkennari: Óttar Rolfsson

Meistaranámsnefnd: Sarah McGarrity og Haraldur Halldórsson

Læknadeild

Heilbrigðisvísindasvið Háskóla Íslands

Júní 2019

Endothelial metabolic response to catecholamine stimulation: towards a metabolic network model of endothelial health

Rósa Sólveig Sigurðardóttir

Thesis for the degree of Master of Science

Supervisor: Óttar Rolfsson

Masters committee: Sarah McGarrity and Haraldur Halldórsson

Faculty of Medicine

School of Health Sciences

June 2019

Prentun: Háskólaprent

Reykjavík, Ísland 2019

Ágrip

Þetta rannsóknarverkefni einblíndi á efnaskipti æðaþelsfrumna (ÆF) og æðaþels-glýkókalixins (ÆG) í áfalla-líkum (*e. trauma-like*) aðstæðum, með það aðalmarkmið að auka skilning á efnaskiptum æðaþels í áfalli. ÆF og ÆG mynda saman innsta borð blóðæða þar sem þau eru í beinni snertingu við blóðrásina og eru sem slík mjög mikilvæg fyrir heilsu æðakerfisins. Vanvirkni í efnaskiptum æðaþelsins stuðlar að framvindu ýmissa æðasjúkdóma, t.d. æðakölkunnar, sykursýki og bráðra sjúkdóma.

Niðurbrot ÆG stuðlar að framvindu æðasjúkdóma, t.d. framvindu áfalls sem einkennist af háum styrk katekólamína í blóði. Þessi aukning veldur niðurbroti ÆG og þar af leiðandi röskun á jafnvægi blóðstorknunarkerfisins sem leiðir til ofþynningu blóðs og aukinnar dánartíðni. Mekanismi ÆG niðurbrots er þekktur að einhverju leiti, en minna er vitað um efnaskipti æðaþelsins við ÆG niðurbrot og lítið sem ekkert er vitað um efnaskiptaferlana sem viðhalda ÆG í áfalli. Sýnt hefur verið fram á að efnaskiptaefni í blóðvökva meðal áfallasjúklinga hefur aðra efnasamsetningu en meðal heilbrigðra viðmiða. Með því að rannsaka efnaskipti æðaþelsins í áfalli og varpa ljósi á óhagstæðar breytingar sem kunna að eiga sér stað myndast tækifæri fyrir jákvæð inngrip sem stuðla að betri útkomu sjúklinga. Betri skilningur á efnaskiptum gæti stuðlað að fyrirbyggingu slæmra efnaskiptaatburða, endurbyggingu eða viðhaldi ÆG og þannig stuðlað að lægri dánartíðni sem tengist niðurbroti ÆG.

Í þessari rannsókn voru áhrif katekólamín örvunar á efnaskipti HUVEC fruma í stöðugri rækt ákvörðuð. Breytingar í efnaskiptum voru ákvörðuð með söfnun og greiningu á efnaskiptasýnum eftir katekólamín örvun. Styrkur efnaskiptaefna var ákvarðaður með ABL mælingum, ensím prófum og massagreiningu. Hraði á nýmyndun efnaskiptaefna var mældur eftir merkingu þeirra með þungum ísótópum og massagreiningu. Einnig voru efnaskipti áfallasjúklinga og heilbrigðra viðmiða greind með notkun aðferða kerfislíffræðinnar og gagnasafna sem innihalda styrki efnaskiptaefna í blóðvökva. Til að meta áhrif efnaskiptaefna í blóðvökva á efnaskipti voru efnaskiptalíkön á erfðamengisskala fyrir áfallasjúklinga og heilbrigð viðmið framleidd og greind m.t.t. efnaskipta.

Katekólamín örvun hægði á virkni glýkólýsu og sítrónusýruhringsins, minnkaði styrk ATP, framkallaði cAMP svar og hægði á nýmyndun auk þess að minnka styrki ÆG forvera. Greining á efnaskiptalíkönum benti til þess að efnaskiptaefni í blóðvökva áfallasjúklinga hefðu óhagstæð áhrif á efnaskipti æðaþelsins.

Við ályktuðum að aukinn styrkur katekólamína meðal HUVEC frumna í rækt hægði á flæði efnaskiptaefna í gegnum aðal efnaskiptaferla, bæði glýkólýsu og sítrónusýruhringinn, auk þess að hafa neikvæð áhrif á nýmyndun ÆG. Við ályktuðum ennfrekar að efnaskiptaefni í blóðvökva áfallasjúklinga hefðu óhagstæð áhrif á efnaskipti æðaþelsins þar sem að greining módelanna sýndi efnaskiptasvipgerðir sem áttu ýmislegt sameiginlegt með þeim efnaskiptabreytingum sem mældust *in vitro* í þessari rannsókn.

Abstract

This thesis is concerned with the metabolism of endothelial cells (ECs) and the endothelial glycocalyx (EGL) in trauma-like conditions, with the overall aim of understanding endothelial metabolism in trauma. The ECs and EGL make up the innermost lining of blood vessels and are in direct contact with the circulatory system and as such are of great importance for vascular health. Dysfunctional endothelial metabolism lies at the crux of many vascular pathologies such as diabetes, atherosclerosis and acute illness.

EGL breakdown contributes to the progression of vascular pathologies such as trauma which is characterized by a high increase in circulatory catecholamines. This increase causes EGL degradation and subsequent disruption of coagulation homeostasis, resulting in profound hypocoagulability and higher mortality rates. The mechanism of EGL breakdown is known to some extent, but less is known about endothelial metabolism in EGL breakdown, let alone the metabolic pathways maintaining the EGL upon this adverse impact. Interestingly, the plasma metabolome of trauma patients has been proven to be different from that of healthy controls. By researching endothelial metabolism in trauma and shedding light on of adverse changes that may take place, the opportunity to intervene and positively affect patient outcomes increases. Better understanding of metabolism could help prevent, rebuild or maintain the EGL structure and thus avoid or decrease the high-mortality associated hypocoagulation.

In this study, we determined effects of catecholamine stimulation on the metabolism of HUVECs in a static culture. Changes in metabolism were determined by catecholamine stimulation and subsequent collection and analysis of metabolic samples. Metabolite concentrations were determined with an ABL machine, enzyme kits and mass spectrometry analysis. Synthesis rates were measured with heavy isotope nutrient labelling and mass spectrometry. We also modelled the metabolism of trauma patients and healthy controls by using systems biology methods and plasma metabolomics datasets. We evaluated the effects of the trauma plasma metabolome on metabolism by generating and analysing *in silico* genome-scale metabolic models of trauma patients and healthy controls.

Catecholamine stimulation decreased glycolytic and TCA cycle activity, decreased ATP concentrations, induced a cAMP response, and decreased synthesis and concentrations of EGL precursors. Metabolic network analysis suggest that the trauma patient plasma metabolome adversely affects endothelial metabolism.

We concluded that increased concentrations of catecholamines in HUVEC cultures slows down flux through key metabolic pathways, both glycolysis and the TCA cycle, and that this negatively impacts EGL synthesis. We further concluded that the plasma metabolomics of trauma patients adversely affect endothelial metabolism by imposing metabolic phenotypes that somewhat resemble those observed *in vitro*.

Acknowledgements

First of all I would like to thank my supervisor, Óttar Rolfsson for outstanding guidance, encouragement and support. I would also like to thank the members of my masters committee, Sarah McGarrity for teaching me about the generation and utilization of metabolic models, and her exceptional guidance and advice in the process, and Haraldur Halldórsson for providing me with cells and guiding me with cell culturing and experiments. I would very much like to thank my lab group and especially Sigurður Trausti Karvelsson and Freyr Jóhansson, for helpful guidance and advice with the metabolic modelling and experiments.

I would like to thank Dr. Pär Ingemar Johansson's team and deCODE genetics for providing me with metabolic datasets used in this thesis and the Landspítalinn for access to their ABL machine. Paulina Cherek at Læknagarður gets special thanks for generating the beautiful TEM images.

It has been the support of my family, friends and especially my boyfriend, Sigurður Ómarsson, that has proven invaluable and kept me going throughout this process and I am forever grateful.

The work of this study was carried out in the Biomedical center facilites at deCODE genetics. I would like to thank the Biomedical center, University of Iceland, and the Center for systems biology. Last but not least I would like to thank the faculty of medicine for accepting this thesis.

Table of contents

List of figures

List of tables

Abbreviations

EC	Endothelial cell
EGL	Endothelial glycocalyx
HUVEC	Human umbilical vein endothelial cell
GAG	Glycosaminoglycan
HS	Heparan sulfate
CS	Chondroitin sulfate
KS	Keratan sulfate
HA	Hyaluronic acid
NO	Nitric oxide
FAO	Fatty acid oxidation
GABA	gamma-Aminobutyric acid
ROS	Reactive oxygen species
eNOS	Endothelial nitric oxide synthetase
AGEs	advanced glycan endproducts
ASGR1	Asialoglycoprotein receptor 1
GEM	Genome-scale metabolic model
COBRA	Constraint based reconstruction and analysis
FBA	Flux balance analysis
MOMA	Minimization of metabolic adjustment
12(S)-HETE	12-Hydroxyeicosatetraenoic acid
15(S)-HETE	15-Hydroxyeicosatetraenoic acid
13(S)-HODE	13-Hydroxyoctadecadienoic acid
13-oxoODE	13-Keto-octadecadienoic acid
14-HDoHE	14-hydroxydocosahexaenoic acid
CECH	gamma-carboxyethyl hydroxychroman
G6P	Glucose-6-phosphate
F6P	Fructose-6-phosphate
PEP	Phosphoenolpyruvate
S1P	Sphingosine-1-phosphate
MTP	Methoxytryptophan

1 Introduction

1.1 The endothelium and the endothelial glycocalyx (EGL)

The endothelium consists of a single layer of endothelial cells (ECs) which cover the innermost lining of blood vessels and constitute a barrier between flowing blood and surrounding tissues. Some decades ago the endothelium was thought of as an inert layer of nucleated cellophane, but this has now been completely disregarded. The endothelium is a key regulator of vascular homeostasis by serving both as a barrier and an active signal transducer for circulating influences. A healthy endothelium responds to chemical and physical signals by producing a broad range of factors that regulate vascular tone, cellular adhesion, blood homeostasis, and vessel wall inflammation(1). Luminally, the ECs are covered by the endothelial glycocalyx (EGL), an intricate network of proteoglycans, glycoproteins and soluble molecules. **Figure 1** shows the EGL schematically and *in vivo* by electron microscopy. In the following sections, the EGL chemical composition, functions, and importance are outlined along with its role in disease.

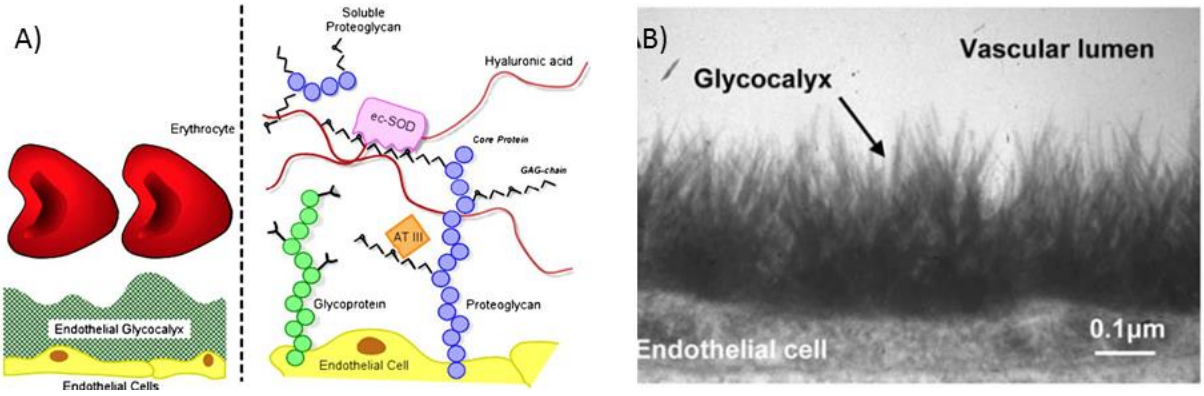

Figure 1: The EGL showed schematically and *in vivo*. (A) *Left:* Schematic representation of the EGL shows its location at the luminal side of the endothelium, forming a barrier between ECs and blood cells. *Right:* Components of the EGL. Proteoglycans with attached GAG chains are bound to the EC membrane. Soluble components like hyaluronic acid, proteoglycans and plasma proteins are embedded into the EGL structure(2). **(B)** An electron microscopy image showing the intact glycocalyx on the luminal side of the endothelial cell(3).

1.1.1 EGL composition

The EGL is a dynamic structure with constant shuffling of membrane-bound molecules and no distinct boundary between locally synthesized and associated elements(2). The main building blocks of the EGL are the proteoglycans which consist of a core protein and glycosaminoglycan (GAG) chains linked to the core protein as presented in **Figure 1**. Core proteins vary in their size, number of attached GAGs and whether or not they are bound to the cell surface. A core protein can contain different types of GAG chains and the GAG chain proportions are likely to change under different circumstances and stimuli. Syndecans, glypicans and perlecans are all examples of core protein groups. The GAG chains are linear polymers composed of varying lengths of disaccharides containing uronic acid and hexosamine sugars. They are modified by sulfation and/or (de)acetylation to a variable extent, the sulfation gives the EGL network a net negative charge. GAG classification depends on the type of uronic acid and hexosamine that is incorporated to the polymer and also on the patterns of

sulfation. The five types of GAGs are heparan sulfate (HS), chondroitin sulfate (CS), dermatan sulfate (DS), keratan sulfate (KS) and hyaluronic acid (HA)(2).

1.1.2 EGL functions and importance

The EGL is located between the blood stream and the endothelium, where it modulates the following barrier functions. It maintains vascular permeability by limiting access of molecules to the EC membrane through steric hindrance and electrostatic charges resulting from the EGLs negative charge(2). The EGL has an important role in controlling extravasation of biological materials and fluids. For example, it has been demonstrated that coronary leak increases after EGL degradation by heparinase in isolated guinea pig hearts(4,5). Furthermore it was demonstrated in a trauma study that high circulating levels of HS, HA and syndecan-1 correlate with increased vascular permeability in human subjects(6). The EGL also influences the blood cell-vessel wall interactions, it repulses red blood cells and platelets from the endothelium and influences leukocyte-vessel wall interactions by sheltering adhesion molecules(2).

The EGL also functions as a mechanotransducer, it has a role in interpreting mechanical forces such as shear stress caused by blood flow into nitric oxide (NO) production(7). It has been demonstrated in cultured ECs that specific breakdown of heparan sulfate GAGs resulted in flawed NO production(8). In the same manner, experiments on canine arteries demonstrated reduced NO production after breakdown of hyaluronan(9).

The EGL has a heterogeneous surface resulting from vast GAG chain variety, mostly caused by GAG chain sulfation patterns and somewhat by GAG length. This surface attaches a lot of plasma-derived molecules which influence the local environment. Take the case of receptors, enzymes and their ligands that bind to the EGL and enable proper signalling or enzymatic functions. Importantly, EGL binding of plasma-derived molecules can lead to local concentration gradients which result in specific biological effects. The binding of some very important anticoagulant mediators illustrate this point, as the binding contributes to the thromboresistant nature of a healthy endothelium which is pivotal for haemostasis. Also, the EGL modulates inflammatory responses by the binding of cytokines and furthermore influences their binding to EC receptors. It is clear that the soluble molecules incorporated into the EGL structure contribute greatly to its functional importance(2).

The important roles of the EGL depend on its structural diversity and as such the integrity of the EGL is of great importance for its functionality and subsequent vascular health. The roles of the endothelium can be summarized as maintaining the barrier between flowing blood and surrounding tissues, mechanotransduction, and embedding of important molecules in its structure such as factors of the blood coagulation system. The perturbations of any of these contributes to what is termed endothelial dysfunction which contributes to multiple diseases of the cardiovascular system.

1.2 Importance of endothelial metabolism

Metabolism is a network of metabolites and metabolic reactions, it represents the biological system that generates the essential components for life. All living organisms maintain a complex network of metabolic routes for the biosynthesis of amino acids, nucleic acids, lipids and carbohydrates, and importantly, for the catabolism of compounds in order to drive cellular processes(10).

EC metabolism has an active role in regulating key endothelial functions. The pivotal role of glycolysis in vessel sprouting is a well-established example, whereas ECs double their glycolytic flux to meet increased biomass and energy demands, and to supply energy for cytoskeletal remodelling(7). Metabolism is also associated with EC vasculoprotective roles. The importance of fatty acid oxidation (FAO) to maintain endothelial barrier functions is becoming increasingly clear. A recent study concerned with how quiescent ECs (QECs) protect themselves against exposure to high oxygen levels in the bloodstream found that when going from proliferative to a quiescent state, ECs reprogrammed their metabolism to increase FAO and subsequently regeneration of NADPH. The NADPH was used by NADPH-consuming enzymes to maintain redox homeostasis, thus supporting barrier integrity(11). An earlier study that utilized proteomics-based metabolic modelling also found that metabolic changes that led to increased EC permeability, like inhibition of carnitine palmitoyltransferase 1A (CPT1A) and decreased FAO were pivotal for endothelial permeability(12). ECs synthesize γ-Aminobutyric acid (GABA) for its vasculoprotective qualities, GABA protects ECs by inhibiting reactive oxygen species (ROS) generation and prevent monocyte adhesion(13), and furthermore it regulates EC key mechanisms of ATP synthesis, fatty acid- and pyruvate oxidation(14).

EC metabolism contributes to endothelial dysfunction and many examples of EC metabolism contributing to disease progression exist. Take the case of perturbations in metabolic pathways generating nitric oxide (NO) and its connection to atherosclerosis. Early atherosclerotic events are characterized by uncoupled and reduced endothelial nitric oxide synthetase (eNOS) activity and subsequent decrease in NO production, increase in ROS formation and the progress of proatherogenic events normally inhibited by NO(7). Another example of EC metabolism in disease progression is that of diabetes, where increased blood glucose levels drastically change EC metabolism. Hyperglycemia causes reduced production of NADPH and subsequent rise in oxidative stress levels, it also obstructs NO production and supports reactive oxygen species (ROS) formation. These metabolic changes can result in DNA strand breaks, accumulation of glycolytic intermediates which end in production of toxic advanced glycan endproducts (AGEs) and accumulation of damaged mitochondria(15). Seeing as how important EC metabolism is for vascular health, it should be considered a very important field of research that should not be overlooked.

Due to the many important roles the endothelium has in maintaining healthy vasculature, its dysfunction lies at the crux of many vascular pathologies. Endothelial dysfunction is associated with most forms of cardiovascular disease, such as hypertension, coronary artery disease, chronic heart failure, peripheral vascular disease, diabetes, and chronic kidney failure(16). Endothelial dysfunction also has a pivotal role in acute critical illnesses such as severe trauma, sepsis, myocardial infarction, and post cardiac arrest syndrome(17).

1.3 EGL metabolism

The metabolism of EGL synthesis is quite well known. Information about its precursors, synthesis reactions, enzymes and cellular compartmentalization is readily available. The first step in proteoglycan synthesis is the translation of a core protein and formation of a GAG primary linker on the protein which takes place in the cytosol and Golgi. Next, GAG chain polymerization takes place by addition of glucuronic acids, using UDP-glucuronate, and glucosamine, using UDP-N-acetylglucosamine(2). Fructose-6-Phosphate, glutamine and acetyl-Coa are required for de novo UDP-N-acetylglucosamine synthesis by the hexosamine pathway(18) and UDP-glucuronate is synthesized from UDP-glucose which is generated from glucose. After polymerization the GAG chain undergoes modifications such as sulfation and epimerization which take place in the Golgi. HA is assembled at the cytosolic side of the EC membrane, using UDP-glucuronate and UDP-N-acetylglucosamine as glycan donors. HA is not modified and therefore does not contain any sulfated groups(2).

1.4 EGL in disease and trauma

Despite knowledge on EGL metabolism, much less is known about the context of EGL metabolism in disease. Given the size and complexity of the structure, the EGL is likely to be metabolically expensive, particularly as it is regenerated quickly after removal and remodelled in response to stimuli such as shear stress(19). Better understanding of EGL metabolism in disease would be of great importance to possibly help rebuild or maintain the structure and thus its important roles for a healthy vasculature.

The EGL structure is compromised in various pathological states due to EGL breakdown or shedding and thus accompanies endothelial dysfunction. The EGLs building blocks are shed from the endothelial surface under various chronic and acute clinical conditions, e.g. ischaemia and hypoxia, sepsis and inflammation, atherosclerosis, diabetes, renal disease and haemorrhagic viral infections(20). The effects of disease on the EGL have been investigated by measuring EGL breakdown products in human plasma. Increased plasma levels of the proteoglycan syndecan-1 have for example been shown to be positively correlated with increased mortality amongst sepsis patients(21) and trauma patients(6,17).

1.4.1 Trauma and catecholamines

Patients experiencing severe trauma experience a shock that causes sympatho-adrenal hyperactivation, resulting in increased circulatory catecholamine levels and hypocoagulability in some cases. Patients with hypocoagulability are reported to have higher mortality rates than their counterparts that don't have hypocoagulability. It has been proposed by Johansson et al that this shock-induced sympathoadrenal hyperactivation is a critical driver of endothelial dysfunction and, supposedly, EGL damage in trauma. They furthermore propose that the compromised EGL and subsequent imbalance in haemostasis induce the profound hypocoagulability observed in these patients(17).

Catecholamines exert their biological effects such as supporting blood sugar maintenance during the fight-or-flight response by binding adrenergic receptors(22). Adrenergic receptors are expressed on ECs(23,24) and important EC functions related to trauma such as (increased) permeability are regulated by catecholamines(25). Catecholamines are known inducers of angiopoietin-2, which is secreted from ECs via Weibel-Palade bodies upon stimulation(26,27) and results in release of heparanase and subsequent EGL breakdown via interference with angiopoietin-1/Tie2 binding(22).

The damage caused by high concentrations of catecholamine on the EGL has been demonstrated in animal models and also *in vitro,* and *in vivo,* in human trauma subjects(28). Members of our lab group have previously carried out *in vitro* experiments on human umbilical vein endothelial cells (HUVECs) which demonstrate the damaging effects catecholamines exert on the EGL. **Figure 2** shows results from these experiments.

As discussed above, the mechanisms of EGL breakdown in disease are known to some extent, e.g. breakdown via enzymes. However less is known about endothelial metabolism following increased circulatory concentrations of catecholamines and EGL breakdown. If and how metabolic pathways change is not known and that is what we wish to elucidate at least in part. Nevertheless, trauma patients are likely to have plasma metabolomics profiles that negatively influence endothelial function.

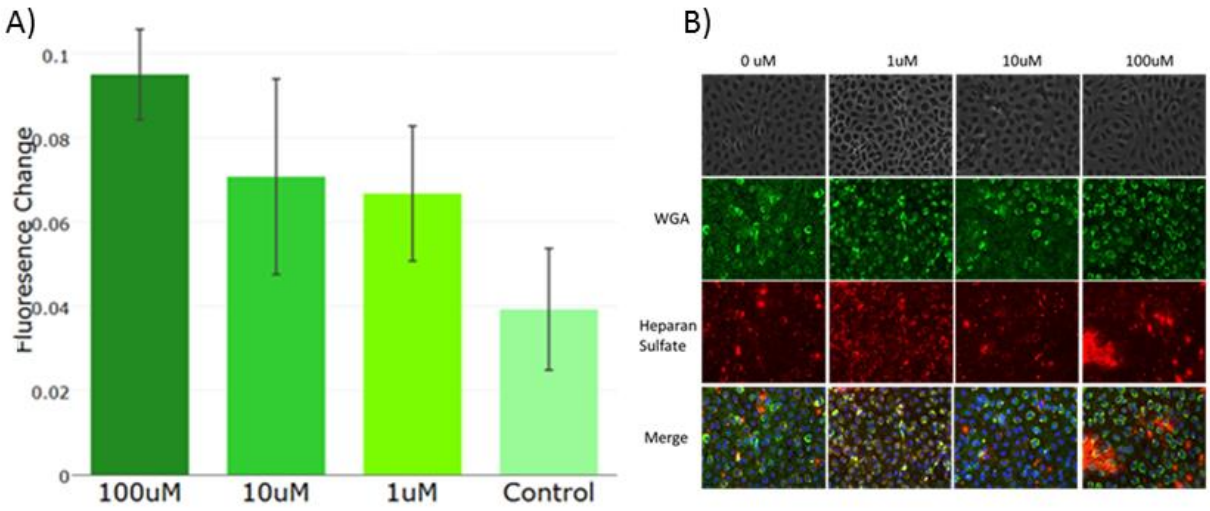

Figure 2: Preliminary data demonstrate the damaging effects catecholamines exert on the EGL and endothelium. HUVEC cells treated with a mix of adrenaline and noradrenaline for 4 hours and effects on the EGL observed. **A)** Endothelial permeability increases with increased catecholamines as observed by flow of fluorescently labelled dextran through cell monolayers. **B)** Light microscopy, unstained cells show greater distance between cells with catecholamine treatment, staining with WGA (green) shows EGL loss with increased catecholamine treatment, HS antibody (red) shows HS loss from cells and accumulation with increased catecholamines. WGA and HS antibody merged with DAPI staining (blue nuclear) summarize the greater disperse of ECs and EGL loss with increased catecholamine treatment.

1.5 ASGR1 variant

The ASGR1 gene encodes the major subunit of the asialoglycoprotein receptor (ASGPR), a lectin that plays a role in the homeostasis of circulating glycoproteins by mediating endocytosis and degradation of desialylated glycoproteins. Recently deCODE genetics identified an ASGR1 variant, a rare

noncoding 12-basepair deletion (del12) in intron 4 of ASGR1 that causes ASGPR to be truncated and prone to degradation. Researchers found an association between the ASGR1 variant, decreased non-high density lipoprotein (non-HDL) cholesterol levels and reduced risk of coronary artery disease. They further concluded that the effect of the ASGR1 variant on coronary artery disease was stronger than that predicted by its effect on circulating non-HDL cholesterol levels alone(29). This suggests that there is an additional mechanism of action for the ASGR1 variant. Given its role in removing glycoproteins it is possible that the vasculoprotective effects observed are due to an increased supply of EGL materials in the bloodstream, available to be imbedded into the EGL. Individuals with the ASGR1 variant could therefore represent a genetic sub-group that possesses an extra healthy endothelium.

1.6 Metabolic systems biology and constraint-based modelling

Endothelial metabolism cannot be investigated directly *in situ.* Trauma patients and ASGR1 del12 carriers however represent patient groups that are likely to have endothelial dysfunction and healthy endothelium, respectively. The plasma profiles of these individuals can be used to estimate endothelial metabolic phenotypes through cell scale metabolic network analysis. In the following sections this methodology is described.

1.6.1 Metabolic systems biology

The main principle of metabolic systems biology is to explore and understand metabolism on a holistic level. Metabolic networks are complex and interconnected by nature. Systems-level computational approaches represent a methodology that can be applied to understand the topology and metabolic flux of nutrients through these networks given that the networks accurately describe all biochemical components of the system. The publication of the first full genome sequence in the mid-1990s opened the possibility to identify all the gene products involved in complex biological processes in a single organism. Metabolic systems biology is built on this genome annotation and the well-studied biochemistry of metabolic activity, that combined makes it possible to reconstruct metabolic networks on a genomic scale(30).

1.6.2 Metabolic reconstructions

One area of metabolic systems biology is focused on metabolite flux analysis, as opposed to static interpretations of presence or absence calls of metabolic components within a pre-defined network. Metabolite flux analysis is dependent upon metabolic reconstructions. A metabolic reconstruction is a list of metabolic reactions that exist within a particular organism and their association with relevant proteins, transcripts and genes(31). RECON1 was published in 2006 and represented the first human whole-genome metabolic reconstruction, it was manually curated and based on both genomic and bibliomic data(32). Since then upgraded versions of RECON have been developed with RECON 3D being the most recent one(33).

1.6.3 Context-specific genome scale metabolic models (GEMs)

In order to analyse context specific metabolism, the metabolic reconstructions are transformed into predictive *in silico* models. That includes extraction of biologically relevant reactions and implementation of constraints that describe the biology of the metabolic subject.

Research in metabolic systems biology often focuses on metabolism in a specific cell type. This requires cell-specific (e.g. endothelial cell) or context-specific (e.g catecholamine stimulation) models. To extract relevant reactions from metabolic reconstructions, transcription data and algorithms such as FASTCORE are used to generate a flux consistent subnetwork that represent the cell type of interest(34). The constraints implemented define the systems boundaries. Boundaries are commonly constraints on metabolite uptake and secretion rates derived from *in vitro* measurements(31). Constrained, cell or context-specific models are commonly abbreviated as genome-scale metabolic models (GEMs). GEMs are available for multiple cell types although these may all be derived from the same reconstruction e.g. RECON 1.

GEMs are mathematically formulated metabolic networks, they contain linked genome and reactome knowledge, meaning they possess relationships between genes, enzymes and metabolites involved in metabolic reactions. **Figure 3** explains the main features of a GEM. A stoichiometric matrix represents the associated reactions and metabolites in the model, where each reaction is represented in a column and each metabolite in a row. This matrix allows the mathematical analysis of metabolic networks(31). The size of this matrix is 2766x3744 in RECON1 and 5063x7440in RECON2.

GEMs provide an *in silico* framework for computational simulation of cellular metabolism. A reliable GEM provides a virtual laboratory for *in silico* experimentation in a convenient, cheap and rapid manner. GEMs have been used to investigate genotype-phenotype relationships, explore the metabolism of disease, for biomarker identification and to identify novel metabolic drug targets, to name a few(35). Cancer-specific GEMs have been developed and used for identification of oncogenes/metabolites and biomarkers for diagnosing specific cancer(36–38). By construction of personalized GEMs, 101 drug targets for liver cancer treatment were identified and thereof 83 are currently in use(39). Insights into the mechanism of non-alcohol fat liver disease(40) and type 2 diabetes(41) have been reported by interpreting clinical data with GEMs. GEMs have been used to study effects of gut microbiota on host(35,42), adipocyte metabolism in obese subjects as compared to normal-weight subjects(43), and endothelial permeability(12). These are only just a few examples of the utilization of GEMs, more examples can be found in a comprehensive review article by Fouladiha and Marashi(44).

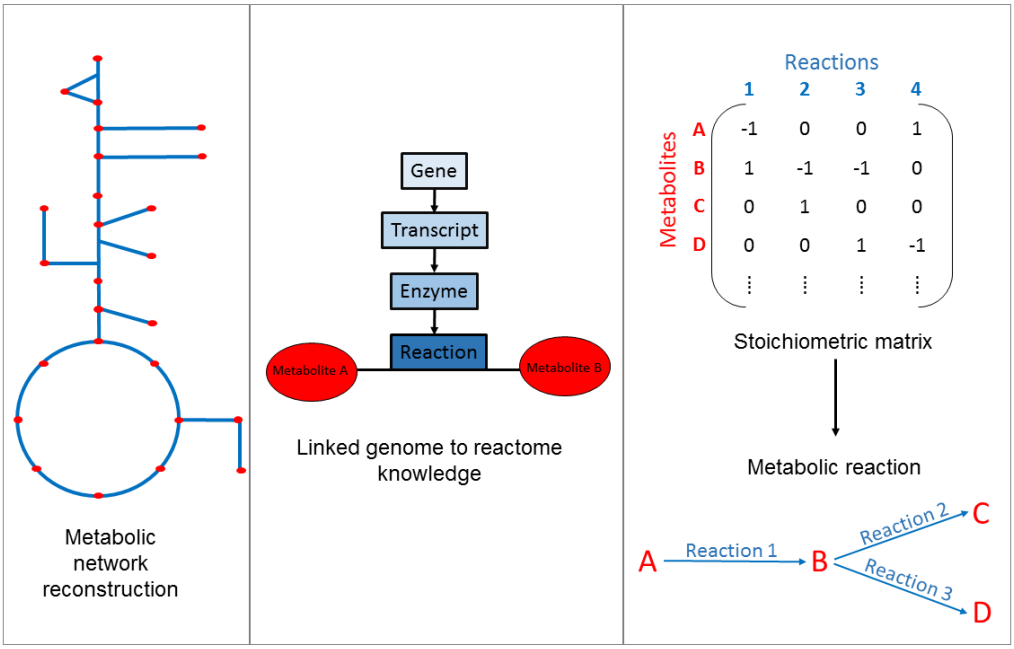

Figure 3: GEMs have linked genome-reactome knowledge that is represented in a stoichiometric matrix. A metabolic network reconstruction contains linked genome to reactome knowledge (left). Gene reaction relationships are contained within reconstructions (middle). The mathematical matrix contains metabolite reaction stoichiometry of all reactions within the network and allows mathematical analysis of metabolism using linear algebra.

1.6.4 Analysis of metabolism via GEMs

Once metabolism of a specific cell or context has been formulated within a GEM, metabolism is analysed within GEMs using a variety of methods. The ones used in this thesis are outlined below. The functions to carry out these methods belong to the constraint-based reconstruction and analysis (COBRA) toolbox(31), a software package which here was used in the Matlab R2017a environment (The Matworks Inc.).

1.6.4.1 Flux balance analysis (FBA) and random sampling

A predictive model has constraints in the form of a stoichiometric matrix, ensuring that the total amount of any compound being consumed must be equal to the total amount being produced, i.e. the system assumes steady state. It also has constraints set in the upper and lower bounds of reactions, defining the minimum and maximum allowable fluxes through reactions. These constraints define the space of allowable flux distributions of a system, also called the *solution space* - that is the rates at which every metabolite can be consumed or produced by each reaction(45).

Flux balance analysis (FBA) is used to analyse the flow of metabolites through a metabolic network by taking these constraints into account. FBA is based on linear optimization and works to optimize a chosen objective function, e.g. the biomass function which allows to predict maximal growth(46). Through the optimization of an objective function, FBA can identify a single optimal flux distribution, or a *flux solution* inside the allowed solution space(45). An FBA solution holds optimized flux values for all reactions within the model under analysis. For example, one could study the differences in an optimal flux distribution solution for maximum possible growth for HUVECs in standard culture conditions as compared to HUVECs treated with catecholamines.

The single optimal solution provided by FBA does not necessarily describe the correct internal state of the cell. This is especially true for cells that are not primarily concerned with growing such as ECs. That is why random sampling is commonly applied as well. It is used to study the entire solution space and gives a *set of feasible flux solutions* that fit within the allowed solution space, thus defining the range of optimal solutions(47). A random sampling solution has flux values for all reactions in multiple sets of solutions and can be subjected to statistical analysis such as calculating the means and standard deviation of flux distributions. The overall aim of random sampling is to extract a more realistic image of metabolism. To continue with the example used above, this method would give a set of feasible flux distributions for HUVECs under standard culture conditions as compared to HUVECs treated with catecholamines.

Simulating fluxes under maximal cell growth isn't necessarily a correct assumption when investigating perturbations in metabolism. While the assumption of growth optimality for a normal, healthy cell is justifiable, the same argument might not apply to metabolism in cells under stress(48).

1.6.4.2 Minimization of metabolic adjustment (MOMA)

To address the problem of growth optimality assumption, the MOMA method was created(48). It was initially designed to analyse gene deletion strains of *E. coli* that had not been exposed to long term evolutionary pressure as the wild type strain. MOMA identifies a point in flux space that comes closest to the wild type point but is also compatible with gene deletion constraints. That being said, it is a convenient method to predict the behaviour of perturbed metabolic networks or in this case metabolic networks representing a patient type whose growth performance is suboptimal(48). MOMA can be used to "push" a control model to be more like a subject model or vice versa. The MOMA solution includes altered flux values for reactions that push the control model to be more like the subject model. The representation of subsystems and genes accompanying the reactions in the solution can be analysed and visualized. Essentially MOMA allows the identification of reactions/genes that require up- or downregulation in order to find an intermediate state between two models. Continuing on with the example above, this method would be used to identify overrepresented subsystems and genes between HUVECs under standard culture conditions as compared to HUVECs treated with catecholamines.

1.6.4.3 Flux enrichment analysis (FEA)

FEA is a subtype of pathway enrichment analysis commonly used in metabolomics and transcriptomic workflows. FEA is performed on the MOMA solution to extract overrepresented subsystems and genes in the solution. Being overrepresented means that out of the genes/subsystems that are altered in the solution, a particular set is more changed than what might happen by chance. FEA returns a list of groups (subsystems or genes), the total set size, an enriched set size, p-value and an adjusted p-value. For example, the total set size of the group 'keratan sulfate degradation' is 75, meaning that 75 reactions belong to this group, and the enriched set size is 12, meaning that in the MOMA solution, 12 reactions out of these 75 are altered. To identify overrepresented groups, the expected representation values and observed representation values of the groups are calculated. Expected representation equals the total set size divided by the total reactions or genes in the model, depending on analysis.

Observed representation equals the enriched set size divided by the value of all enriched set sizes (total reactions/genes that are altered in MOMA). If the observed representation exceeds the expected representation the group is said to be overrepresented. This method would be used to visualize what subsystems and genes were overrepresented in HUVECs under standard culture conditions as compared to HUVECs treated with catecholamines.

2 Aims

The aim of this thesis is to shed light on endothelial and EGL metabolism in trauma by using a combination of methods including *in vitro* catecholamine cell experiments and *in silico* computational trauma simulations, utilizing plasma metabolomics data collected from trauma patients and ASGR1 variant carriers.

2.1 Research questions and objectives

1. **Will increased concentration of catecholamines in HUVEC cultures result in changes to EC metabolism, and particularly, do the catecholamines exert their effects on EGL metabolism?**

We wish to elucidate the metabolic effects that increased catecholamine levels have on EC and EGL metabolism. The metabolic effects following stimulation of HUVEC with catecholamines will be investigated by measurements of extra-, and intracellular metabolites along with their synthesis rates. Intracellular ATP, AMP and cAMP will be measured to investigate the effects of catecholamines on energy and signalling metabolism. To investigate effects on glycolysis, extracellular lactate and glucose will be measured. The TCA cycle will be investigated by measurements of intracellular concentrations of citrate, succinate, malate, L-glutamine and L-glutamate (anaplerotic metabolites). Anaplerotic metabolites will also be measured extracellularly. Synthesis rates of citrate, L-glutamine and L-glutamate will also be measured. The intracellular concentration and synthesis rates of UDP-N-acetylglucosamine and UDP-glucose (EGL precursors) will be measured to observe catecholamine effects on EGL metabolism. Combined these measurements will provide a good overview of change in HUVECs metabolism as a response to catecholamine stimulation.

2. **Will differences in plasma metabolomics between trauma patient and healthy controls account for differences in EC and EGL metabolism?**

Our collaborators have established that there is a difference between the plasma metabolome of trauma patients and healthy controls. If and how the plasma metabolome effects endothelial and EGL metabolism is yet to be answered. We wish to investigate metabolic phenotypes in healthy and dysfunctional endothelium (trauma) by establishing GEMs based on plasma metabolomics. For that we will upgrade our GEM using the concentrations in the metabolic plasma datasets and EGL metabolism. Models for trauma, ASGR1 and healthy controls will be generated and analysed to highlight differences between trauma and healthy controls and ASGR1 variant carriers and non-carriers.

3 Methods

3.1 HUVEC extraction and culturing

HUVECs were isolated from human umbilical cords by Haraldur Halldórsson and grow in 37°C, 5%CO_2 in EGM medium (Lonza) which consists of EBM (Lonza) and EGM-2 Endothelial SingleQuots kit (Lonza). During experiments cells were not subcultured for further use, so each experiment uses HUVECs from different donors.

3.2 Transmission electron microscopy

Cells were grown on glass coverslips (12mm, size1, Heinz Herenz) until 50% confluency in 24 well plates. Cells received 4 different treatments for 4 hours: (1) two control wells (EGM) (2) two wells received 1µM catecholamines, (3) two wells received 10µM catecholamines, and (4) two wells received 100µM catecholamines. After 4 hour treatment the medium was removed and cells were fixed with 300µL 2% glutaraldehyde (Ted Pella, Inc.) in 0.1M Cacodylate buffer (pH 7.4, J.B.EM Services Inc.) for 20 minutes. The fixative was removed and 1mL 0.1M cacodylate buffer was pipetted onto the cells and the cells were refrigerated until sample preparation.

Sample preparation was carried out by Paulina Cherek at Læknagarður. Coverslips were postfixed in 1% osmium tetroxide (J.B.EM Services Inc.) in 0.1M cacodylate buffer for 1 hour, followed by two washes with 0.1M cacodylate buffer 3 minutes each. Cells were dehydrated in series of ethanol: once with 70% ethanol (Gamla Apótekið) for 1 minute, once with 96% ethanol for 1 minute and twice with absolute ethanol for 1 minute. Next, each coverslip was dipped in acetone for a few seconds and placed on an aluminum dish (Sigma-Aldrich). Immediately after, a drop of resin (Spurr Resin - Ted Pella, Inc.) was poured on top of the coverslip covering the cells. Gelatin capsule was filled with resin and put upside down on top of the cells to create a block. Samples were incubated at room temperature for 2 hours to allow the resin to infiltrate the cells. Blocks were baked overnight in a 70°C oven. After cooling down, resin blocks were separated from coverslips by dipping them for a few seconds in liquid nitrogen. Blocks were trimmed with trimming tool (Leica EM Trim 2) and then ultra-thin (100nm) sections were cut with a diamond knife (45° Diatome) on an Ultramicrotome (Leica EM UC7) and placed on copper grids (Ted Pella, Inc.). Grids were post-stained with uranyl acetate (0,5% in distilled water, (J.B. EM Services Inc.) for 30 minutes and with lead citrate (3% Ultrostain 2, Leica) for 1 minute. Sections on grids were imaged using a JEM-1400PLUS PL Transmission Electron Microscope at various magnifications.

3.3 Metabolic catecholamine stimulation experiments

Experiments involved addition of catecholamine's (and catecholamines + heavy isotope nutrient labelling) to HUVEC cultures and subsequent metabolic sample collection (intracellular and extracellular) after 4h and 24h after catecholamine stimulation. Collection of baseline samples was carried out beforehand. Extracellular (medium) samples were analysed with ABL 800 (Radiometer) to measure glucose and lactate concentrations, and with absorbance assays (Megazyme) to measure

glutamine and glutamate concentrations. Intracellular samples were analysed with mass spectrometry (Waters) to measure various intracellular metabolites.

3.3.1 Stimulation with catecholamine's

HUVECs were seeded to the 4 corner wells in 6-well plates (to secure equal evaporation), to 36 wells in total and incubated in 37°C, 5% CO_2. When cells reached confluency (defined as 0h) they were treated with one of four treatments: (1) Eight controls wells with 0µM catecholamines (just EGM medium), (2) eight wells received 0,5µM catecholamines in EGM, (3) eight wells received 5µM catecholamines in EGM, and (4) 8 wells received 50µM catecholamines in EGM. The remaining four wells were baseline samples which represented a 0h timepoint and received no treatment.

Metabolic samples were collected at 0h (baseline samples) 4 hours and 24 hours after catecholamine stimulation. In all cases, cells were counted, and extra- and intracellular samples were stored. Cells were counted using a haemocytometer. Extracellular samples for 4h and 24h were collected by storing medium from cells before methanolcollection was carried out. Extracellular baseline samples are the treatment media mentioned above before any contact with the cell culture. Intracellular samples were collected by methanolcollection: medium was removed and cells were quickly washed two times with PBS. 1mL of 80% ice cold methanol was pipetted onto cells, cells were collected to the side of the well with a cell scraper and pipetted to an Eppendorf tube along with the ice cold methanol. All samples were stored at -80°C. **Figure 4** explains the setup of the experiment.

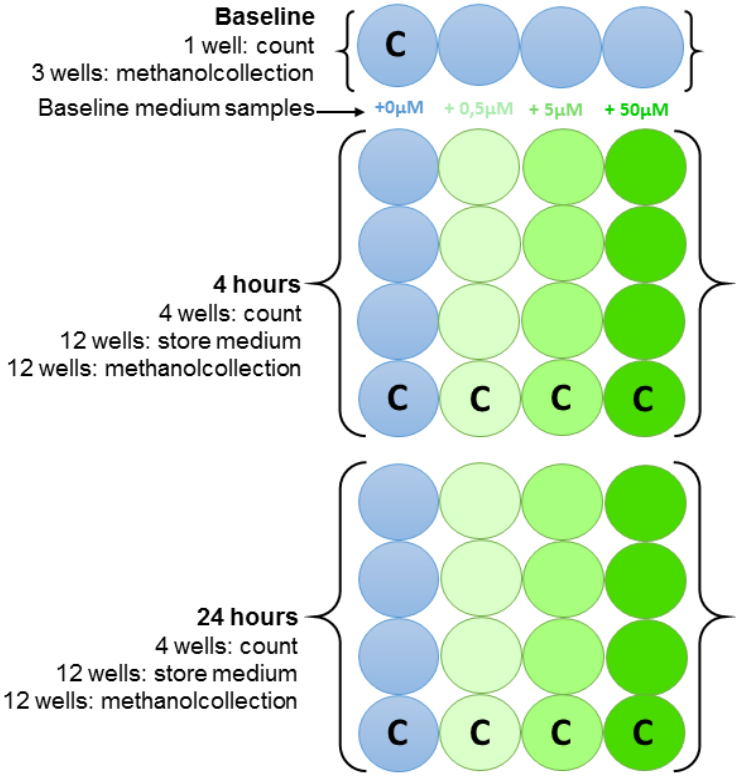

Figure 4: Setup of a metabolic catecholamine stimulation experiment. The figure shows how the baseline, 4 hour and 24 hour samples are collected and the concentrations of the catecholamine solutions added (increased catecholamine = wells are more green).

3.3.2 Stimulation with catecholamine's and heavy isotope nutrient labelling

This experiment has the same setup as the catecholamine stimulation experiment, except for the treatments which were: (1) 0µM catecholamines (EGM), (2) 0µM catecholamines + labelled molecule, (3) 0,5µM catecholamines + labelled molecule, and (4) 5µM catecholamines + labelled molecule. All samples were collected and stored in the same manner. One experiment was carried out using 98% $^{15}N_2$-glutamine (Cambridge Isotope Laboratories) and another using 99% $^{13}C_6$-glucose (Cambridge Isotope Laboratories).

3.3.3 Catecholamine solutions

Catecholamine solutions were equimolar epinephrine/norepinephrine solutions. They are mixed in the following manner: 18,3mg epinephrine (Sigma) was dissolved in 2mL 1M HCl solution (1000µM epinephrine) and 16,9mg norepinephrine (Sigma) was dissolved in 2mL 1M HCl solution (1000µM norepinephrine). 10µL from each 5000µM solution were diluted to 10mL EGM (1000x dilution) making a 50µM equimolar solution of epinephrine/norepinephrine. Serial dilutions to mix 5µM and 0,5µM epi/norepi solutions: 1mL of 50µM solution was diluted to 9mL EGM = 5µM epi/norepi solution and 1mL 5µM epi/norepi solutions was diluted to 9mL EGM = 0,5µM solution.

To mix labelled catecholamine solutions, 0,02763g $^{13}C_6$-glucose or 0,03999g $^{15}N_2$-glutamine were weighed into 27mL EGM, thereof 9 mL were used for EGM + labelled molecule, 9mL were used for 0,5µM catecholamines + labelled molecule, and another 9 mL for 5µM catecholamines + labelled molecule. 10mL EGM with 50µM catecholamines was prepared like described above and 1mL serially diluted into the already labelled 9mL EGM solutions to make 5µM epi/norepi + labelled molecule and 0,5µM epi/norepi + labelled molecule.

3.3.4 Intracellular metabolic measurements

Intracellular metabolic samples were collected with methanolcollection and kept in -80°C like described above. Samples were prepared for the mass spec in the following way: 30uL of Internal Standards mix prepared within the lab added to each sample, 5 minute vortexing until sample looks homologous, centrifugation at full speed (4°C) for 15 minutes. The supernatant was transferred to a new tube (TUBE 1) and 500µL of ice-cold MeOH:H_2O (7:3) was added to the remaining pellet, 5 minute vortexing and centrifugation at full speed (4°C) for 15 minutes, the supernatant was transferred to TUBE 1 and the precipitate thrown away. Samples were dried using the miVac QUATTRO concentrator (Genevac) until all liquids had evaporated. The dried down pellet was reconstituted in 300µL H_2O:Acetonitrile (1:1) and vortexed until fully dissolved. The samples were filtered using a 96-well protein precipitation plate (Pierce) by centrifugation at 2000rpm for 30 minutes. Samples were stored in -80°C before mass spectrometer analysis.

The instrumentation used for mass spec analysis was an ACQUITY UPLC system (UPLC ACQUITY, Waters Corporation, Milford, MA) coupled to a qTOF mass spectrometer (Synapt G2 HDMS, Waters Corporation, Manchester, U.K.) with an electrospray interface (ESI). The gradient chromatographic separation was performed on an ACQUITY BEH Amide (2.1 mm × 150 mm, 1.7 µm particle size, Waters Corporation) at 45°C. Mobile phase A was acetonitrile/ammonium bicarbonate

(10mM) 95:5 and mobile phase B was ammonium bicarbonate (10mM) /acetonitrile 95:5. Injection volume was 7.5 µL, flow rate was 0.4 mL/min and run time was 14 min. The following gradient pattern (solvent B) was used: 0 min, 1% B; 0.1 min, 1% B; 5 min, 58% B; 6 min, 40% B; 7 min, 1% B; 14 min, 1% B. Negative (-) ESI mode was acquired for all samples. The capillary and cone voltage were 1.5 kV and 30 V, respectively. The source and desolvation temperature were 120 and 500 °C, respectively, and the desolvation gas flow was 800 L/h.

3.3.5 Extracellular metabolite measurements

Extracellular metabolic samples were collected and stored in -80°C like described above. Glucose and lactate concentration were measured on the ABL 800 (Radiometer). L-glutamine concentration was measured using the L-glutamine/Ammonia kit (Megazyme), following the microplate assay procedure as outlined in the included pamphlet. A modification was made for calculations, the absorbance of NH_4^+ was not subtracted from the absorbance of glutamine as advised, since the sample is EGM media that has a buffer system. L-glutamate concentration was measured using the L-glutamic acid kit (Megazyme), following the microplate assay procedure like outlined in the included pamphlet. L-glutamine and L-glutamate samples were measured using the SpectraMax M3 spectrometer and the accompanying software, SoftMax Pro 6.1 (Molecular Devices).

3.4 Metabolic datasets

The metabolic datasets used in this study show measurements of metabolites obtained from human blood plasma. The datasets are comprised of *fold changes* for every metabolite, meaning that they represent the difference in metabolite concentrations between subject and control groups.

3.4.1 Trauma dataset

The trauma dataset was obtained from Dr. Pär Ingemar Johannson at the Righospitalet in Copenhagen, Denmark who has been studying plasma profiles in acute critical illness(17). The values in the dataset were obtained from UHPLC-MS measurements of plasma samples from 20 trauma patients admitted to a level 1 Trauma center and 20 age and gender matched healthy volunteers. The dataset has fold differences for 65 metabolites between trauma patients and matched controls. Two metabolites had the same KEGG ID (C00219, C06428) and were regarded as the same metabolite, leaving 64 metabolites for analysis. Thereof 57 metabolites were used to constrain the model.

3.4.2 ASGR1 dataset

The ASGR1 dataset was obtained from deCODE genetics. The dataset includes fold differences for 149 metabolites that are significantly different ($p<0.05$) between ASGR1 variant carriers and matched controls. Included were values of unknown metabolites that were not used in this thesis. The dataset also included values for various types of triacylglycerols (n=64), phosphatidylethanolamines (n=10), and lysophosphatidylcholines (n=9) that were not used since the model does not differentiate between different structural types of the lipid groups. Fortunately, the dataset did have measurements for total values of triacylglycerols and lysophosphatidylcholines that were used. Unfortunately it did not include a “total” measurement for phosphatidylethanolamines, so the two values with the lowest p-values

(0,0169 and 0,0172) which are ester type phosphatidylethanolamines were used by averaging out the fold changes. After excluding these unusable values, 44 metabolites were left for analysis. Thereof 18 metabolites were used to constrain the model.

3.5 Upgrade and refinement of iEC2812

The base model (iEC2812) was generated by Sarah McGarrity and has already been used to study metabolic changes accompanying endothelial dysfunction(49). The upgrade of iEC2812 was carried out in two parts, which involved (1) addition of metabolites, reactions and genes making the model fit to analyse the datasets mentioned above and (2) Incorporation of EGL synthesis.

3.5.1 Incorporating trauma and ASGR1 metabolites

The metabolites in the datasets needed to be available in the model along with their accompanying exchange reactions to enable metabolic analysis which relies on constraining upper and lower bounds of exchange reactions.

To connect a metabolite to iEC2812, its synthesis and exchange reactions were identified and added to the model. Reactions were identified using metabolic datasets like the KEGG (Kyoto Encyclopaedia of Genes and Genomics) PATHWAY Database(50) and BiGG (biochemical, genetic, and genomic) models(51). When reactions had been identified, MATLAB R2017a (Mathworks) and the COBRA Toolbox package(52) were used to add reactions to the model, the COBRA Toolbox *addReaction* function was used. In summary, the steps to connect a metabolite to the model are (1) reaction identification, (2) listing of reactions and metabolites, and (3) addition of metabolites and reactions.

Figure 5 explains the process of identifying and connecting the metabolite 12HETE (12-Hydroxyeicosatetraenoic acid) to the model. First, an upstream precursor of 12HETE was identified using metabolic databases and literature search, which in this case was arachidonic acid, a metabolite already included in the model. ALOX12 is a reaction that consumes arachidonic acid to synthesize 12HPETE (12-Hydroperoxyeicosatetraenoic acid). Next the reaction 12HETE1 transforms 12HPETE to 12HETE, which is then transported via the reaction 12HETEt1 from the cytosol the extracellular space. To allow metabolite exchange, the exchange reaction EX_12HETE was added. Identification and addition of these metabolites and reactions allows the model to synthesize and export 12HETE.

1. Reaction identification: Metabolic databases

KEGG REACTION: R01596 Help

Entry	R01596 Reaction
Name	arachidonate:oxygen 12-oxidoreductase
Definition	Arachidonate + Oxygen <=> 12(S)-HPETE
Equation	C00219 + C00007 <=> C05965

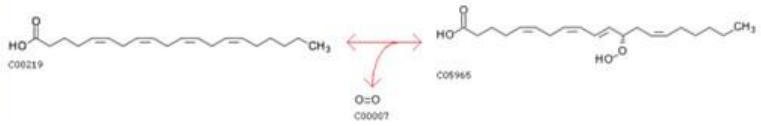

2. List of reactions to add: Microsoft excel

Reaction name	Reaction formula	Status
ALOX12	O2[c]+arachd<=>12HPETE[c]	Added
12HETE1	12HPETE[c] -> 12HETE[c]	Added
12HETEt1	12HETE[c] <=> 12HETE[e]	Added
EX_12HETE	12HETE[e] ->	Added

3. Add reactions: MATLAB & COBRA Toolbox

```
modelstart = modelUFinal;
model = addReaction(modelstart,'ALOX12',{'o2[c]','arachd[c]','12HPETE[c]'},
[-1 -1 1],true,-1000,1000,0,'Arachidonic acid metabolism');
model = addReaction(model,'12HETE1',{'12HPETE[c]','12HETE[c]'},
[-1 1],true,-1000,1000,0,'Arachidonic acid metabolism');
model = addReaction(model,'12HETEt1',{'12HETE[c]','12HETE[e]'},
[-1 1],true,-1000,1000,0,'Arachidonic acid metabolism');
model = addReaction(model,'EX_12HETE',{'12HETE[e]'},[-1],
true,-1000,1000,0,'Arachidonic acid metabolism');
```

Figure 5: The process of connecting a metabolite to a metabolic model. Image shows that reaction identification is done using databases, how the reactions are listed and how a code is written in MATLAB using the COBRA Toolbox function *addReactions*, adding metabolites and reactions to the model.

3.5.2 Incorporating EGL synthesis

3.5.2.1 EGL building blocks and ratios

An EGL review article published in 2006 that has been cited over 200 times(2) was used to identify which building blocks should be included in the EGL. The building blocks identified and their metabolism were explored in the whole genome reconstruction RECON 2.2(53), which showed that some building blocks had more than one subtypes. After building block identification, the different subtypes, precursors and accompanying reactions were identified and added to the model using the method outlined in **Figure 5**. After doing so, EGL synthesis still had some gaps. Therefore a list of missing EGL reactions was generated by comparing reactions in the model to reactions in iCHOv1(54). This list of missing reactions (genes) was compared to transcriptomic data originally used to generate iEC2812, reactions intersecting both lists were inspected and relevant reactions added to the model. To finalise EGL synthesis, some manual curation took place, e.g. the exploration of dead ends in the model and the incorporation of dolichol synthesis which was a necessary downstream pathway for KS synthesis. Finally, primary linkers (core proteins), such as discussed in chapter 1.1.1

were added to the model via sink reactions. Sink reactions are used for metabolites produced in reactions outside the scope of the system, in this case the cytosolic translation of a core protein that GAG chains are linked to. The GAGs, their primary linkers, the linker names and the sink reactions are outlined in **Table 1**.

Table 1: Primary linkers added to the model with sink reactions. The GAG types are listed, KSII core-2 and core-4 have the same type of primary linker (O-glycosylation). KSI has a separate primary linker (N-glycosylation). HS and CS have the same type primary linker.

GAG type	Primary linker	Linker name	Sink reaction
KSII core 2 & 4-linked	Ser/thr[r]	Protein linked Ser or Thr residue (O-glycosylation site)	Ser/thr[g] <=>
KSI	Asn-X-Ser/Thr[r]	Protein linked asparagine residue (N-glycosylation site)	Asn-X-Ser/Thr[r] <=>
HS & CS	Ser-Gly/Ala-X-Gly[r]	Protein linked serine residue (GAG attachment site)	Ser-Gly/Ala-X-Gly[r] <=>

When the synthesis of all building blocks and other necessary metabolites had been added to the model, the ratios of each building block in the EGL was estimated from literature review. In total, 11 studies on GAGs were read(55–65) and the results interpreted into building block ratios.

3.5.2.2 EGL synthesis reaction

When the ratios of building blocks had been decided, a reaction that synthesizes the EGL was designed manually and added to the model using the methods already explained.

3.5.2.3 Incorporation of EGL to the biomass function

The biomass function includes the metabolites necessary for synthesis of cell biomass and their stoichiometry. The last step of EGL incorporation to iEC2812 was its integration to the biomass function, making its synthesis necessary for cell survival.

Before integration to the biomass function, EGL weight proportion out of the total biomass weight was estimated. To do so, values for endothelial cell size and EGL size were found and used to estimate the EGL weight proportion. Further calculations were carried out to estimate the EGL biomass weight in grams per. dry weight (g/DW). The EGL was added to the biomass function using MATLAB and the COBRA Toolbox functions *addReaction* and *changeObjective*.

3.6 Modelling of endothelial metabolism in trauma patients and ASGR1 carriers models

Models representing trauma and ASGR1 metabolism were generated after completion of the model upgrade. Models were generated from the final version of the upgraded model, iEC2997.

3.6.1 Trauma and ASGR1 model generation

To study differences in metabolism, models were generated for both subjects and controls. Two trauma models were generated, one for trauma patients and another for controls. Two ASGR1 models were generated, one for ASGR1 carriers and another for controls. Models representing trauma and ASGR1 metabolism were generated using the same method. The generation of these models is explained in the following text and **Figure 6** presents an explanatory overview of model generation.

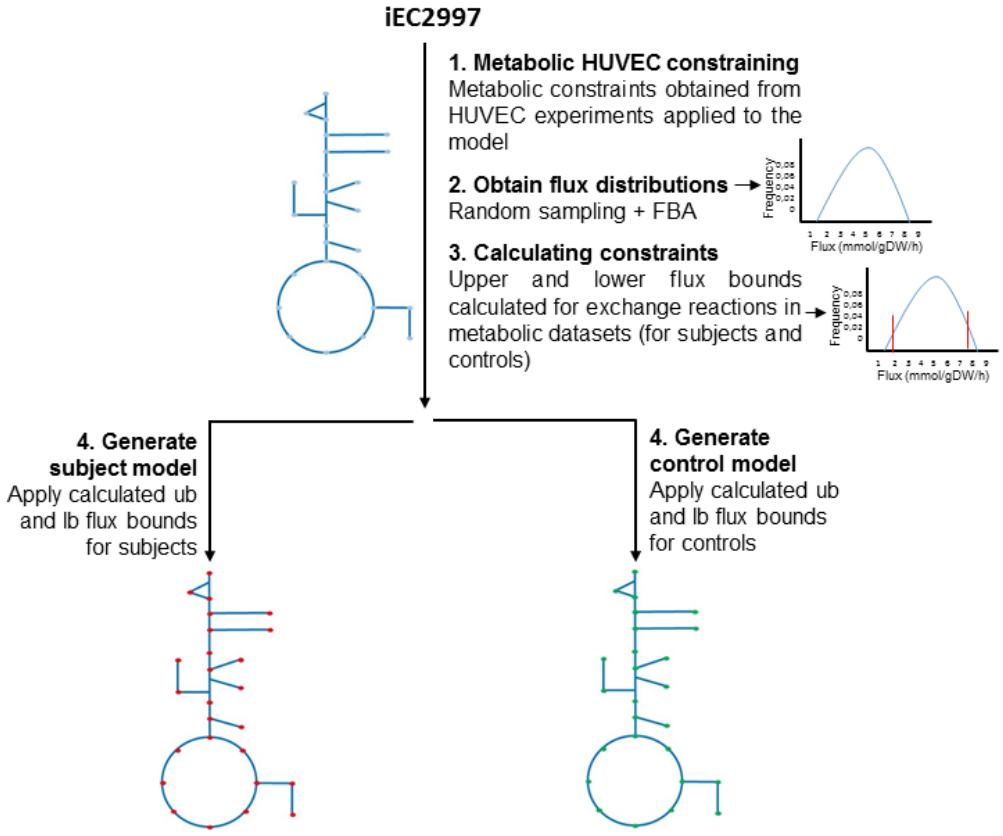

Figure 6: The process of subject and control model generation. iEC2997 is constrained using HUVEC constraints, next random sampling with >50% FBA is carried out to obtain feasible flux distributions of the network and then upper and lower bounds are calculated from the flux distribution of 57 exchange reactions that represent metabolites in the trauma dataset. These upper and lower bounds are imposed on the model to generate trauma patient and control models.

Step. 1, metabolic HUVEC constraining: The first step of generating models was to apply metabolic constraints to 18 exchange reactions in iEC2997, they were applied using MATLAB and the COBRA Toolbox function *changeRxnBounds*, where upper bounds (ub) and lower bounds (lb) from an

already constrained model were used. The constraints are originated from metabolic HUVEC experiments, carried out by Ósk Anufuoro within the lab.

Step. 2, obtain flux distributions: Random sampling (5000 points) was carried out on the constrained iEC2997 in MATLAB using the COBRA functions *optimizeCbModel* and *gpSampler*, obtaining feasible flux distributions for the metabolic network.

Step. 3, calculating constraints: Upper and lower quartiles of the flux distributions for exchange reactions in the metabolic datasets were calculated in MATLAB in the unit mmol/grams dry weight/hour. The upper and lower quartiles from these calculations were interpreted as the ub and lower bounds lb of the reactions for the control models. Corresponding values for subjects were calculated by multiplying the ub and lb control values by the fold change value of the metabolite/exchange reaction in question in the metabolic dataset. **Table 2** shows these calculations and **Figure 7** explains how ub and lb are decided from a random sampling flux distribution.

Table 2: Example of calculations for upper and lower flux bounds. The fold change of pyruvate between healthy controls and trauma patients is 1,5336 and EX_pyr(e) is the exchange reaction for pyruvate. The calculated lb and ub for controls are -14,3217 and 21,1808 mmol/gDW/hour, respectively. Patient bounds are calculated by multiplying the control ub and lb by the fold change.

Metabolite	Fold change	EX reaction	Control lb	Control ub	Patient lb	Patient ub
Pyruvate	1,5336	EX_pyr(e)	-14,3217	21,1808	-21,9642	32,4836

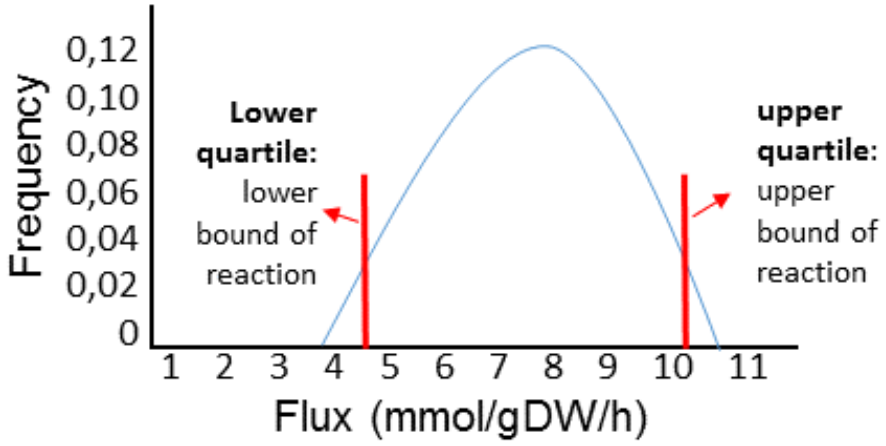

Figure 7: Upper and lower quartiles of a random sampling flux distributions represent the upper and lower bounds of exchange reactions. Figure shows a flux distribution of a reaction obtained from 5000 points random sampling (blue curve). The x-axis shows the flux unit in mmol/grams per dry weight/hour and the y-axis shows the frequency of a given flux value, therefore the highest point of the flux distribution represents the most common flux value of a given reaction. The upper quartile of the distribution represents the reactions upper bound and the lower quartile represents its lower bound. In this figure, the upper flux bound would be 10 mmol/gDW/hour and the lower flux bound would be 4,5 mmol/gDW/hour.

Step. 4, generation of control and subject (trauma and ASGR1 variant carriers) models: In the final step of model generation, calculated ub and lb values were incorporated to the models using MATLAB and the COBRA Toolbox function *changeRxnBounds*, generating control models from control values and subject models from subject values. To generate the trauma models, ub and lb values of 57 exchange reactions were calculated and used as constraints, **Table 3** lists these reactions. To generate the ASGR1 models, ub and lb values of 18 exchange reactions were calculated and used as constraints, **Table 4** lists these reactions. See supplementary appendix 1 for codes, metabolic HUVEC constraints, and calculations of lb and ub.

Table 3: A list of the 57 exchange reactions constrained to generate trauma and healthy control models, and accompanying metabolites. The lists of exchange reactions are presented in two columns for space saving reasons.

Exchange reaction	Metabolite	Exchange reaction	Metabolite
EX_pyr(e)	Pyruvate	**EX_12(13)DHOME**	DiHOME12
EX_dmgly	N-dimethylglycine	**EX_13oODE**	DE13
EX_fume	Fumaric acid	**EX_thr_L(e)**	Threonine
EX_PCRN	Propionylcarnitine	**EX_male**	Malic acid
EX_lnlnca(e)	α-Linolenic acid	**EX_ser_L(e)**	Serine
EX_pmtleice	Palmitic acid	**EX_phe_L(e)**	Phenylalanine
EX_12HETE	HETE12	**EX_tyr_L(e)**	Tyrosine
EX_crvnc(e)	DHA	**EX_succ(e)**	Succinic acid
EX_ile_L(e)	Isoleucine	**EX_leu_L(e)**	Leucine
EX_dcsptn1(e)	Docosapentaenoic	**EX_OCCrn**	Octanoylcarnitine
EX_5oxoe	Oxoproline	**EX_ACRNT**	Acetylcarnitine
EX_his_L(e)	Histidine	**EX_hxan(e)**	Hypoxanthine
EX_cit(e)	Citric acid	**EX_prostge2(e)**	ProstaglandinE2
EX_glu_L(e)	Glutamic acid	**EX_pmtcrne**	Palmitoylcarntine
EX_trp_L(e)	Tryptophan	**EX_met_L(e)**	Methionine
EX_lkynre	Kynurenine	**EX_pro_L(e)**	Proline
EX_lys_L(e)	Lysine	**EX_crne**	Carnitine
EX_13HODE	HODE13	**Ex_lac-L[e]**	Lactate
EX_sphs1p(e)	Sphingosine	**EX_dlnlcg(e)**	DihomoLinolenic
EX_gly(e)	Glycine	**EX_lnlncg(e)**	Linoleate
EX_gln_L(e)	Glutamine	**EX_ASPe**	Aspartic acid
Ex_glc-D[e]	Glucose	**Ex_cys_L[e]**	Cystine
EX_ala_L(e)	Alanine	**EX_akge**	α-Ketoglutarate
EX_arg_L(e)	Arginine	**EX_urate(e)**	Uric acid
EX_c4crn	Butyrylcarnitine	**EX_arachd(e)**	Arachidonic acid
EX_15HETE	HETE15	**EX_val_L(e)**	Valine
EX_hdca(e)	Hexadecenoic	**EX_ocdca(e)**	Octadecenoic acid
EX_lnlc(e)	Linoleic acid	**EX_adn(e)**	Adenosine
EX_adrn(e)	Adrenic acid		

Table 4: A list of the 18 exchange reactions constrained to generate ASGR1 variant carrier and non-carrier models, and accompanying metabolites.

Exchange reaction	Metabolite
EX_gly(e)	Glycine
EX_ins(e)	Inosine
EX_bilirub(e)	Bilirubin
EX_glyc	Glycerol
EX_lpchol_hs(e)	Lysophosphatidylcholine
EX_creat(e)	Creatine
EX_dhcrm	Dihydroceramide
EX_sphs1p(e)	Sphingosine 1-phosphate
EX_sphings	Sphingosine
EX_pchol_hs(e)	Phosphatidylcholine
EX_arg_L(e)	Arginine
EX_asn_L(e)	Asparagine
EX_glyc3p	Glycerol 3-phosphate
EX_pe_hs(e)	Phosphatidylethanolamine
EX_cholp	Choline phosphate
EX_asp_L(e)	Aspartate
EX_tag_hs(e)	Triacylglycerol
EX_gsn(e)	Guanosine

3.6.2 Model analysis

When the model generation was completed the models were analysed. This analysis involved comparing the subject models to the control models to see how the metabolism is different. Various methods were used for this purpose and they are explained in the following text.

3.6.2.1 Calculation and analysis of reaction flux values

To obtain feasible flux distributions, random sampling was performed using the COBRA toolbox function *gpSampler* under the conditions of fulfilling at least 50% of an FBA solution. The flux distributions obtained were used to compare the flux of reactions between control and subject models.

The flux distributions obtained were utilized to analyse what reactions had been upregulated, downregulated or reversed between controls and patients. To allow comparison of flux values, the mean flux values of all reactions in all models were calculated in MATLAB. Next, the mean flux values of subjects were divided by the mean flux values of controls and the outcomes were interpreted as shown on **Figure 8**. These analysis resulted in lists of reversed, up- and downregulated reactions in subjects as compared to controls and vice versa.

$$\frac{subject\ mean\ flux}{control\ mean\ flux} < 0 = reversed\ reaction$$

$$\frac{subject\ mean\ flux}{control\ mean\ flux} > 100 = reaction\ upregulated\ at\ least\ by\ 100x\ in\ subjects$$

$$0 < \frac{subject\ mean\ flux}{control\ mean\ flux} < 0{,}01 = reaction\ downregulated\ at\ least\ by\ 100x\ in\ subjects$$

Figure 8: Calculations for comparisons of flux values. Calculations for interpretation of upregulation, downregulation and reversed reactions between subjects and controls. Values <0 represent reversed reactions, values >100 represent upregulated reactions and values between 0< and <0.0 represent downregulated reactions.

The flux distributions obtained from random sampling were used for plotting flux histograms that visually show flux distributions of reactions. A single histograms contains the flux distribution of the same reactions from two models and therefore allows visual comparison of reaction fluxes. The histograms were made in MATLAB using the COBRA Toolbox function *automaticFigureExport*, an altered version of the function *plotSampleHist*, generated by Sigurður Trausti Karvelsson. These histograms were used to generate a flux image showing what reactions are more active in controls or subjects. The flux image was manually generated using Microsoft PowerPoint.

3.6.2.2 Minimization of metabolic adjustment (MOMA)

MOMA was performed in MATLAB using the COBRA Toolbox function *MOMA*. The control models were pushed to be more like the patient models, which gave a MOMA solution that holds altered flux values to fulfil that purpose. Essentially MOMA allows reactions/genes that require up- or downregulation in order to identify an intermediate state between two models.

3.6.2.3 Flux enrichment analysis (FEA)

FEA was performed in MATLAB using the Cobra Toolbox function *FEA*. FEA was performed on the MOMA solution to search for overrepresented subsystems and genes in the MOMA solution. To identify overrepresented groups, expected and observed representation values were calculated like explained in chapter 1.6.4.3.

4 Results

4.1 Effects of catecholamines on the EGL phenotype

The EGL was imaged after 4 hours of catecholamine stimulation to determine if addition of catecholamines would affect the EGL phenotype of HUVECs in static culture.

4.1.1 TEM images show EGL reduction after catecholamine stimulation

Figure 9 shows loss of EGL structure with catecholamine stimulation. The loss can be seen in the reduction of the lighter structure on the outer rim of the cells. The EGL is long and easily observed after 4 hours of no catecholamine treatment, whereas after 4 hours of 100µM catecholamine treatment, the EGL is much shorter.

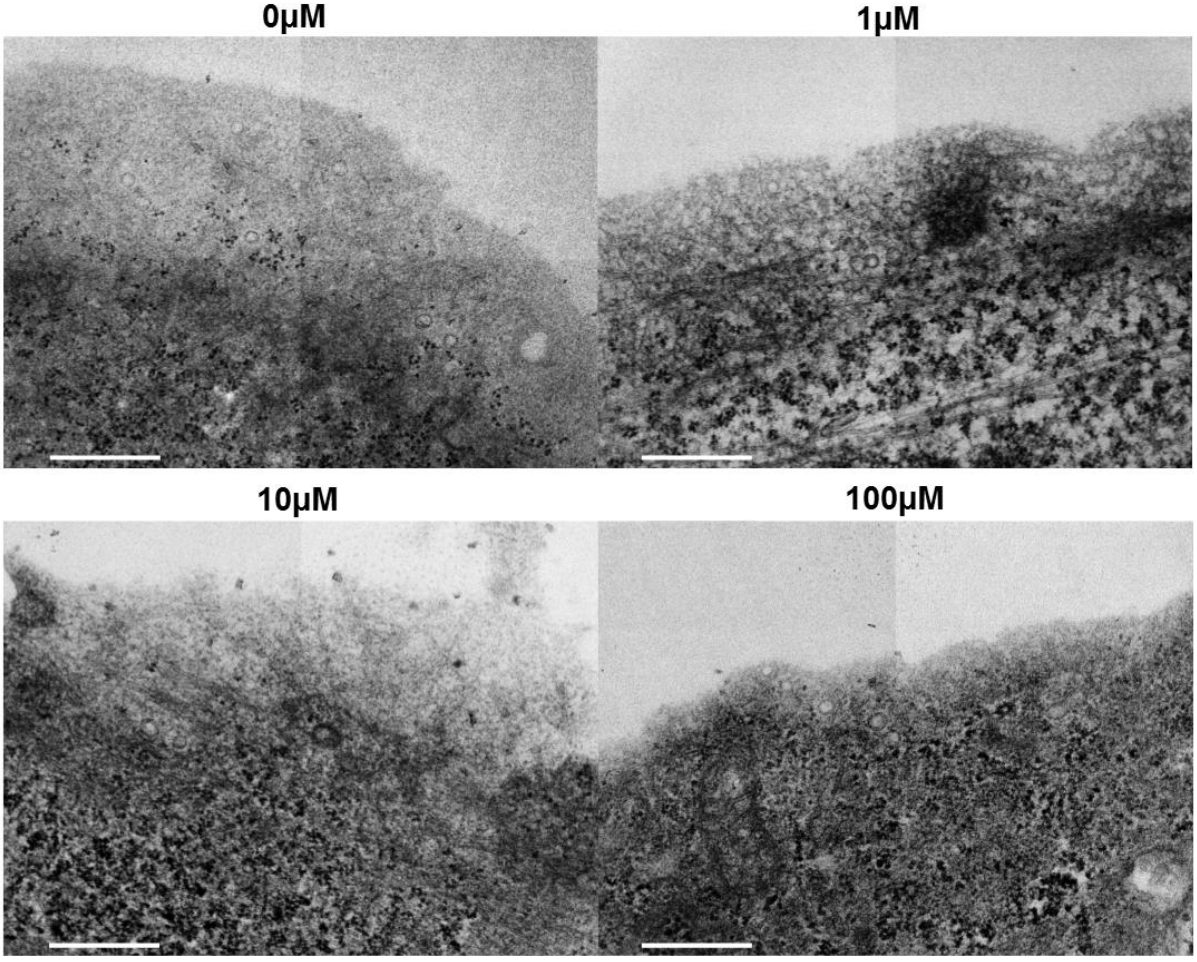

Figure 9: TEM images show EGL reduction with increased catecholamine stimulation. TEM images of the EGL following 4 hours of catecholamine stimulation (0µM, 1µM, 10µM, 100µM) and post-staining in 20.000x magnification. The reference bar is 500nm in length.

4.1.2 TEM images show unidentified vesicles in the EGL

Unidentified round vesicles were visualized in the EGL and can be seen on **Figure 10**. There was an increase in these vesicles with increased catecholamine concentrations.

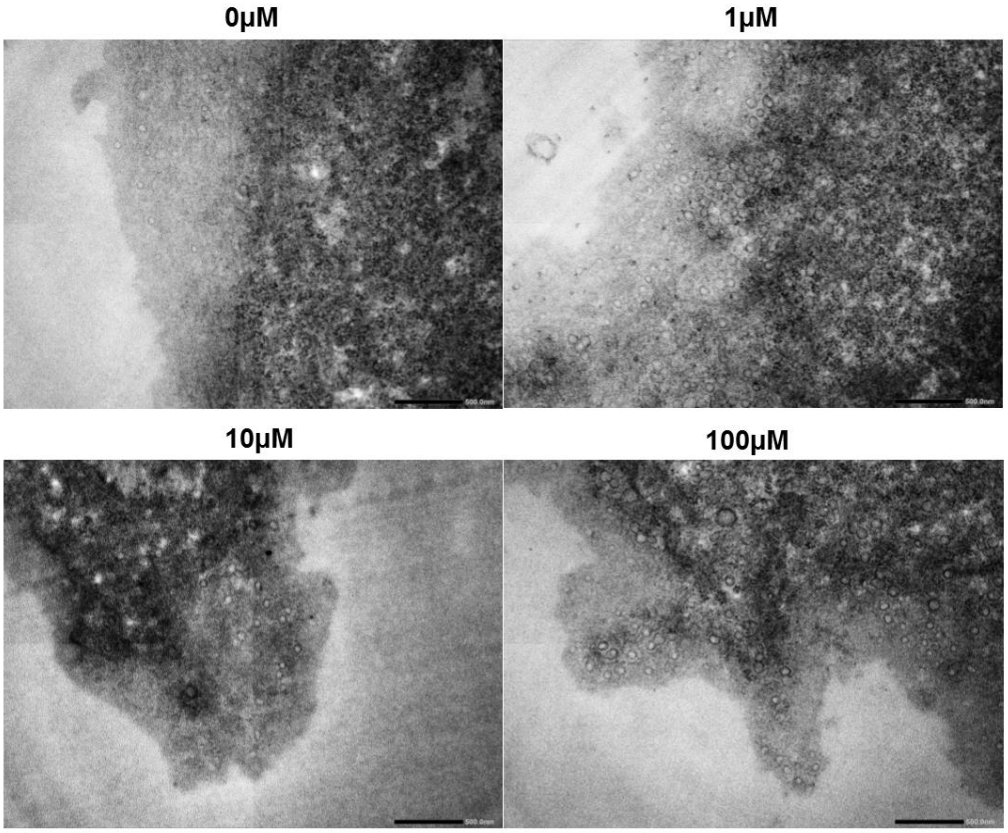

Figure 10: TEM images show unidentified vesicles in the EGL. TEM images of the EGL following 4 hours of catecholamine stimulation (0µM, 1µM, 10µM, 100µM) without post-staining in 15.000x magnification. The reference bar is 500nm in length.

4.1.3 TEM images show Weibel-Palade bodies in HUVECs

Figure 11 shows black, ovular and very densely packed vesicles, these are Weibel-Palade bodies, a well-known characteristic of ECs. No differences in the numbers of these structures were observed between control and catecholamine treated cells.

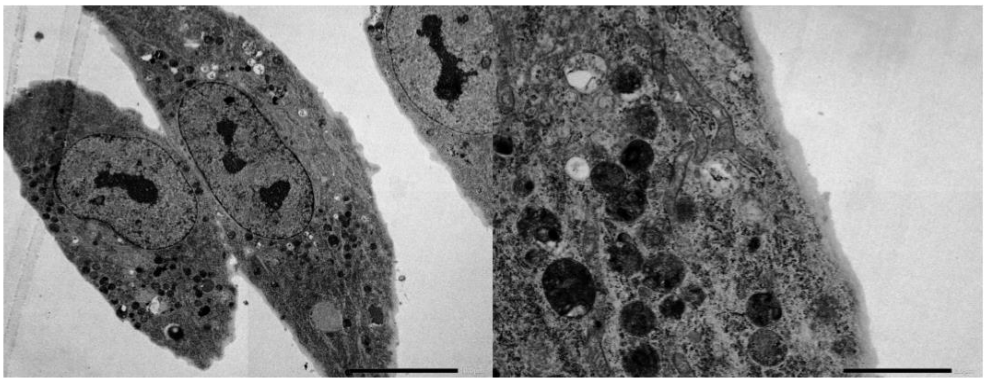

Figure 11: TEM images show Weibel-Palade bodies. TEM images of the EGL after 4 hours of incubation in EGM (0µM catecholamines) and post-staining. On the left: 1200x magnification, the reference bar is 10µM in length. On the right: 6000x magnification, the reference bar is 2 µM in length.

4.2 Effects of catecholamines on energy and signalling metabolism

4.2.1 Catecholamines effect ATP, AMP and cAMP metabolism

Intracellular concentrations of ATP, AMP and cAMP were measured to examine the effects of catecholamine stimulation on energy and signalling metabolism. **Figure 12 (A)** shows decrease in intracellular ATP concentrations with increased catecholamine concentrations after 4 and 24 hours of catecholamine stimulation. **Figure 12 (B)** shows that AMP concentrations decrease between 0,5µM and 50µM catecholamine treatment at 4 hours, but increase with elevated catecholamines at 24 hours. **Figure 12 (C)** shows that at 4 hours, cAMP concentration increases between 0uM and 5µM catecholamine treatment, and drops again at 50µM. No change is observed in cAMP concentrations at 24h. **Table 5** summarizes these results. Mass spectrometry data can be found in supplementary appendix 8.

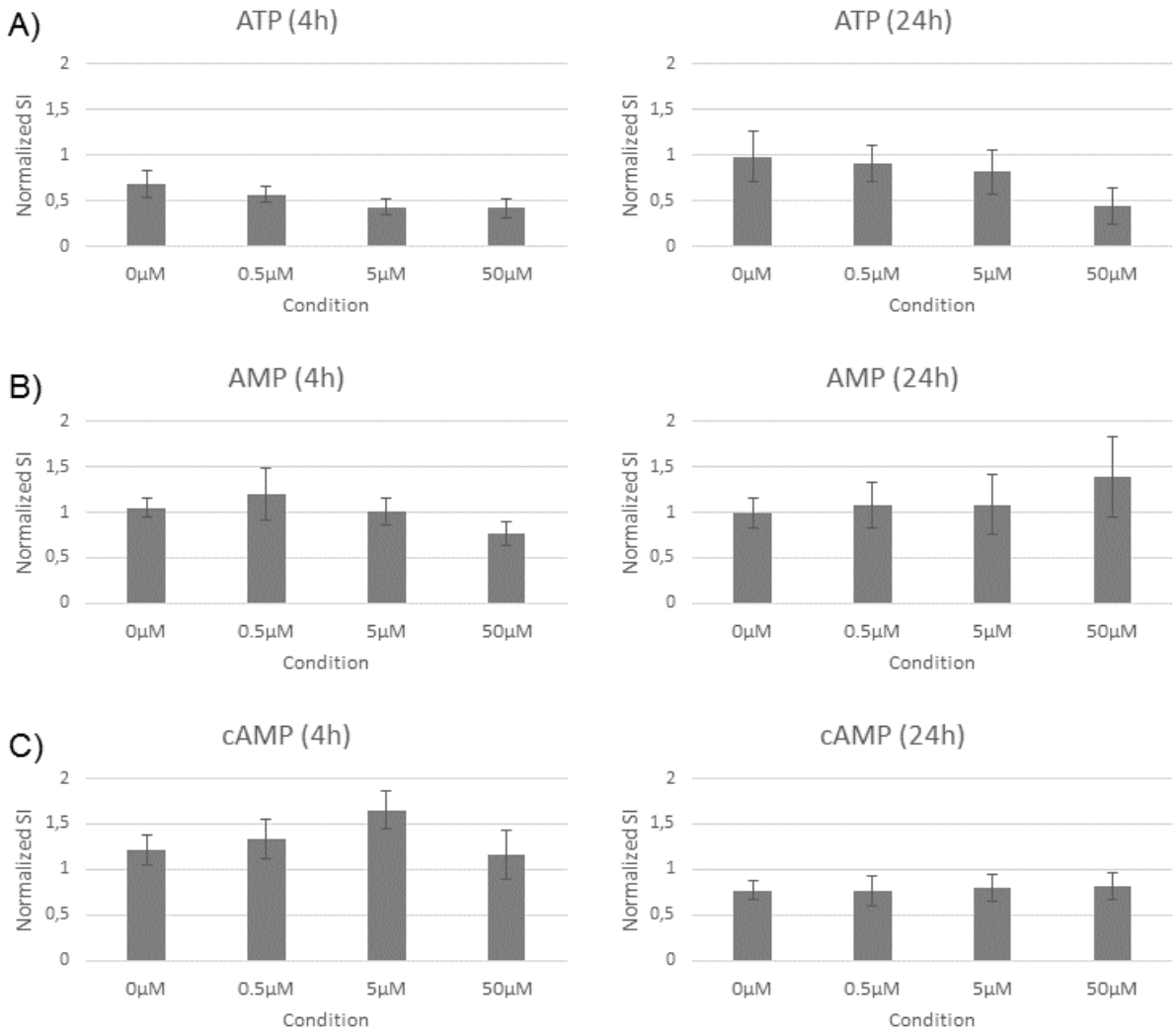

Figure 12: Intracellular concentrations of ATP, AMP and cAMP change in response to catecholamine stimulation. The effect of catecholamine stimulation (0,5µM, 5µM and 50µM) on **(A)** intracellular ATP, **(B)** AMP and **(C)** cAMP concentrations after 4 and 24 hours. Error bars show the standard error of measurements. The x-axis shows catecholamine concentrations and the y-axis shows the concentration of metabolites normalized to the standard intensity of the internal standard.

Table 5: Results for energy and signaling metabolism. Table shows the measurement type, the measurement metabolite and results after 4 and 24 hours of catecholamine stimulation.

Measurement type	metabolite	4 hours	24 hours
Intracellular concentration	ATP	decrease	decrease
Intracellular concentration	AMP	decrease	increase
Intracellular concentration	cAMP	increase	no trend

4.2.2 Catecholamines cause decrease in extracellular glucose and lactate

After demonstrating that catecholamine stimulation had effects on the EGL phenotype and energy and signalling metabolism, its effect on glycolysis were examined. Extracellular glucose and lactate concentrations were measured after 4 and 24 hours of catecholamine stimulation. **Figure 13 (A)** schematically shows glycolysis, and the production of lactate from pyruvate, the end product of glycolysis. **Figure 13 (B)** shows measurements of baseline samples that have some degree of standard deviation for 0µM glucose. **Figure 13 (C)** and **(D)** show the measured values of glucose and lactate at 4 and 24 hours without subtraction of the baseline values. The concentration of lactate seems to decrease with increased catecholamine concentrations at both timepoints, while the concentration of glucose seems to increase.

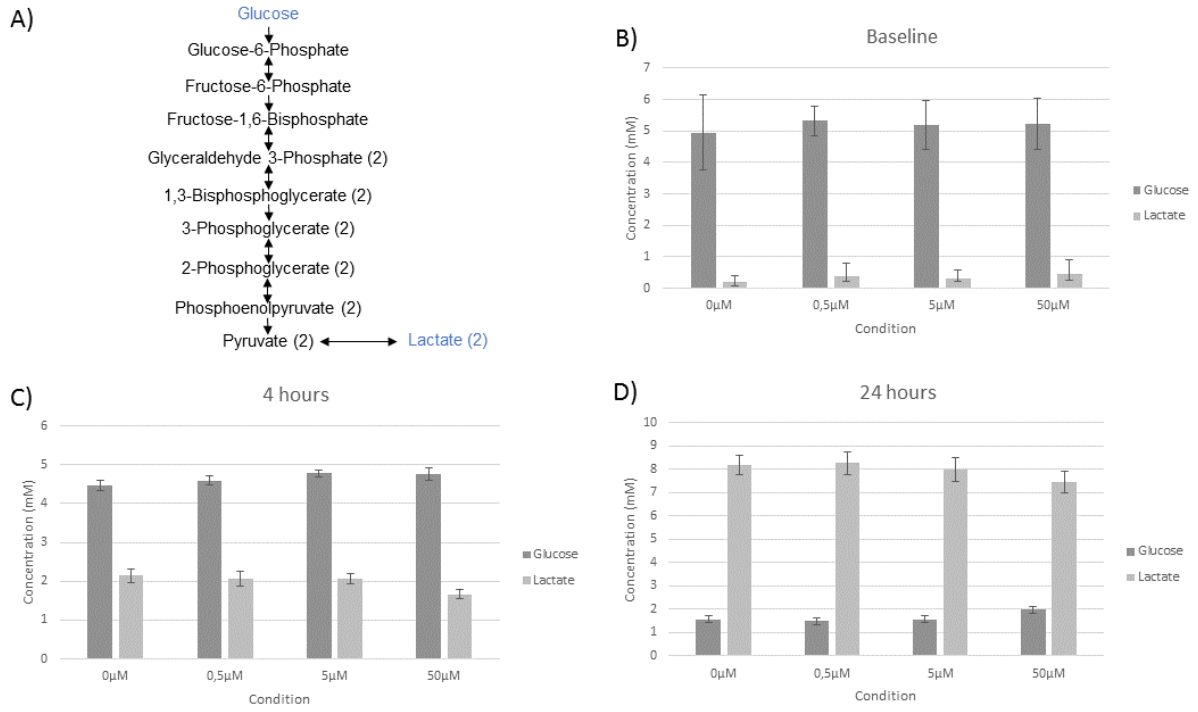

Figure 13: Baseline, 4 and 24 hour measurements of extracellular glucose and lactate. (A) Overview of glycolysis and the production of 2 lactates from 2 pyruvates. **(B)** Baseline measurements of glucose and lactate. **(C)** The effect of catecholamine stimulation (0,5µM, 5µM and 50µM) on extracellular glucose and lactate concentrations after 4 hours. **(D)** The effect of catecholamine stimulation (0,5µM, 5µM and 50µM) on extracellular glucose and lactate concentrations after 24 hours. The error bars show the standard errors of measurements.

When baseline values were subtracted from their corresponding 2 and 24 hour measurements and averages of standard errors calculated, a trend of decreased extracellular lactate and glucose was visible. The baseline value was fixed (average of baseline measurements) as the starting concentration of glucose and lactate should be the same in all cases. **Figure 14 (A)** shows that after 4 hours of catecholamine stimulation, lactate concentrations decrease from 1,8mM to 1,3mM and glucose concentrations decrease from 0,7mM to 0,4mM, reflecting decreased lactate secretion and glucose uptake parallel to increase in catecholamines. **Figure 14 (B)** shows the ratio of glucose uptake/lactate secretion at 4 hours, which is decreases with catecholamine treatment. A normal ratio is 0,5 – where 1 glucose is consumed to produce 2 lactates (via 2 pyruvates). A ratio below 0,5 suggests lactate production from other sources. **Figure 15 (A)** shows the same trend at 24 hours, where lactate concentrations decrease from 7,8mM to 7,1mM and glucose concentrations decrease from 3,6mM to 3,1mM. **Figure 15 (B)** shows the ratio of glucose uptake/lactate secretion at 24 hours, which stay the same for catecholamine treated and non-treated samples.

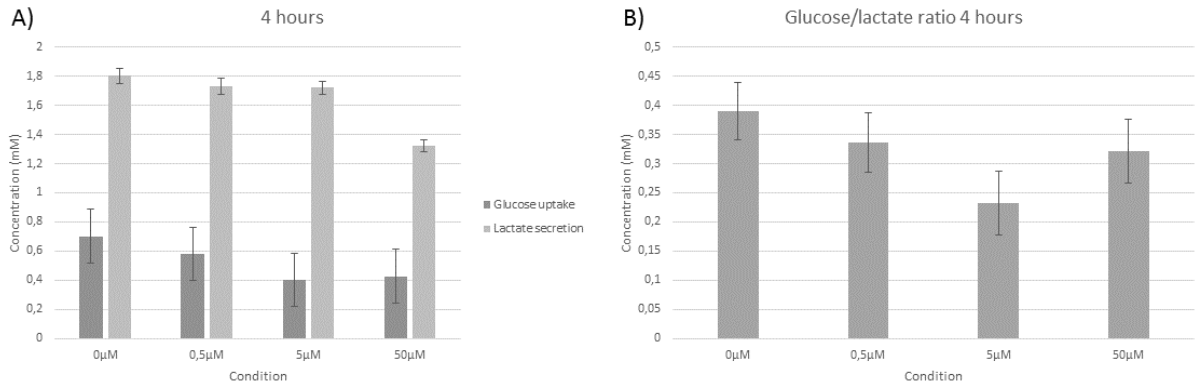

Figure 14: Extracellular measurements of glucose and lactate suggest a drop in lactate secretion after 4 hours of catecholamine stimulation. (A) The effect of catecholamine stimulation (0,5µM, 5µM and 50µM) on glucose uptake and lactate secretion after 4 hours. Datapoints represent subtraction of baseline values (**Figure 13 B**) from measured values at 4 hours (**Figure 13 C**). Fixed baseline values were 5,17mM for glucose and 0,33mM for lactate. Averages of standard errors are shown. **(B)** The ratio of glucose uptake/lactate secretion after 4 hours of catecholamine stimulation (0,5µM, 5µM and 50µM).

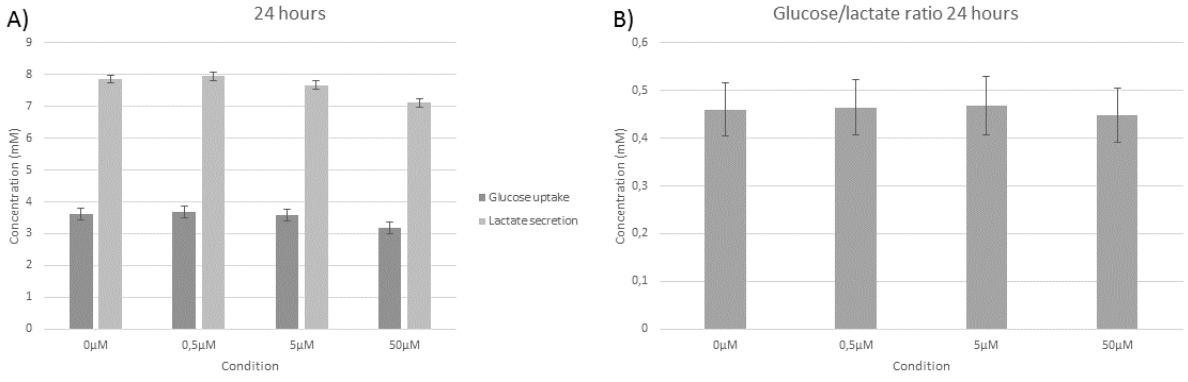

Figure 15: Extracellular measurements of glucose and lactate suggest a drop in lactate secretion after 24 hours of catecholamine stimulation. (A) The effect of catecholamine stimulation (0,5µM, 5µM and 50µM) on glucose uptake and lactate secretion after 24 hours. Datapoints represent subtraction of baseline values (**Figure 13 B**) from measured values at 24 hours (**Figure 13 D**). Fixed baseline values were 5,17mM for glucose and 0,33mM for lactate. **(B)** The ratio of glucose uptake/lactate secretion after 24 hours of catecholamine stimulation (0,5µM, 5µM and 50µM).

According to this data, intracellular concentrations of glucose and lactate decrease (**figures 13-15**), which implies that lactate secretion and glucose uptake slow down as a response to increased catecholamine concentrations. **Table 6** summarizes results for glycolysis. See supplementary appendix 2 for measurements and calculations of glucose and lactate.

Table 6: Results for glycolysis. Table shows the measurement type, the measured metabolite, and the results after 4 and 24 hours of catecholamine stimulation.

Measurement type	**metabolite**	**4 hours**	**24 hours**
Extracellular concentration	Lactate	decrease	decrease
Extracellular concentration	Glucose	decrease	decrease
Extracellular concentration	Glucose/lactate ratio	no trend	no trend

4.3 Catecholamines cause decreased activity of the TCA cycle

After demonstrating that catecholamines exerted their effects on glycolysis, the effects on the tricarboxylic acid (TCA) cycle were investigated. Measurements of cycle intermediates and anaplerotic metabolites were carried out. To investigate the effects of catecholamines on the TCA cycle, intracellular concentrations of citrate, succinate and malate were measured. ^{13}C-6 heavy isotope nutrient labelling of citrate was also measured to explore its synthesis rate. Intra- and extracellular concentrations of L-glutamine and L-glutamate were measured, their synthesis rates were also measured with ^{13}C-6 and ^{15}N-2 heavy isotope nutrient labelling. **Figure 16** shows glycolysis, the TCA cycle, and the fate of ^{13}C-6 labelled glucose in these metabolic pathways. L-glutamine and L-glutamate are also shown in the context of the TCA cycle, where they are used as anaplerotic metabolites.

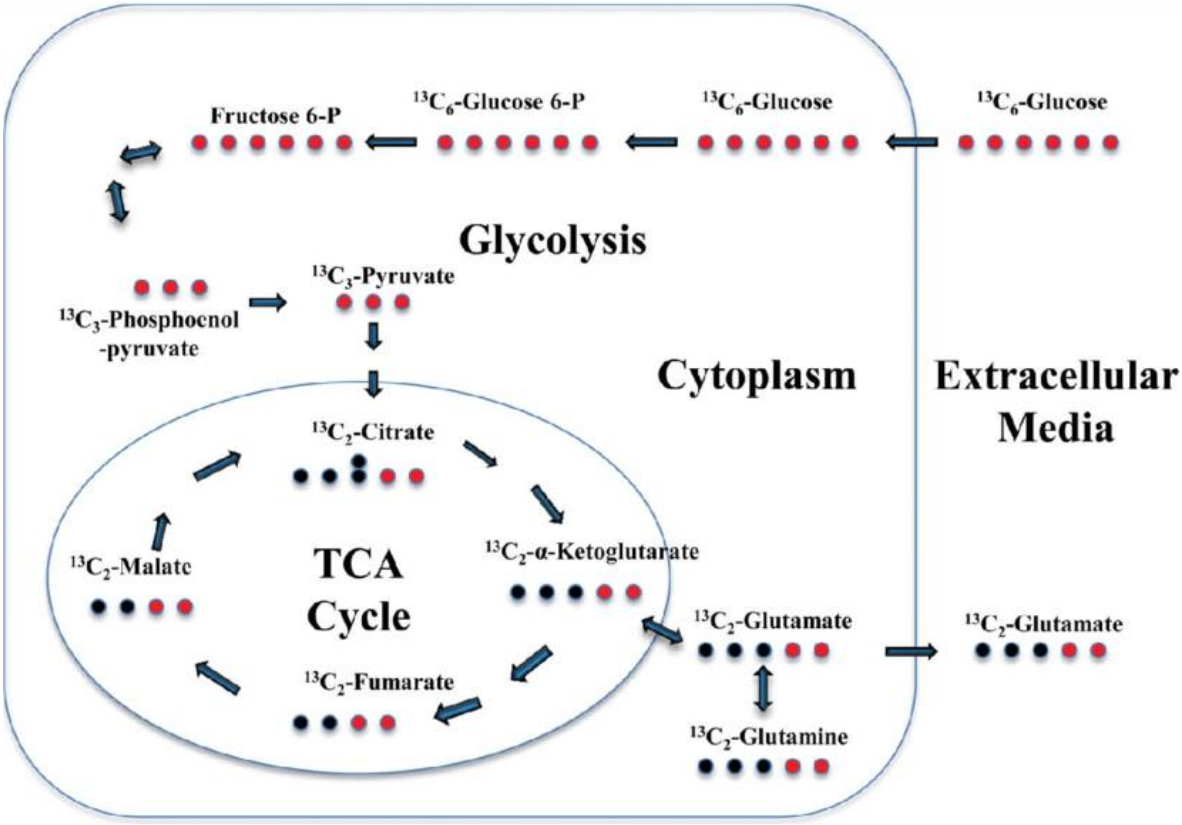

Figure 16: The fate of 13C-6 glucose in the TCA cycle. The figure shows glycolysis, the TCA cycle and how 13C-6 glucose is incorporated into TCA cycle intermediates and anaplerotic metabolites. It also shows how L-glutamate and L-glutamine are used to generate a-ketoglutarate which is used in the TCA cycle, they are anaplerotic metabolites(66).

4.3.1 Catecholamines cause decrease in intracellular concentrations of citrate, succinate and malate

To investigate the effects catecholamines exerted on the TCA cycle, intracellular concentrations of cycle intermediates were measured. **Figure 17 (A)** shows a dose-dependent drop in citrate concentrations as a response to increased catecholamines after 4 hours. This trend is also observed after 24 hours, except for the 50µM measurements which are higher than the 5µM. This effect is greater at 24 hours than at 4 hours. **Figure 17 (B)** shows a dose-dependent drop in succinate concentrations after 4 hours of catecholamine stimulation, but no trend is observed at 24 hours. **Figure 17 (C)** shows a considerable dose-dependent drop in malate concentrations in response to increased catecholamines at both timepoints, excluding the 0µM measurement which does not follow this trend. According to this data, there is an overall trend of a drop in concentrations of intracellular TCA cycle intermediates.

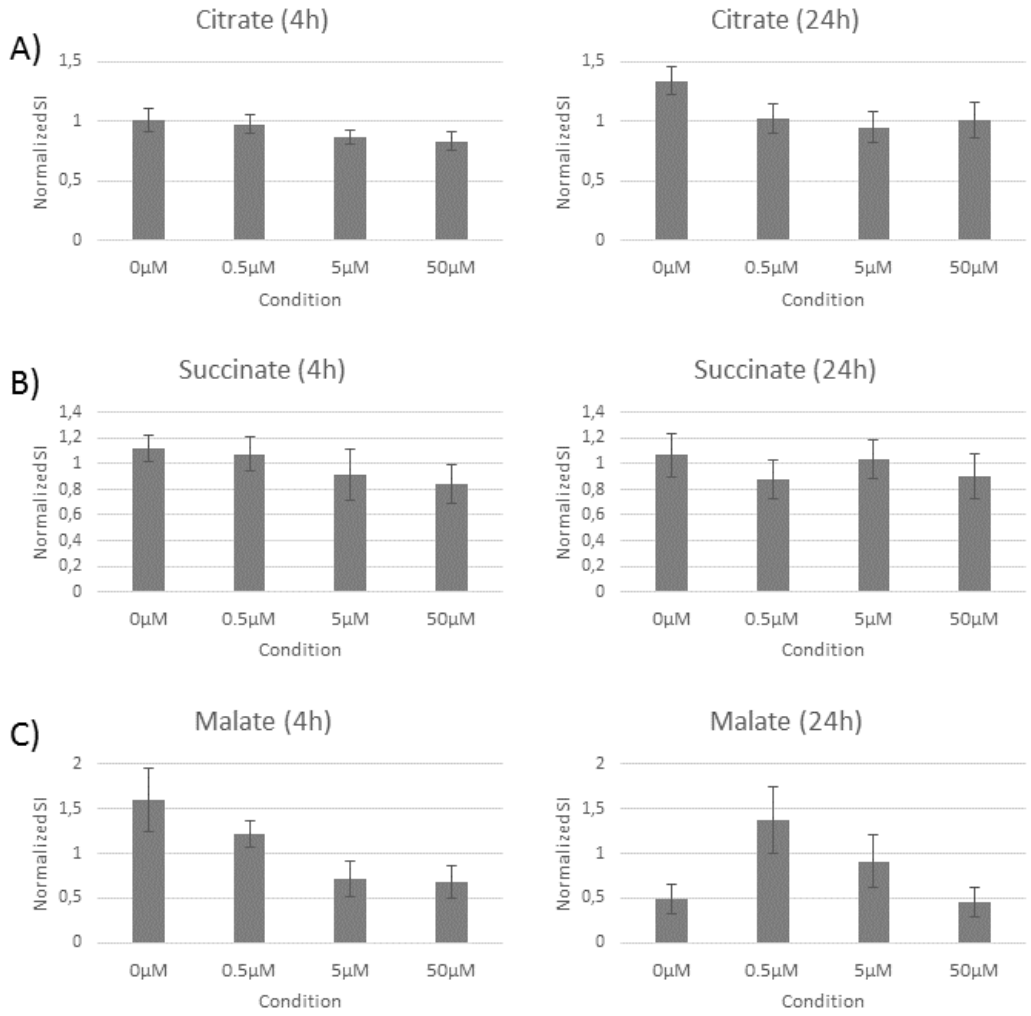

Figure 17: Catecholamine stimulation causes decrease in intracellular concentrations of TCA cycle intermediates. The effect of catecholamine stimulation (0,5µM, 5µM and 50µM) on intracellular (A) citrate, (B) succinate, and (C) malate concentrations after 4 and 24 hours. The error bars show the standard error of measurements. The x-axis shows catecholamine concentrations and the y-axis shows metabolite concentration normalized to the standard intensity of an internal standard.

4.3.2 Catecholamines cause slower synthesis rates of citrate

To identify if synthesis rates contributes to the lower intracellular concentrations of TCA cycle intermediates, synthesis rates of citrate were measured. **Figure 18** shows results for the ^{13}C-6 labelling of citrate at 4 and 24 hours after catecholamine stimulation. Label incorporation decreases in a dose-dependent manner after 4 hours of catecholamine stimulation, implying that catecholamines cause slower synthesis rates of citrate from glucose (via the TCA cycle). On the contrary, greater label incorporation is observed for 5µM catecholamine treatment at 24 hours. See supplementary appendix 8 for calculations.

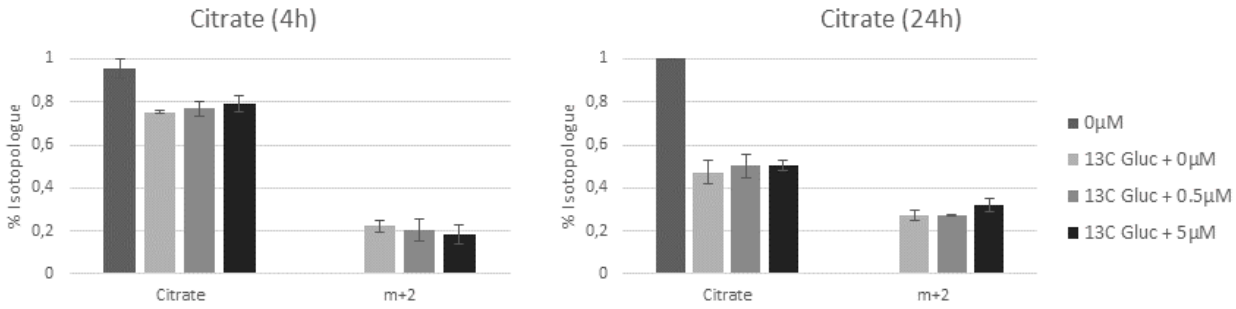

Figure 18: 13C-6 label incorporation implies slower synthesis rates of citrate after 4 hours of catecholamine stimulation. The effect of catecholamine stimulation (0,5µM, and 5µM) on 13C-6 label incorporation of citrate after 4 and 24 hours. Error bars show the standard error of measurements. The x-axis shows measurements of unlabeled citrate (Citrate) and citrate labelled with 2 heavy isotope carbons derived from 13C-6 glucose (m+2). The y-axis shows the measured percentage of labeled and unlabeled citrate at a given condition (see legend titles). 0µM includes nor catecholamines or labelling and thus is measured as 100% unlabelled.

4.3.3 Catecholamines cause a trend of dose-dependent rise in extracellular L-glutamine concentration

The next step in TCA cycle investigation was to measure extracellular concentrations of anaplerotic metabolites, here results for extracellular L-glutamine concentrations in are represented. **Figure 19 (A)** shows baseline measurement of L-glutamine and **Figure 19 (B)** shows the measured concentrations of L-glutamine in extracellular samples after 4 and 24 hours of catecholamine stimulation, without subtraction of baseline values. Despite a high degree of standard deviation, a trend of elevated extracellular L-glutamine concentrations are visible following catecholamine stimulation at both timepoints. Concentrations are higher at 24 hours than at 4 hours following catecholamine stimulation.

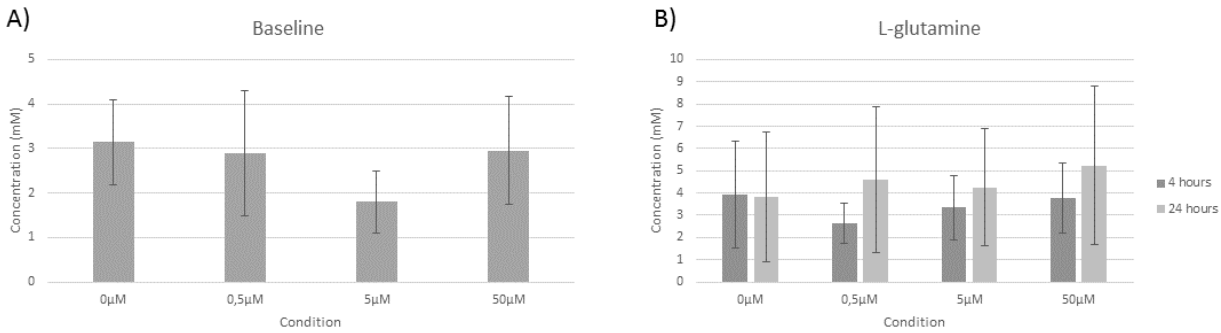

Figure 19: Extracellular measurements of L-glutamine suggest an increase in concentrations after 24 hours of catecholamine stimulation. (A) Baseline measurements for L-glutamine, and **(B)** measurements of extracellular L-glutamine concentrations after 4 and 24 hours of catecholamine stimulation (0,5µM, 5µM and 50µM). Error bars show the standard deviation of measurements.

When baseline values were subtracted from measured values and averages of standard deviations calculated, a rising trend in extracellular L-glutamine concentrations became apparent at 24 hours as can be seen on **Figure 20**. The baseline value was fixed (average of baseline measurements) as the starting concentration of L-glutamine should be the same in all cases. At 24 hours there is a rise in extracellular concentrations of L-glutamine, where concentration rises from 0,8mM to 2,2mM. The concentration increase is clear, but the degree of standard error is very high. According to this data, an extracellular concentration increase of L-glutamine as a response to catecholamine stimulation is possible. 4 hour measurements show no trend in increase or decrease. See supplementary appendix 2A for measurements and calculations of L-glutamine concentrations.

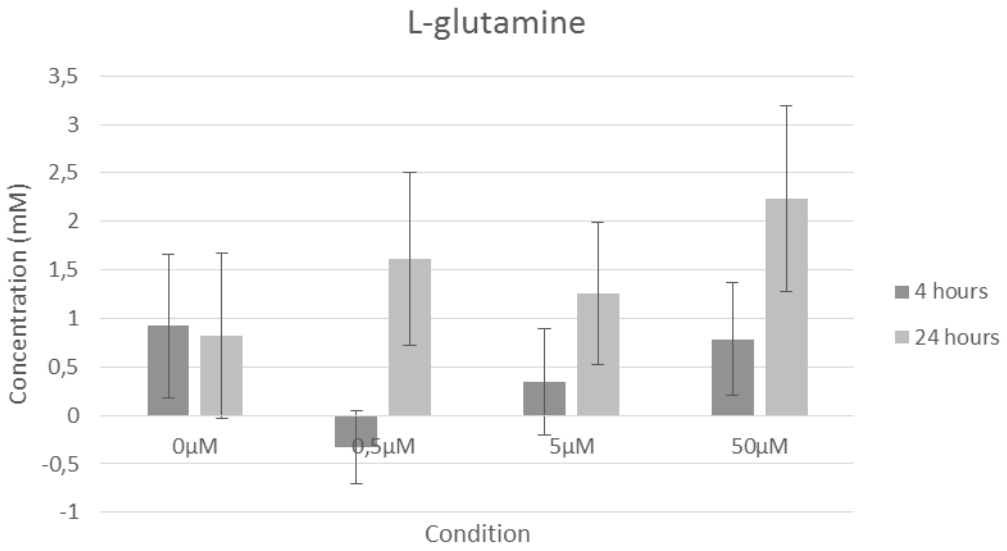

Figure 20: A dose-dependent rise in extracellular concentrations of L-glutamine is observed after 24 hours of catecholamine stimulation. The effect of catecholamine stimulation (0,5µM, 5µM and 50µM) on L-glutamine secretion/uptake after 4 and 24 hours. Baseline values (**Figure 19 A**) were subtracted from measured values at 4 and 24 hours (**Figure 19 B**). Fixed baseline value was 2,99mM. Error bars represent the mean standard errors.

4.3.4 Catecholamines cause a trend of dose-dependent decrease in extracellular L-glutamate concentration

Next, extracellular concentrations of another anaplerotic metabolite were measured, here results for L-glutamate are represented. **Figure 21 (A)** shows baseline measurements of L-glutamate, which have a high degree of variation. **Figure 21 (B)** shows the measured concentrations of L-glutamate after 4 and 24 hours of catecholamine stimulation, without subtraction of baseline values. The data is very variable, but there seems to be a trend of decreased levels of L-glutamate with increased catecholamine for the 24 hour timepoint.

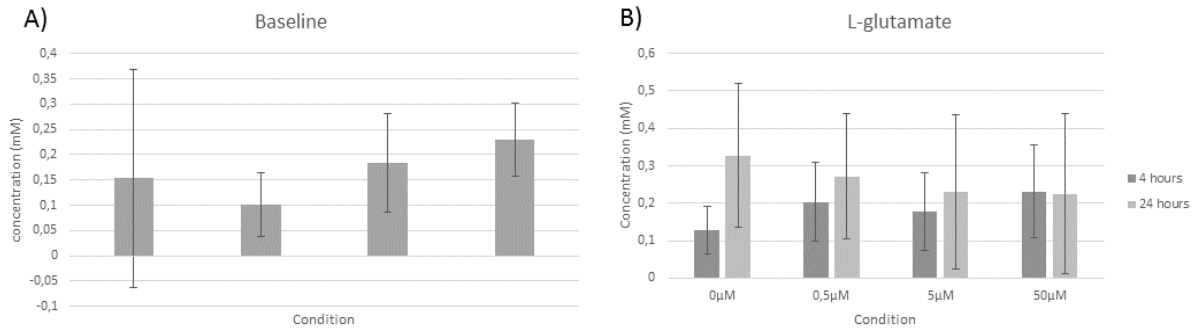

Figure 21: Extracellular measurements of L-glutamate suggest a decrease in concentrations after 24 hours of catecholamine stimulation. (A) Baseline measurements of L-glutamate in medium samples and **(B)** measurements of extracellular L-glutamate concentrations after 4 and 24 hours of catecholamine stimulation (0,5µM, 5µM ans 50µM). Error bars show the standard deviation of measurements.

Figure 22 shows results for when baseline values were subtracted from measured values and averages of standard deviations calculated. The baseline value was set at a fixed values (average of baseline measurements) as the starting concentration of L-glutamate should be the same in all cases. A dose-dependent decrease in extracellular concentrations was observed after 24 hours of catecholamine stimulation, where concentration decreased from 0,16mM to 0,05mM. According to this data, an extracellular concentration decrease of L-glutamate as a response to catecholamine stimulation is possible. 4 hours of catecholamine stimulation does not exert any observable effects on extracellular L-glutamate levels. See supplementary appendix 2 for measurements and calculations of L-glutamate concentrations.

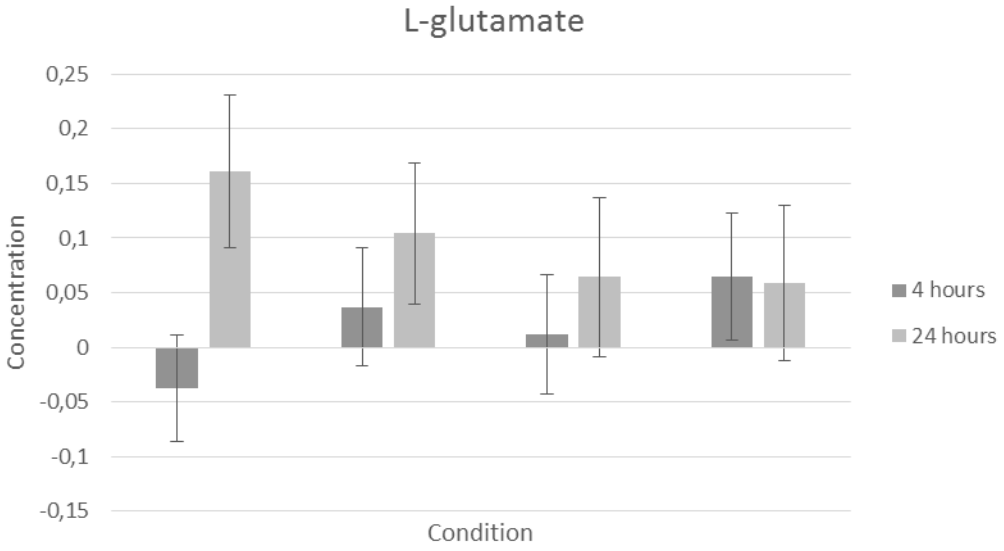

Figure 22: A dose-dependent decrease in extracellular concentrations of L-glutamate is observed after 24 hours of catecholamine stimulation. The effect of catecholamine stimulation (0,5µM, 5µM, and 50µM) on L-glutamate secretion/uptake after 4 and 24 hours. Baseline (**Figure 20 A**) were subtracted from measured values at 4 and 24 hours (**Figure 20 B**). value was 0,16mM. Averages of standard deviations are shown.

4.3.5 Catecholamines cause a decrease in intracellular concentrations of L-glutamine and L-glutamate

L-glutamine and L-glutamate were also measured intracellularly after 4 and 24 hours of catecholamine stimulation. **Figure 23 (A)** shows a slight decrease in L-glutamine concentrations after 4 hours, whereas the 24 hour measurements shows no trend. **Figure 23 (B)** shows a dose-dependent decrease in L-glutamate at both timepoints, this decrease is of larger scale than what is observed for L-glutamine. According to this data, the intracellular concentrations of these metabolites decrease with increased catecholamine concentrations.

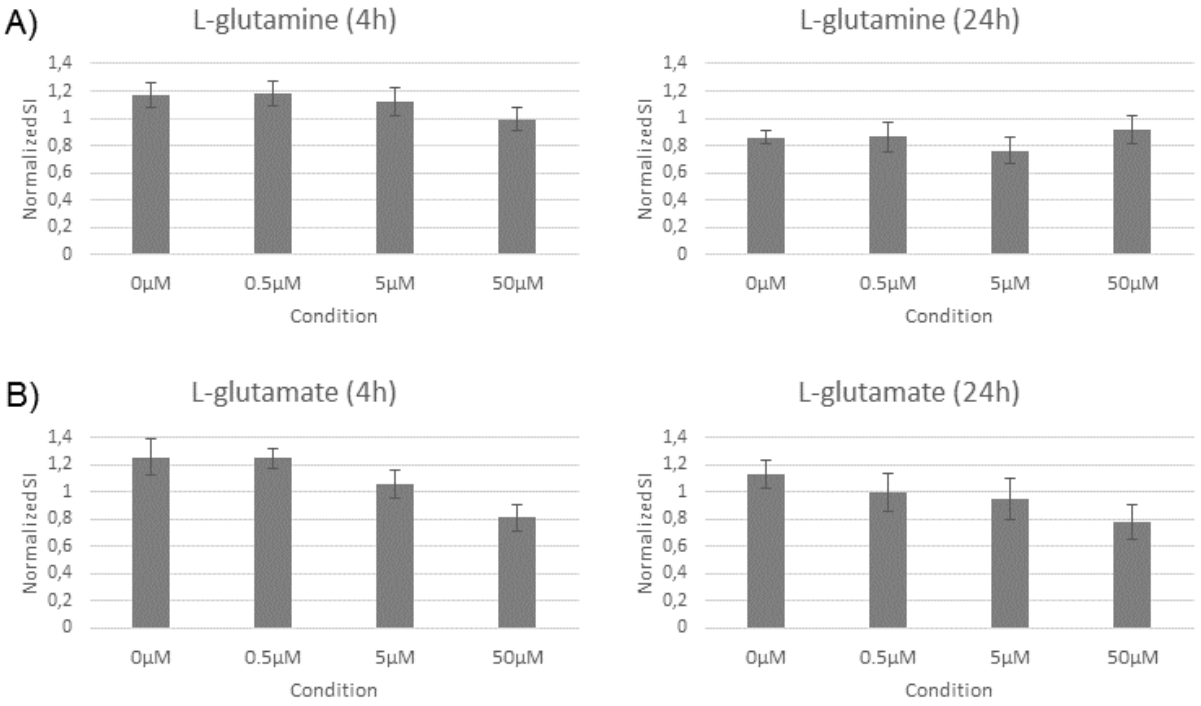

Figure 23: A decrease in intracellular concentrations of L-glutamine and L-glutamate is observed after 4 and 24 hours of catecholamine stimulation. The effect of catecholamine stimulation (0,5µM, 5µM and 50µM) on (A) intracellular L-glutamine, and (B) intracellular L-glutamate concentrations after 4 hours and 24 hours. Error bars show the standard deviation of measurements. The x-axis shows catecholamine concentrations and the y-axis shows metabolite concentration normalized to the standard intensity of an internal standard.

4.3.6 Catecholamines cause lower synthesis rates of L-glutamine and L-glutamate

To further investigate catecholamine effects on L-glutamine and L-glutamate, their synthesis was examined after catecholamine stimulation. **Figure 24** shows results for ^{13}C-6 labelling of L-glutamate at 4 and 24 hours after catecholamine stimulation. At 4 hours the label incorporation is the same in all cases. At 24 hours a slight drop in label incorporation is observed for 5µM catecholamines, suggesting slower synthesis rate for L-glutamate after 24 hours of catecholamine stimulation.

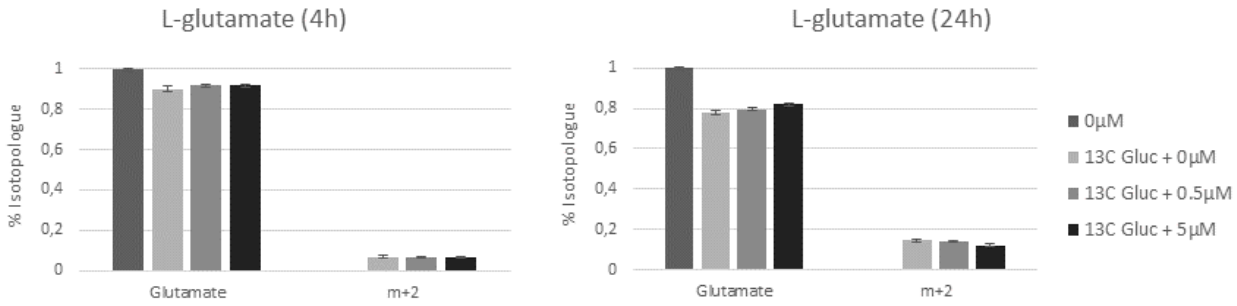

Figure 24: 13C-6 label incorporation implies slower synthesis rates of L-glutamate after 24 hours of catecholamine stimulation. The effect of catecholamine stimulation (0,5µM, and 5µM) on 13C-6 label incorporation of L-glutamate after 4 and 24 hours. The x-axis shows measurements of unlabeled L-glutamate and L-glutamate labelled with 2 heavy isotope carbons derived from 13C-6 glucose (m+2). The y-axis shows the measured percentage of labeled and unlabeled citrate at a given condition (see legend titles). 0µM includes nor catecholamines or labelling and thus is measured as 100% unlabelled. Error bars show the standard error of measurements.

Figure 25 shows results for ^{15}N-2 labelling of L-glutamine and L-glutamate at 4 and 24 hours after catecholamine stimulation. **Figure 25 (A)** shows that L-glutamine ^{15}N-2 label incorporation drops with 5µM catecholamine stimulation at both timepoints. **Figure 25 (B)** shows that L-glutamate ^{15}N-2 label incorporation drops in a dose-dependent manner after 4 and 24 hours of catecholamine stimulation. According to this data, the synthesis rates of L-glutamine and L-glutamate decrease in response to increased catecholamine concentrations.

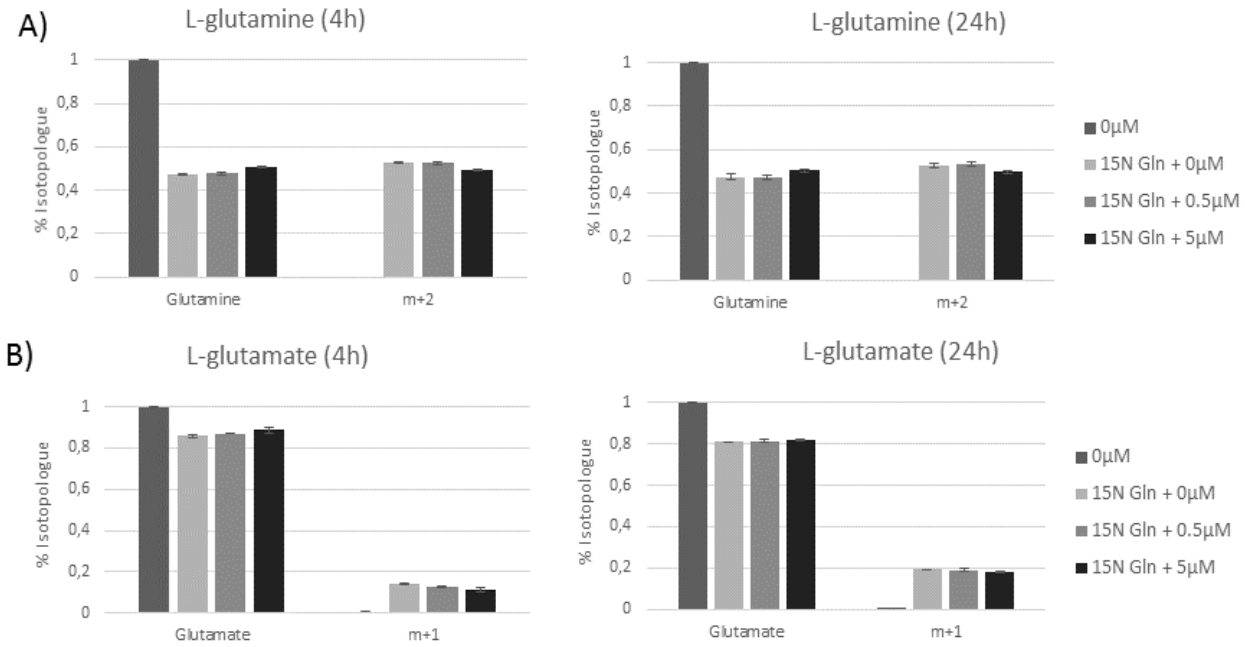

Figure 25: 15N-2 label incorporation implies slower synthesis rates of both L-glutamine and L-glutamate after 4 and 24 hours of catecholamine stimulation. The effect of catecholamine stimulation (0,5µM, and 5µM) on **(A)** 15N-2 label incorporation of L-glutamineand **(B)** L-glutamate after 4 and 24 hours. The x-axis shows measurements of unlabeled L-glutamine and L-glutamate and labelled with 2 or 1 heavy isotope carbons derived from 15N-2 glutamine (m+2 and m+1). The y-axis shows the measured percentage of labeled and unlabeled molecules at a given condition (see legend titles). 0µM includes nor catecholamines or labelling and thus is measured as 100% unlabelled. Error bars show the standard error of measurements.

According to measurements of TCA cycle intermediated and anaplerotic metabolites, intracellular concentrations and synthesis rates are decreased in most cases. This strongly suggests that the metabolic activity of the TCA cycle is decreased as a response to catecholamine stimulation. **Table 10** summarizes results for the TCA cycle. Mass spectrometry data can be found in supplementary appendix 8.

Table 7: Results for TCA cycle metabolism. Table shows the measurement type, the measured metabolite, and the results after 4 and 24 hours of catecholamine stimulation.

Measurement type	metabolite	4 hours	24 hours
Intracellular concentration	Citrate	decrease	decrease
Intracellular concentration	Succinate	decrease	no trend
Intracellular concentration	Malate	decrease	decrease
Intracellular concentration	L-glutamine	decrease	no trend
Intracellular concentration	L-glutamate	decrease	decrease
Extracellular concentration	L-glutamine	no trend	increase
Extracellular concentration	L-glutamate	no trend	decrease
Synthesis rate (13C-6)	Citrate	decrease	increase
Synthesis rate (13C-6)	L-glutamate	no trend	decrease
Synthesis rate (15N-2)	L-glutamine	decrease	decrease
Synthesis rate (15N-2)	L-glutamate	decrease	decrease

4.4 Effects of catecholamines on EGL metabolism

4.4.1 Catecholamines cause a decrease in intracellular EGL metabolite precursors

After catecholamine effects on the EGL phenotype, signalling and energy metabolism, glycolysis and the TCA cycle had been established, the effects of intracellular concentrations of EGL precursors were examined. **Figure 26** shows results for intracellular concentrations of UDP-Glucose and UDP-N-acetylglucosamine after 4 and 24 hours of catecholamine stimulation. A drop in concentration is observed for both metabolites at both timepoints, excluding the 5µM measurements of UDP-Glucose at 4 hours. According to this data, there is a decrease in intracellular EGL precursors as a response to catecholamine stimulation.

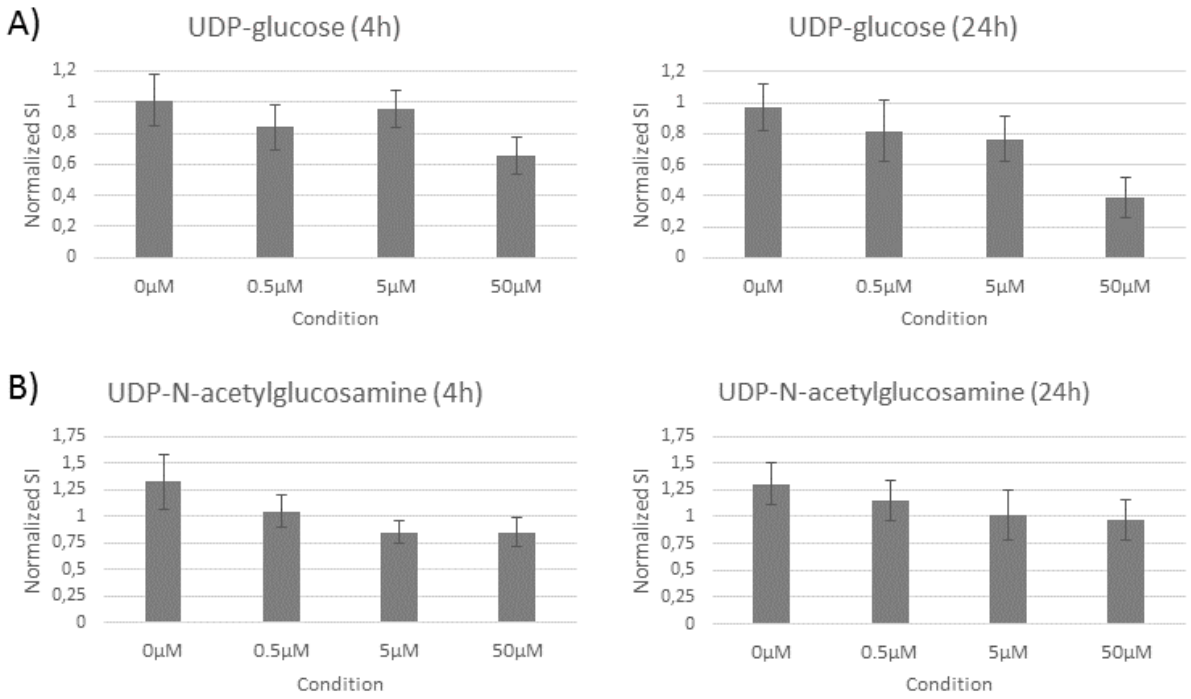

Figure 26: Intracellular concentrations of EGL precursors drop in response to catecholamine stimulation. The effect of catecholamine stimulation (0,5µM, 5µM and 50µM) on **(A)** intracellular UDP-Glucose, and **(B)** UDP-N-acetylglucosamine concentrations after 4 and 24 hours. Error bars show the standard error of measurements. The x-axis shows catecholamine concentrations and the y-axis shows metabolite concentration normalized to the standard intensity of an internal standard.

4.4.2 Catecholamines cause lower synthesis rates of EGL precursors

After establishing a decrease in EGL precursors as a response to catecholamines, synthesis rates of these precursors were measured by ^{13}C-6 and ^{15}N-2 heavy isotope nutrient labelling. **Figure 27 (A)** shows that after 4 hours, a dose-dependent drop in 13C-6 label incorporation is observed for UDP-glucose. This effect is not observed at 24 hours. According to this data, slower synthesis rates of UDP-glucose are observed after 4 hours of catecholamine stimulation. **Figure 27 (B)** shows no specific trends for 13C-6 label incorporation of UDP-N-acetylglucosamine at either timepoints. **Figure 27 (C)** shows that at 4 hours, 15N-2 label incorporation to UDP-N-acetylglucosamine decreases for m+1. On the contrary, at 24 hours, the 15N-2 incorporation to UDP-N-acetylglucosamine increases for m+1 and decreases slightly for m+2. According to this data, synthesis rates of UDP-N-acetylglucosamine are affected via incorporation of nitrogens after 4 hours of catecholamine stimulation. **Table 8** summarizes results for EGL precursors. Mass spectrometry data can be found in supplementary appendix 8.

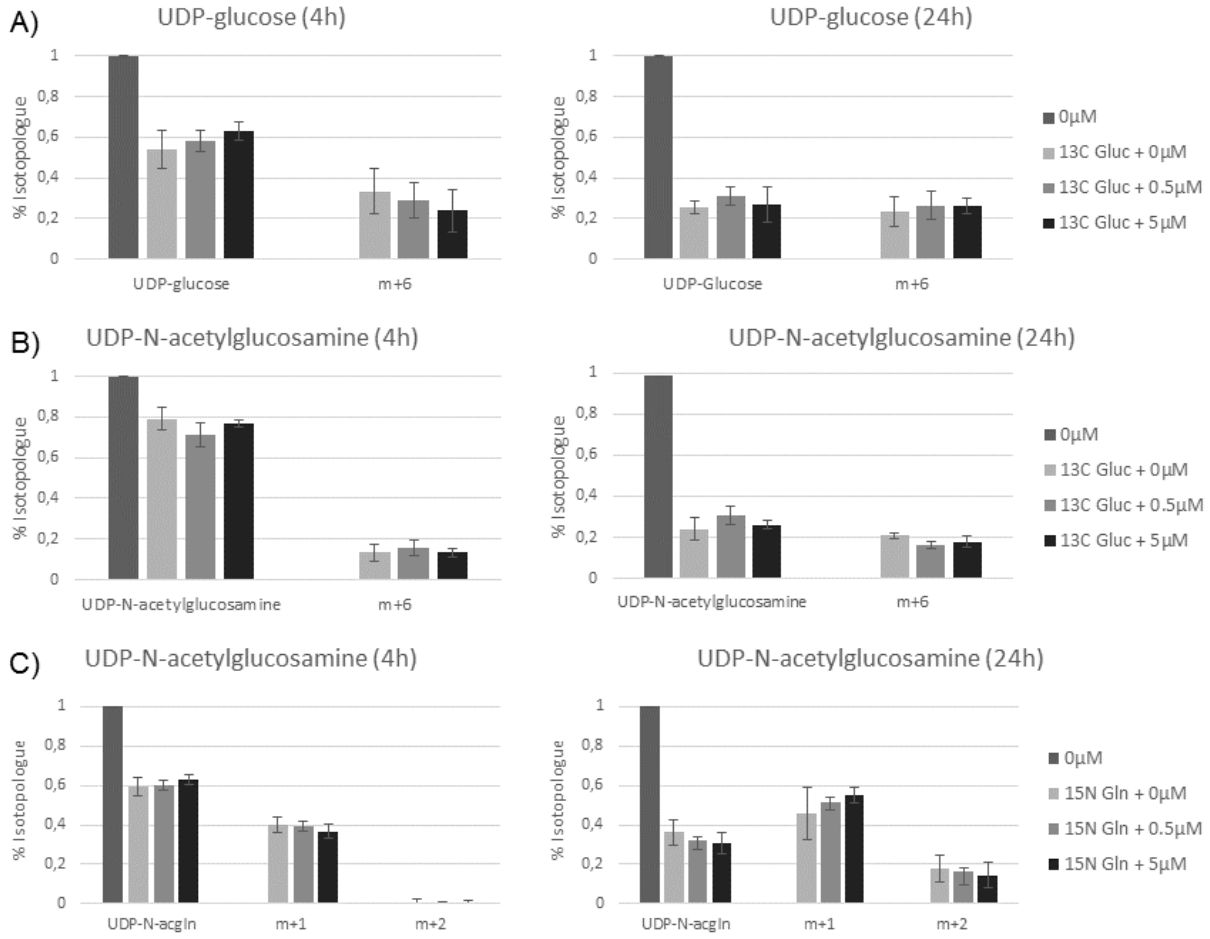

Figure 27: 13C-6 and 15N-2 label incorporation imply slower synthesis rates of EGL precursors after 4 and 24 hours of catecholamine stimulation. The effect of catecholamine stimulation (0,5µM, and 5µM) on 13C-6 label incorporation of **(A)** UDP-Glucose and **(B)** UDP-N-acetylglucosamine, and **(C)** 15N-2 incorporation into UDP-N-acetylglucosamine after 4 and 24 hours. The x-axis shows measurements of unlabeled molecules and molecules labelled with 6, 2 or 1 heavy isotope carbons (m+6, m+2, m+1) derived from 13C-6 glucose or 15N-2 glutamine. The y-axis shows the measured percentage of labeled and unlabeled molecules at a given condition (see legend titles). 0µM includes nor catecholamines or labelling and thus is measured as 100% unlabelled. Error bars show the standard error of measurements.

Table 8: Results for EGL metabolism. Table shows the measurements type, the measured metabolite and results after 4 and 24 hours of catecholamine stimulation.

Measurement type	metabolite	4 hours	24 hours
Intracellular concentration	UDP-glucose	decrease	decrease
Intracellular concentration	UDP-N-acetylglucosamine	decrease	decrease
Synthesis rates (13C-6)	UDP-glucose	decrease	no trend
Synthesis rate (13C-6)	UDP-N-acetylglucosamine	no trend	no trend
Synthesis rate (15N-2)	UDP-N-acetylglucosamine	decrease (m+1)	increase (m+1) decrease (m+2)

4.5 Upgrade and refinement of iEC2812 yields iEC2997

4.5.1 49 reactions representing 20 trauma metabolites added to iEC2812

The trauma dataset had fold change measurements for 63 metabolites that needed to be included in the model. Of these 63 metabolites, 8 needed to be connected to the model by synthesis, transport and exchange reactions. Another 12 metabolites were already synthesized by the model but needed to have exchange- and/or transport reactions added. 39 metabolites were already fully included in the model and needed no further reactions added. 4 metabolites were not added to the model. **Table 9** shows an overview of these metabolites. The metabolites already available in the model be found in supplementary 4. A total of 49 reactions were added, thereof 18 transport reactions, 19 exchange reactions and 12 synthesis reactions.

Table 9: Overview of metabolites from the trauma dataset and their status in the model upgrade. Table shows metabolites that were connected to the model by synthesis, transport and exchange reactions, metabolites that were already included in the model but needed exchange- and/or transport reactions and the metabolites that were not added to the model.

Connected to the model:	Added exchange/transport:	Not added:
12(S)-HETE	L-Aspartic acid	14-HDoHE
15(S)-HETE	L-Kynurenine	Eicosapentaenoic acid
13(S)-HODE	N,N-dimethylglycine	Trimethylamine N-oxide
12(13)-DiHOME	N,N-dimethylglycine	Decanoylcarnitine
13-OxoODE	5-Oxoproline	
Butyrylcarnitine	a-Ketoglutarate	
Octanoylcarnitine	Fumaric acid	
Hexadecenoic acid	Malic acid	
	Carnitine	
	Acetylcarnitine	
	Propionylcarnitine	
	Palmitoylcarntine	

4.5.2 20 reactions representing 7 ASGR1 metabolites added to iEC2812

After the exclusion of the metabolites that could not be used (discussed in chapter 3.4.2), 44 metabolites were left. Thereof, 2 were connected to the model by synthesis, transport and exchange reactions. Another 5 metabolites were already synthesized by the model but needed to have exchange- and/or transport reactions added. 13 metabolites were already fully included in the model and needed no further reactions. 24 metabolites were not added to the model. **Table 10** shows an overview of these metabolites. The metabolites already available in the model be found in supplementary 4. A total of 20 reactions were added, thereof 9 transport reactions, 9 exchange reactions and 2 synthesis reactions.

Table 10: Overview of metabolites from the ASGR1 dataset and their status in the model upgrade. Table shows metabolites that were connected to the model by synthesis, transport and exchange reactions, metabolites that were included in the model but needed exchange- and/or transport reactions and the metabolites that were not added to the model.

Connected to the model:	Added exchange/transport:	Not added:
Ribitol	Glycerol	Total lactosylceramide
3-hydroxy-5-cholestenoic acid	Glycerol-3-Phosphate	Lysophosphatidylethanolamine
	Total dihydroceramide	gamma CECH
	Sphingosine	2-Aminophenol sulfate
	Choline Phosphate	3-indoxyl sulfate
		Alpha-hydroxyisovalerate
		Androsterone sulfate
		Dimethyl sulfone
		DSGEGDFXAEGGGVR
		Glycylglycine
		Glycilvaline
		Lysylglutamine
		Phenylalanylleucine
		Phenylalanyltryptophan
		Prolylproline
		Aspartylphenylalanine
		Methylsuccinate
		N-acetylglycine
		Histidyltryptophan
		Tryptophylasparagine
		Tyrosylglutamine
		N6-succinyladenosine
		3-ureidopropionate
		Arabinose

4.5.3 EGL synthesis was manually incorporated to iEC2812

4.5.3.1 HS, CS, KS and HA represent the EGL in the ratios of 4:1:0,5:0,5

The building blocks needed to synthesize the EGL were identified to be heparan sulfate (HS), chondroitin sulfate (CS), Keratan sulfate (KS) and hyaluronic acid (HA). Exploration of RECON2.2 showed five CS subtypes (a, b, c, d and e), all synthesized from the same chondroitin sulfate precursor (cs_pre[g]) and UDP-N-acetylglucosamine. Exploration of RECON2.2 also showed three KS subtypes (I, II-core-2 linked and II-core-4 linked), all were synthesized from different KS precursors. While CS and KS have various subtypes, HS and HA each have one subtype.

All of the subtypes were included in the model, but synthesis reactions and precursor reactions were missing. For example, KSI and KSII core-4 had no producing reactions. The greatest amount of reactions were missing for KS synthesis. Many precursors had to be added to the model for EGL synthesis. Also, primary linkers (core proteins) had to be added to the model.

Because of unequal numbers of subtypes between EGL building blocks, reactions that produce each building block were designed and added to the model, these reactions are shown in **Table 11**. With the addition of these reactions, each building block is represented by one metabolic component that can enter the EGL synthesis reaction.

Table 11: Reactions that produce each building block of the EGL. The [e] stands for extracellular. Chondroitin sulfate has 5 subtypes and each of them represents 0,2 parts of the synthesized CS[e]. Keratan sulfate has 3 subtypes and each of them represents 0,33 parts of the synthesized KS[e]. Heparan sulfate and hyaluronic acid each have one subtype which represent the synthesized HS[e] and HA[e].

Building block	Producing reaction
Heparan sulfate	hspg[e] -> HS[e]
Chondroitin sulfate	0.2 cspg_a[e] + 0.2 cspg_b[e] + 0.2 cspg_c[e] + 0.2 cspg_d[e] + 0.2 cspg_e[e] -> CS[e]
Keratan sulfate	0.33 ksi[e] + 0.33 ksii_core2[e] + 0.33 ksii_core4[e] -> KS[e]
Hyaluronic acid	ha[e] -> HA[e]

Literature review of 11 articles (supplementary 4) lead to the decision that HS should be the major building block. A comprehensive review article(2) said that it represented 50% - 90% of the GAGs in the EGL and in the literature review it was almost always the major building block. Chondroitin sulfate was recognized to be the second most common building block, and that it should be in the ratio of 3:1 or 4:1 (HS:CS). Evidence suggested that HA should represent far less amounts than HS. Information on KS synthesis was harder to find so it was decided it should represent the same amount as HS to avoid overrepresentation. The final ratios were: 4 HS, 1 CS, 0,5 KS and 0,5 HA.

4.5.3.2 EGL synthesis was designed and incorporated manually

Exploration of RECON2.2 revealed that it did not contain synthesis of the EGL, rather it had transport reactions for each subtype from the Golgi system to the extracellular space. In reality, a reaction synthesizing the EGL isn't a real quantitative reaction, rather the building blocks are secreted and/or attached to the cell membrane or to other EGL components to form the EGL. An EGL synthesis

reaction is therefore a pseudo reaction necessary to represent the EGL in the model. The EGL synthesis reaction was designed to include all the building blocks from **Table 11** in the decided ratios.

4.5.3.3 EGL estimated to represent 5% out of total biomass weight

The biomass function is a reaction that consumes metabolites (biomass precursors) in fixed ratios in the unit mmol/grams dry weight/hour (mmol/gDW/hour), representin the metabolites required by the cell for maintenance and gowth. Prior to EGL addition to the biomass function, the proportion of EGL weight out of the total biomass function weight was estimated. The endothelial cell is approximately 1-2µm in depth and the EGL ranges from being 0.1-1µm in length [ref?]. For calculations the EGL was estimated to be at its smallest (0.1µm length) and the cell at its biggest (2µm depth) to avoid overestimating EGL weight, making the total height of cell + EGL = 2,1µm. The proportion of the EGL was therefore estimated at: 0,1µM (EGL length)/2,1µM (cell+EGL length) = 0,05 = 5%.

According to these calculations the EGL accounts for 5% of the total mass of the biomass function. The total mass of the metabolites in the biomass function is 27,79 grams/dry weight (g/DW) when ATP is excluded. ATP was excluded from calculations on the grounds that is an energy component that is constantly being produced and consumed, rather than forming cell mass. The EGL biomass was calculated to be 1.38g/DW (5% of 27.79).

When EGL weight had been estimated, a new biomass function including the EGL was added to the model and was made to be the models new objective reaction. The original biomass function that did not include the EGL was deleted from the model. **Figure 28** shows how the EGL synthesis reaction was designed and incorporated into the biomass function. **Table 12** shows detailed values for EGL biomass contribution.

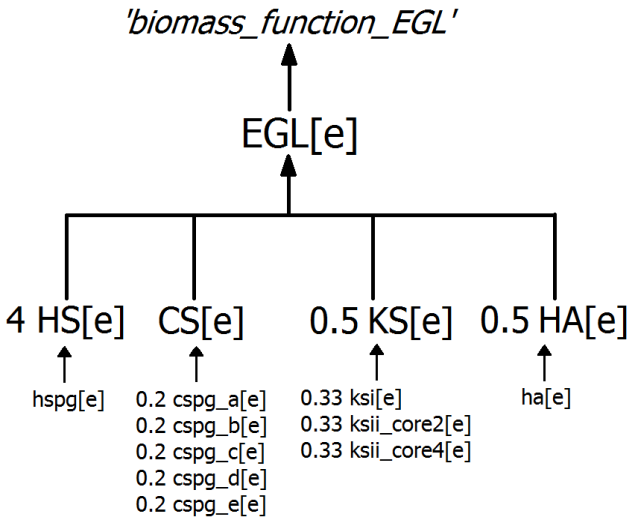

Figure 28: Computational design of the EGL synthesis reaction and EGL incorporation to the biomass function. Synthesis of EGL building blocks takes place like displayed in **Table 11**. The EGL building blocks are consumed in the decided ratios to synthesize the EGL. The EGL is finally incorporated into the biomass function.

Table 12: The calculated contribution of EGL building blocks to biomass weight. Overview of the EGL building blocks, the decided ratios for their synthesis, calculated EGL ratios (e.g. HS represents 66% of the EGL), the part of each building block out of the biomass function in g/DW and the consumption for biomass synthesis in g/DW.

Building block	Ratios	EGL ratio	Part of biomass (g/DW)	Consumption for biomass (g/DW)
HS	4	0,66666666	0,92640023	-0,92640023
KS	0,5	0,08333333	0,11580002	-0,11580002
CS	1	0,16666666	0,23160005	-0,23160005
HA	0,5	0,08333333	0,11580002	-0,11580002
Total	6	1	1,38960035	-1,38960035

4.5.4 Final model upgrade and refinement overview

The model was updated stepwise by addition of metabolites and reactions for the trauma dataset, next the ASGR1 dataset and finally EGL synthesis. The final model has 2997 reactions and 2105 metabolites. **Table 13** shows the number of reactions and metabolites in the model at each stage of model upgrade. MATLAB codes for reaction addition (trauma, ASGR1 and EGL), EGL synthesis, EGL literature review and biomass incorporations, along with calculations for biomass incorporation and list of metabolites already available in the model can be found in supplementary appendix 4. List of all reactions added to the model can be found in supplementary appendix 7.

Table 13: Overview of the model upgrade process showing the number of reactions and metabolites incorporated to the model. The number of metabolites and reactions incorporated between model updates not only represent the metabolites connected to the models, but also their necessary precursors.

Model	Reactions	Metabolites
iEC2812	2812	1979
Trauma dataset incorporation	2861	2013
ASGR1 dataset incorporation	2918	2038
EGL synthesis incorporation	2997	2105
iEC2997	2997	2105

4.6 Trauma and ASGR1 model analysis

When the models had been generated from trauma and ASGR1 datasets as explained in section 3.6.1 they were analysed in order to investigate differences in metabolism between trauma patients and healthy controls, and between ASGR1 carriers and non-carriers. Results are presented below.

4.6.1 Flux analysis

Flux analysis was carried out by analysing upregulated, downregulated and reversed reactions between subject and controls, and by generating flux images. Analysis were all based on means of flux distributions obtained from random sampling. MATLAB codes and lists of reactions can be found in supplementary appendix 5.

4.6.1.1 Flux comparisons show differences between subject and control models

In order to extract up- and downregulated reactions between subject and control models, flux comparisons were carried out like explained in section 3.6.2.1. **Table 14**, **Table 16**, and **Table 18** show results for upregulated, downregulated and reversed reactions in trauma patients as compared to their matched controls (healthy controls). **Table 15**, **Table 17**, and **Table 19** show the same results for ASGR1 variant carriers as compared to their matched controls (non-carriers).

Table 14: Reactions upregulated in trauma patients as compared to matched controls. Table shows flux fold differences, the mechanism of the reaction and the reaction name in the model in brackets, and corresponding gene IDs. In calculations for upregulation, reactions that display values higher than 100 are upregulated by a factor of 100 or more. A total of 5 reactions were upregulated, they are displayed in a row of decreased upregulation.

Flux fold difference	Reaction	Gene ID
223,6881878	Ganglioside synthesis (ST6GALNAC61)	ST6GALNAC6
221,8591187	Ganglioside synthesis (ST8SIA51g)	ST8SIA5
157,3443872	Production of DAG second messenger (PI4PLC)	PLC
148,4066881	Sialyl(2,3)sialyl(2,6)galactosylgloboside transport (ACN23ACNGALGBSIDEtg)	NaN
105,8064292	Catabolism of extracellular adp to amp (ATPH2e)	ENTPD

Table 15: Reactions that are upregulated in ASGR1 variant carriers as compared to non-carriers. Table shows flux fold differences, the mechanism of the reaction and the reaction name in the model in brackets, and corresponding gene IDs. In calculations for upregulation, reactions that display values higher than 100 are upregulated by a factor of 100 or more. A total of 3 reactions were identified as being upregulated.

Flux fold difference	Reaction	Gene ID
975,6421101	Hydroxylation of phenylalanine to tyrosine (PHETHPTOX2)	PAH
289,2592722	Synthesis of KSI (G14Tg)	B4GALT
217,9272303	Synthesis of KSI (AG13T10g)	B3GNTL1

Table 16: Reactions downregulated in trauma patients as compared to matched controls. Table shows flux fold differences, the mechanism of the reaction and the reaction name in the model in brackets, and corresponding gene IDs. In calculations for downregulation, reactions that display values between 0 and 0,1 are downregulated by a factor of 100. A total of 214 reactions were downregulated, the table displays the 15 most downregulated reactions. Reactions are displayed in a row of decreased downregulation.

Flux fold difference	Reaction	Gene ID
1,54E-14	Catabolism of extracellular ATP (ATPH1e)	ENTPD
1,93E-14	Cleavage of AMP to adenosine (NTD7e)	NT5E
0,000443396	De novo purine (adenine) synthesis (ADSL2)	ADSL
0,000443396	De novo purine (adenine) synthesis (AICART)	ATIC
0,000443396	IMP biosynthesis, adenine precursor (PRFGS)	PFAS
0,000443396	De novo purine synthesis (GLUPRT)	PPAT
0,000443396	Purine (adenine) synthesis (AIRcr)	PAICS
0,000443396	Purine (adenine) synthesis (PRAIS)	GART
0,000443396	Purine (adenine) synthesis (IMPC)	ATIC
0,000443396	Purine (adenine) synthesis (PRASCS)	PAICS
0,000443396	Purine (adenine) synthesis (PRAGSr)	GART
0,000443396	Purine (adenine) synthesis (GARFT)	GART
0,005646246	Production of NADH (ALDD2x)	ALDH
0,006250008	Acetaldehyde production (r0186)	NaN
0,006939938	NADPH production (ALDD2y)	ALDH

Table 17: Reactions that are downregulated in ASGR1 variant carriers as compared to non-carriers. Table shows flux fold differences, the mechanism of the reaction and the reaction name in the model in brackets, and corresponding gene IDs. In calculations for downregulation, reactions that display values between 0 and 0,1 are downregulated by a factor of 100. One reaction was identified as being downregulated.

Flux fold difference	Reaction	Gene ID
0,007933289	Norepinephrine sulfate transport (diffusion)	NaN

Table 18: Reactions that are reversed between trauma patients and matched controls. Table shows flux fold differences, the mechanism of the reaction and the reaction name in the model in brackets, and corresponding gene IDs. In calculations for reversibility, reactions that have minus values have changed their flux directions between models. A total of 4 reactions had flux fold changes higher than -100.

Flux fold difference	Reaction	Gene ID
-329,139762	Biosynthesis of glycosphingolipids (GALGT2)	B4GALNT1
-173,6488573	Globoside synthesis (s2l2n2m2mXl)	B3GNT3
-107,603889	Glycan transport (s2l2n2m2mXl)	NaN
-100,7105913	Breakdown of KSI (NACHEX11ly)	HEXA/B

Table 19: Reactions that are reversed between ASGR1 variant carriers and non-carriers. Table shows flux fold differences, the mechanism of the reaction and the reaction name in the model in brackets, and corresponding gene IDs. In calculations for reversibility, reactions that have minus values have changed their flux directions between models. A total of 4 reactions were identified as being reversed.

Flux fold difference	Reaction	Gene ID
-420,5923666	Natrium-dependent antiport of glycine and tyrosine (r1678)	NaN
-163,1045754	Reversible transport of GDP between golgi and cytosol (GDPtg)	NaN
-123,2513747	Synthesis of KSI (S6T13g)	CHST6
-113,112557	GMP dependent transport of GDP-L-fucose (GDPFUCtg)	NaN

4.6.1.2 Flux analysis highlight differences in central carbon metabolism between trauma patients and healthy controls

Because the flux balance analysis in the previous section can be biased on account of the biomass function, we analysed models further by random flux sampling. Flux images were manually generated as explained in chapter 3.6.2.1 to visualize differences in central carbon metabolism between the trauma patient model and healthy control model. **Figure 29** is a compilation of a central carbon flux image and accompanying flux histograms. The flux image demonstrates differences in central carbon metabolism where the blue arrows represent higher flux for healthy controls, red arrows represent higher flux for trauma controls, and grey arows represent no measured flux in either model.

Healthy controls show greater flux of glucose (reaction 1) into the cytosol but the production of glucose-6-phosphate (G6P) from glucose (first step of glycolysis, reaction 3) was more in patients. The patients oxidized G6P in greater amounts into the phentose phosphate pathway, while the controls directed G6P in greater amounts to produce fructose-6-phosphate (F6P), which they directed in greater amounts into the hexosamine biosynthetic pathway, producing precursors for the EGL.

Glycolysis then proceded similarly in both models and diverted again in the lower half. The production of pyruvate from phosphoenolpyruvate (PEP, reaction 5), the transport of pyruvate into the mitochondria (reaction 6), and the production of acetyl-Coa in the mitochondria all showed greater flux for controls. The transport of citrate to the cytosol (reaction 9) and its utilization in fatty acid synthesis was also greater for controls, but the production of citrate from acetyl-CoA (reaction 7) has higher flux for patients than controls. As can be seen on histogram no. 7, the peaks of flux distribution are similar on the x-axis but the patients have a wider distribution. Another two reactions in the TCA cycle had greater flux for the patients, the production of α-ketoglutarate and succinate. Both models have upregulated reactions in the TCA cycle but the controls had greater flux of carbons into the cycle. The highlights here are that the controls had higher fluxes of carbons into the hexosamine biosynthetic pathway, the TCA cycle and fatty acid synthesis. Also, the patients had higher fluxes into the pentose phosphate pathway and for the production of citrate from acetyl-Coa and oxaloacetate.

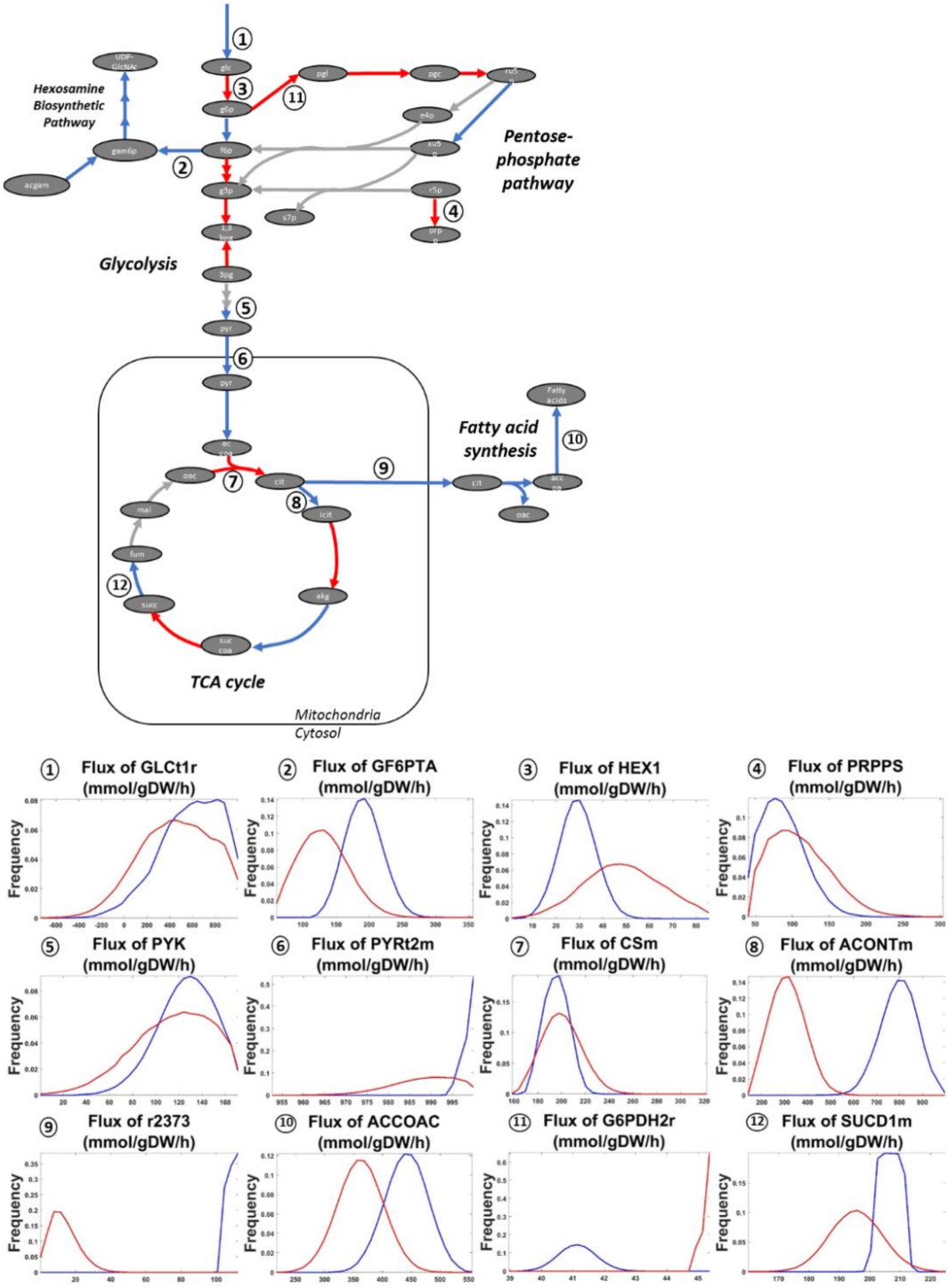

Figure 29: Flux image of central carbon metabolism highlights differences between trauma patient and healthy control model metabolism. Blue arrows and histogram lines represent higher mean flux values for healthy controls, red arrows and histogram lines represent higher mean flux values for trauma controls. Grey arrows represent no flux in either model. Numbered reactions on the flux image refer to their flux histograms below the image. The flux histograms show the distributions of flux values for 5000 points random sampling. The x-axis represents the flux values and the y-axis represents the frequency of each flux value. The histogram titles refer to the reaction names in the model.

4.6.1.3 Flux analysis show major differences in EGL metabolism between trauma patients and healthy controls

Differences in EGL metabolism between the trauma patient model and healthy control model were visualized by generating a flux image. **Figure 30** is a compilation of an EGL metabolism flux image and accompanying flux histograms. The flux image demonstrates differences in central carbon metabolism where the blue arrows represent higher flux for healthy controls and red arrows represent higher flux for trauma controls.

The production of UDP-N-acetylglucosamine from G6P (reaction 1 and the following 2 reactions) has higher flux for healthy controls. The transport of UDP-N-acetylglucosamine from the cytosol to the golgi (reaction 4) and its utilization for EGL synthesis (reaction 6, 7, 8, 9, 10) has higher flux for healthy controls, furthermore the production of UDP-glucuronate from UDP-glucose and its transport from the cytosol into the golgi (reactions 11 and 12) also has higher flux for the controls. The only reaction with higher flux for trauma patients is the utilization of N-acetylglucosamine derived from EGL breakdown to synthesize N-acetylglucosamine-6-Phosphate.

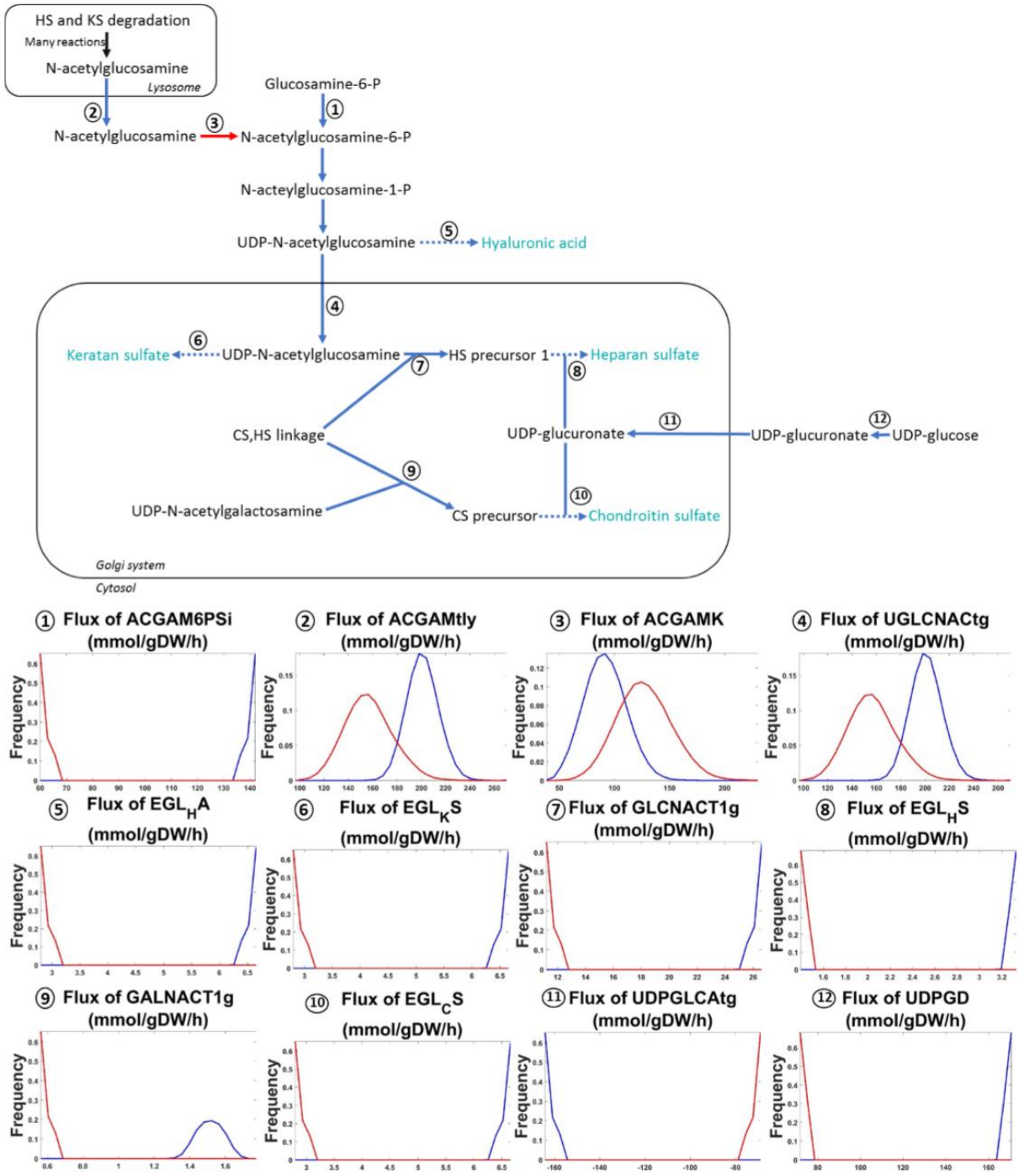

Figure 30: Flux image of EGL metabolism highlights differences between trauma patient and healthy control model metabolism. Blue arrows and histogram lines represent higher mean flux values for healthy controls, red arrows and histogram lines represent higher mean flux values for trauma controls. Grey arrows represent no flux in either model. Numbered reactions on the flux image refer to their flux histograms below the image. The flux histograms show the distributions of flux values for 5000 points random sampling. Healthy controls are represented by blue lines and trauma patients by red lines. The x-axis represents the flux values and the y-axis represents the frequency of each flux value. The histogram titles refer to the reaction names in the model.

4.6.1.4 Flux analysis highlight a difference in the hexosamine biosynthetic pathway between ASGR1 variant carriers and non-carriers

Differences in central carbon metabolism between ASGR1 carrier model and non-carrier model was visualized with the same methods as the trauma models. **Figure 31** is a compilation of a central carbon flux image and accompanying flux histograms. Blue arrows represent higher flux for non-carriers, red arrows represent higher flux for ASGR1 variant carriers, yellow arrows represent no flux differences and the grey arrows represent no measured flux in each of the models.

The transport of glucose into the cytosol was the same for both models, but the production of G6P from glucose (reaction 1) had higher flux for carriers. The non-carriers utilized G6P in greater amounts for the pentose phosphate pathway (reaction 5), and the flux of G6P into F6P was greater for non-carriers (reaction 2). Furthermore, the flux of F6P into the hexosamine pathway was greater for non-carriers (reactions 3 and 4), which represented the greatest flux difference observed here. Many of the reactions in glycolysis and the TCA cycle had the same fluxes for both models (yellow), e.g. the transport of pyruvate into the mitocondria and its consumption for acetyl-CoA production. The carriers had greater flux for the transport of citrate from the mitocondria to the cytosol (reaction 8) and also greater flux of acetyl-CoA into fatty acid synthesis (reaction 9). The production of α-ketoglutarate (reaction 10) had greater flux for non-carriers. The main result here is the far greater flux of carbons into the hexosamine biosynthesis pathway for non-carriers.

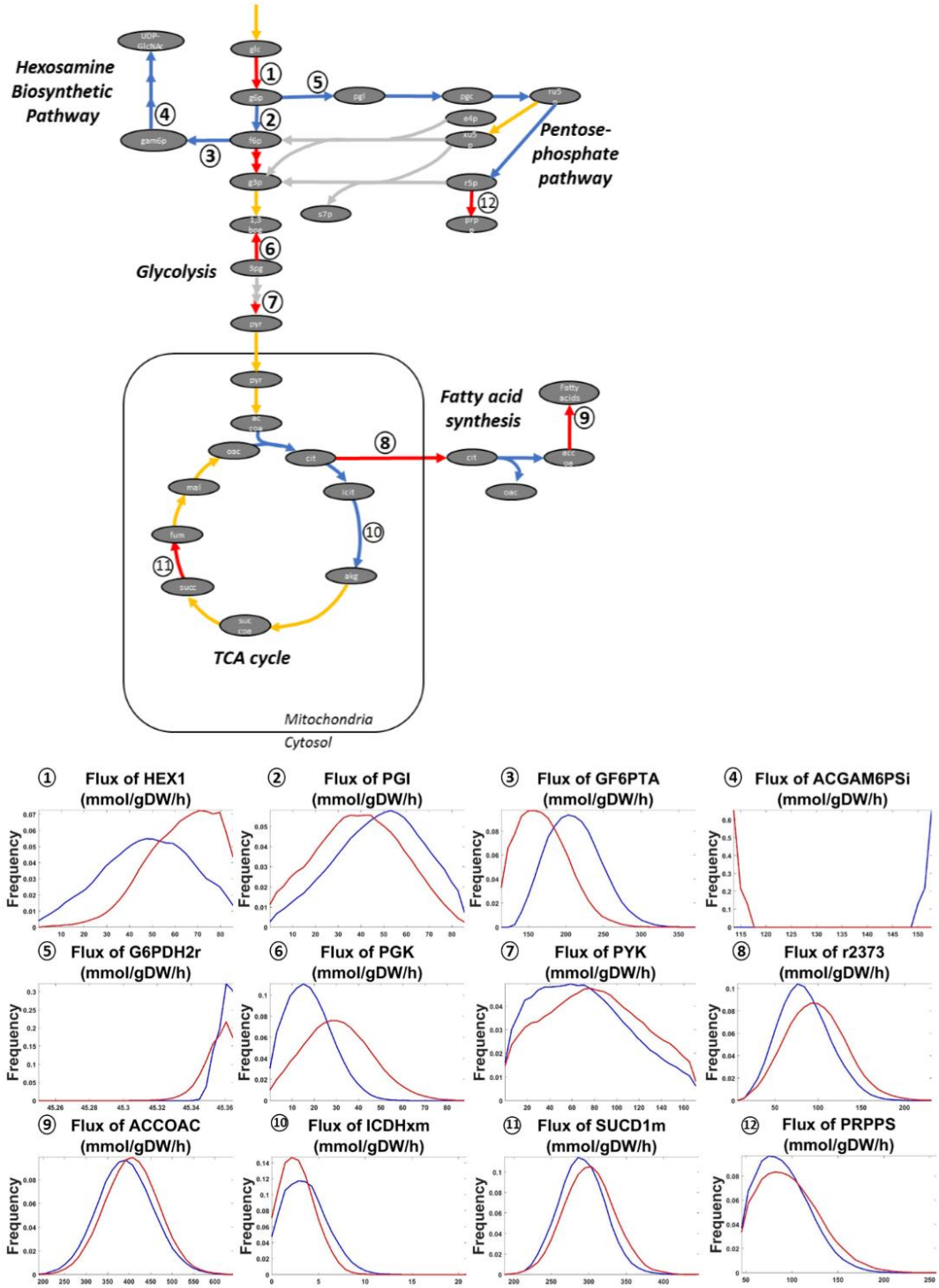

Figure 31: Flux image of central carbon metabolism highlights differences between ASGR1 carrier and non-carrier model metabolism. On the flux image, the blue arrows represent higher mean flux values for non-carriers and red arrows represent higher mean flux ASGR1 variant carriers. Numbered reactions on the flux image refer to their flux histograms below the image. The flux histograms show the distributions of flux values for 5000 points random sampling. Non-carriers are represented by blue lines and ASGR1 carriers by red lines. The x-axis represents the flux values and the y-axis represents the frequency of each flux value. The histogram titles refer to the reaction names in the model.

4.6.2 MOMA and FEA analysis

To further analyse differences in metabolism between subject and control models MOMA and FEA analysis were carried out like explained in sections 3.6.2.2 and 3.6.2.3. All codes, calculations and results can be found in supplementary appendix 6.

4.6.2.1 N-Glycan and CS/HS synthesis are highlighted as differentiating between trauma and controls

Figure 32 shows results from MOMA and FEA analysis on subsystems. The CS/HS synthesis and N-glycan synthesis subsystems had the greatest overrepresentation. Exchange/demand reactions are the third most overrepresented, followed by cholesterol metabolism and nuclear transport. IMP synthesis, heme synthesis, carnitine metabolism and linoleate metabolism also show some overrepresentation.

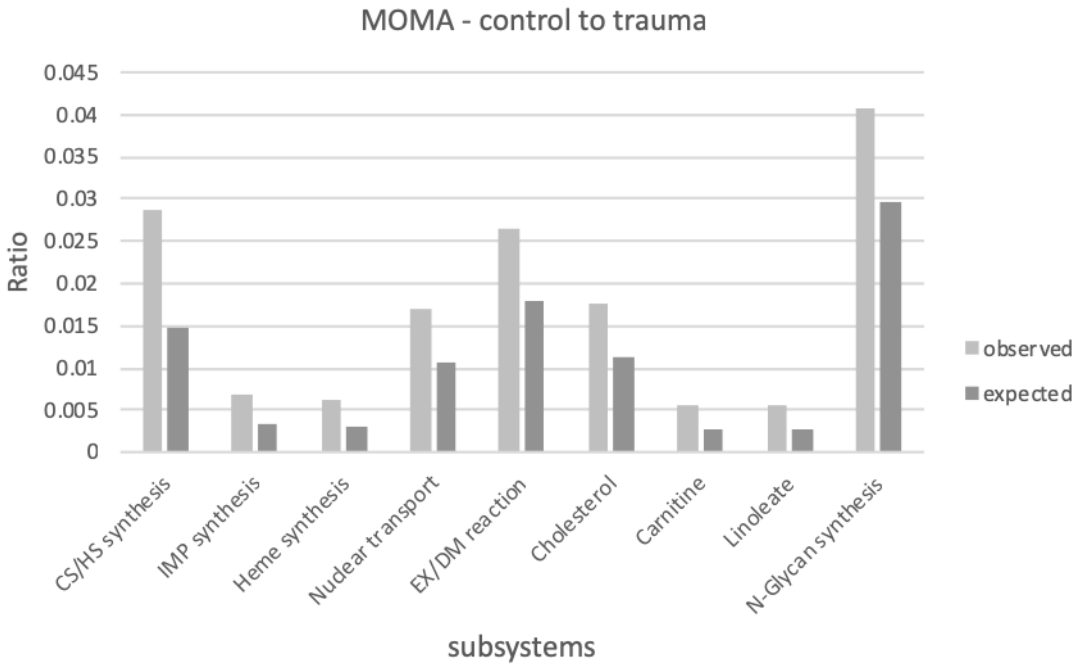

Figure 32: MOMA and FEA highlight CS/HS synthesis and N-glycan synthesis to differentiate between trauma patient and healthy control model metabolism. The y-axis represents the subsystems that are overrepresented and have an adjusted p-value<0.05 when the healthy control model is pushed to become more like the trauma patient model. They are the subsystems that include the greatest amounts of reactions that need alteration in order for that to happen.

4.6.2.2 The SLC7A6 gene is highlighted as differentiating between trauma and controls

Figure 33 shows results from MOMA and FEA analysis on genes. The solute carrier family 7 member 6 gene had the greatest overrepresentation out of the 3 genes that were overrepresented. Folylpolyglutamate synthase, aldehyde dehydrogenase and nucleoside diphosphate kinase 1 and 2 were also overrepresented, but to a less extent.

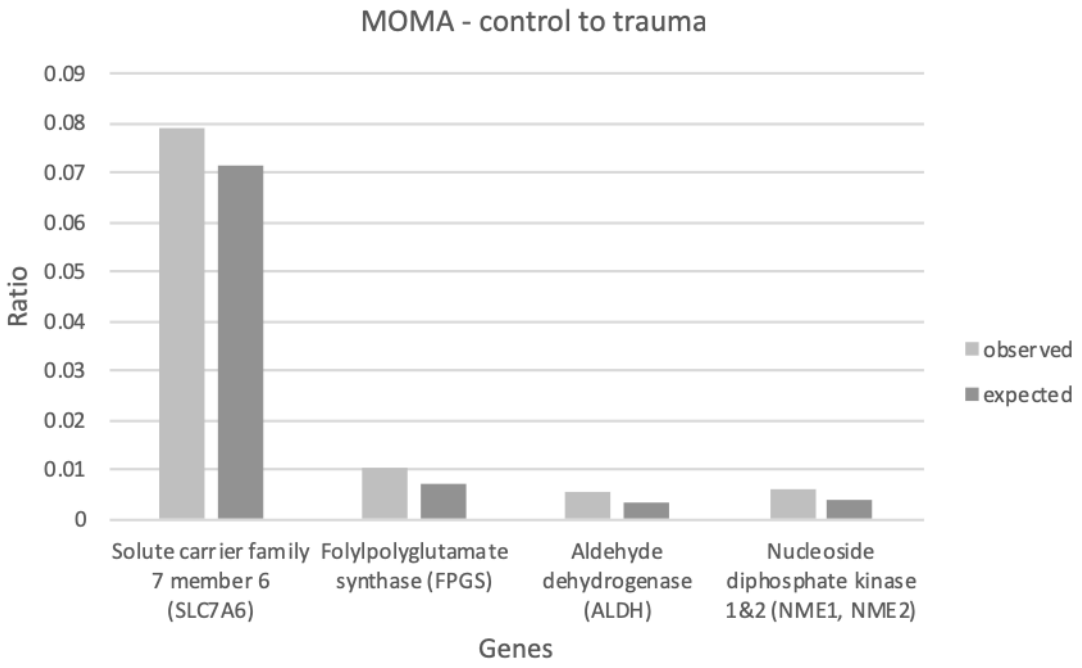

Figure 33: MOMA and FEA highlight the SLC7A6 gene as differentiating between trauma patient and healthy control model metabolism. The y-axis represents the genes that have an adjusted p-value<0.4 when the healthy control model is pushed to become more like the trauma patient model.

4.6.2.3 N-Glycan synthesis is highlighted as differentiating between ASGR1 variant carriers and non-carriers

Figure 34 shows results from MOMA and FEA analysis on subsystems. The N-glycan synthesis subsystem has the greatest overrepresentation. The subsystem that comes next is glycerophospholipid metabolism, which is followed by cholesterol-, urea/cycle amino group- and inositol phosphate metabolism. Heme synthesis, fructose and mannose-, carnitine- and linoleate metabolism also show some degree of overrepresentation.

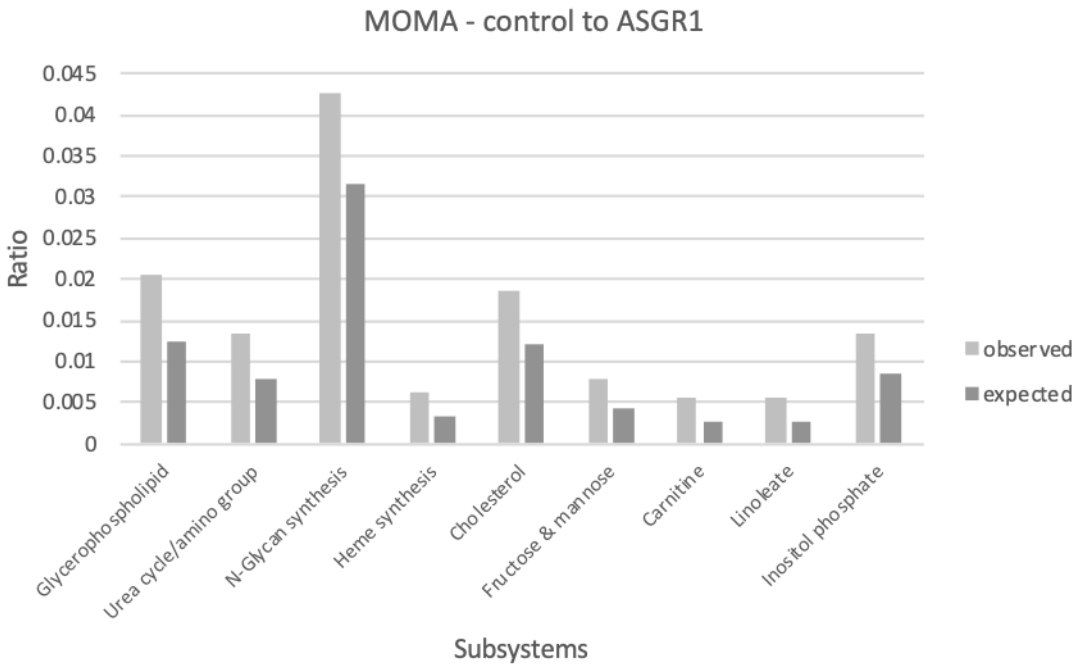

Figure 34: MOMA and FEA highlight N-Glycan synthesis to differentiate between ASGR1 variant carrier and non-carrier metabolism. The y-axis represents the subsystems that have an adjusted p-value<0.05 when the non-carrier model is pushed to become more like the trauma patient model. They are subsystems that include the greatest amounts of reactions that need alteration in order for that to happen.

4.6.2.4 The FPGS, ALDH and NME1/2 genes are highlighted as differentiating between ASGR1 variant carriers and non-carriers

Figure 35 shows results from MOMA and FEA analysis on genes. Folylpolyglutamate synthase (FPGS) has the greatest overrepresentation. Aldehyde dehydrogenase and nucleoside disphophate kinase 1 and 2 also showed overrepresentation.

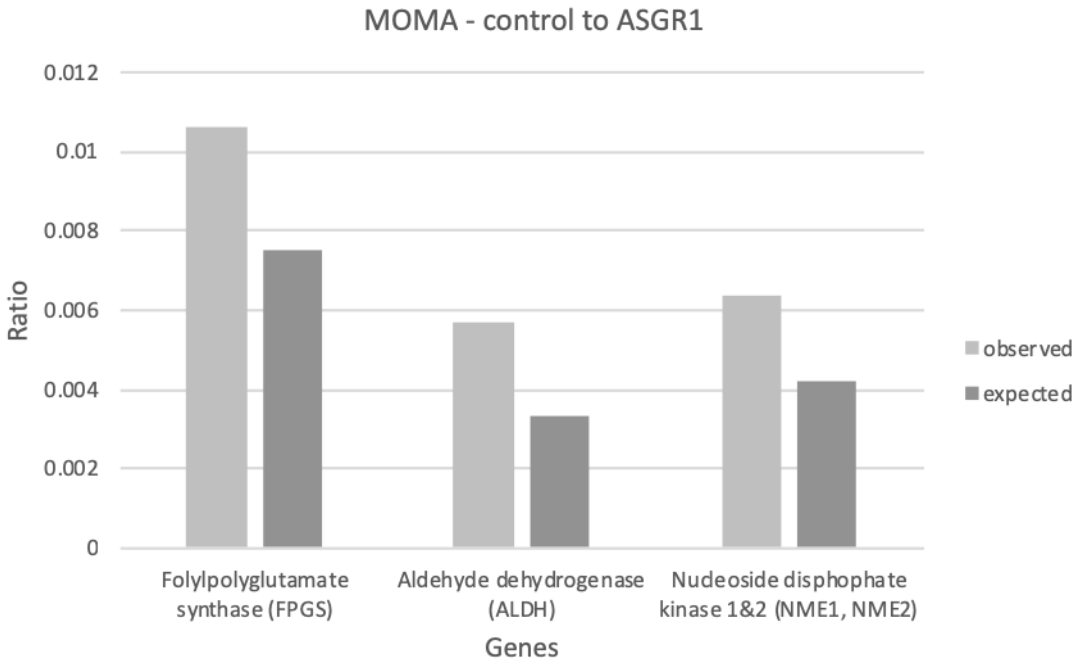

Figure 35: MOMA and FEA highlight the FPGS gene as differentiating between ASGR1 variant carrier and non-carrier model metabolism. The y-axis represents the genes that have an adjusted p-value<0.4 when the non-carrier model was pushed to be more like the carrier model.

4.6.3 Biomarker exchange table highlights differences in uptake and secretion of endothelial biomarkers between models

The metabolic models allow biomarkers of endothelial health to be predicted from metabolic phenotypes(49). **Table 20** lists endothelial biomarkers and their uptake or secretion status in trauma and ASGR1 models. The trauma patient model shows decrease in secretion of NO and methoxytryptophan (MTP), and increase in secretion uric acid as compared to the healthy control model. The trauma patient model also shows increased uptake of sphingosine-1-phosphate (S1P) and decreased uptake of GABA.

The ASGR1 variant carrier model has increased secretion of NO and MTP, and decreased secretion of S1P as compared to the non-carrier model. Both model secrete uric acid to the same extent. The carrier model has decreased uptake of GABA. MATLAB codes for the generation of this table can be found in supplementary appendix 7.

Table 20: Biomarker exchange table highlights differences in uptake and secretion of key endothelial health biomarkers. Table lists endothelial biomarkers and if they are secreted or taken up by the control models and if and how uptake and secretion change between controls and subject models. The table shows results for both trauma and ASGR1 models.

Biomarker	Healthy control	Trauma patient	Non-carrier	ASGR1 Carrier
NO	Secretion	Decrease	Secretion	Increase
S1P	Uptake	Increase	Secretion	Decrease
MTP	Secretion	Decrease	Secretion	Increase
GABA	Uptake	Decreased	Uptake	Decreased
Uric acid	Secretion	Increase	Secretion	The same

5 Discussion

The adverse effects on the glycocalyx during trauma are well known and documented, but the role of endothelial and specifically EGL metabolism in that context is not known. What is known is that increased circulatory shed EGL components and catecholamines are observed in trauma patients(17) and that the metabolomic plasma profiles of these patients are different from healthy controls, as recently demonstrated by our collaborators (Henriksen et al., 2019, accepted in Annals of Surgery.). These observed phenotypic differences differentiate between trauma patients and healthy controls and as such have laid the ground for our endothelial research.

We set out to demonstrate the effects of increased catecholamine concentrations such as observed in trauma on endothelial and specifically EGL metabolism. We wished not to explore how the EGL breaks down, rather we were curious about the aftermath of EGL breakdown – what would the effects of increased catecholamines and subsequent EGL breakdown be on the observed metabolism? Furthermore, we set out to investigate endothelial metabolism by using systems biology methods since endothelial research has been haltered by technical difficulties such as difficult access. By utilizing genome-scale constraint-based metabolic modelling, and plasma metabolomics data, we explored how the observed differences in plasma metabolomics between trauma patients and healthy controls affected changes to endothelial metabolism.

TEM images combined with previously carried out experiments within our lab show that catecholamine stimulation of HUVECs *in vitro* does indeed cause EGL loss. Results of metabolic experiments demonstrate that catecholamine stimulation does effect endothelial metabolism, as can be seen in the observation of decreased glycolytic and TCA cycle activity, ATP decrease, cAMP response and the decrease of intracellular concentrations and synthesis rates of EGL precursors as a response to catecholamine stimulation. *In silico* analysis of the metabolic models in many ways concurred with the results from *in vitro* metabolic experiments. 10 downregulated reactions amongst trauma patients were involved in adenosine/purine synthesis, which complements the observed ATP decrease in catecholamine treated cells. Decrease in ATP and glycolytic flux could also go hand in hand. Complementary to *in vitro* metabolic results, flux analysis of central carbon metabolism showed greater flux of carbons into the TCA cycle and the hexosamine biosynthetic pathway (EGL precursor production) for healthy controls than patients. Furthermore, flux analysis showed greater flux for synthesis of EGL building blocks and precursors amongst healthy controls. MOMA and FEA highlighted CS/HS synthesis and N-glycan synthesis along with the SLC7A6 gene to differentiate the most between healthy control and trauma models. Flux analysis for ASGR1 models highlighted the greatest difference in the hexosamine biosynthetic pathway, while MOMA and FEA highlighted N-glycan synthesis and the FPGS gene as differentiating.

5.1 Effects of catecholamines on the EGL phenotype

TEM images did show EGL loss after 4 hours of catecholamine stimulation, with the most visual effects for 10µM and 100µM. The concentrations of catecholamines used in metabolic experiments were 0,5µM, 5µM and 50µM, it is a fair assumption that the concentrations of 50µM (and likely 5µM as well) exert their effects on HUVECs in culture.

5.2 Energy and signalling metabolism is affected by catecholamine stimulation

The investigation of catecholamine effects on energy and signalling metabolites led to the discovery that intracellular ATP decreased at both timepoints, AMP decreased at 4 hours but increased at 24 hours, and that cAMP only showed response after 4 hours of catecholamine stimulation. Results for ATP, AMP and cAMP measurements are outlined in **Table 5**.

The *in silico* flux analysis complement the metabolic results as 12 out of the 15 downregulated reactions in trauma patients as compared to healthy controls were involved in adenine synthesis and extracellular cleavage of ATP/AMP, generating cell permeable adenosine. These results indicate that intracellular ATP decreases because of less ATP synthesis and also suggest that the trauma patient plasma metabolomics have adverse effects on adenine synthesis. Weather the ATP decrease comes from greater consumption or less production is hard to say since these measurements do not say anything about synthesis rates. In conclusion, it is not possible to assert why intracellular ATP decreases as a response to catecholamine stimulation at this timepoint, but it definitely does decrease. The 4 hour decrease and 24 hour increase in AMP concentrations are difficult to understand, and it should be kept in mind that energy metabolism changes with the cells energy needs. Measurements at tighter intervals are likely required to determine accurate fluctuations to ATP and its derivatives.

The increase in cAMP 4 hours after catecholamine stimulation did not come as a surprise since catecholamines are known to activate the production of cAMP through the actions of β-adrenergic receptors(67). It has been demonstrated previously that ECs (human microvascular) stimulated with adrenaline for 15 minutes strongly upregulate their cAMP synthesis(68). The same research group later demonstrated that adrenaline had the same effect on HUVECs which upregulated their cAMP synthesis by 323% after 15 minutes of 100µM stimulation. The cAMP increase in this study was not of the same scale, whereas smaller concentrations of catecholamines were used for stimulation. Importantly, in this thesis cAMP concentrations were measured after 4 hours, when the initial effects of catecholamine stimulation would be diminished. It should be kept in mind that the catecholamines in the media might not all exert their effects at the same time as the medium is static as opposed to flowing like observed *in vivo*. In conclusion, the observed increase in cAMP is most likely due to the prolonged catecholamine exposure of HUVECs in culture.

5.3 Glycolytic activity is decreased following catecholamine stimulation

When the effects of catecholamine stimulation on glycolysis were investigated the most apparent trends were the drop in extracellular lactate and glucose concentration at both timepoints. Results for glucose and lactate measurements are outlined in **Table 6**.

These data demonstrate that lactate and glucose concentrations drop as a response to catecholamine stimulation. This reflects decreased glucose uptake and decreased lactate secretion, which strongly suggest decreased overall glycolytic activity. ECs primarily rely on glycolysis for ATP production, results showed that intracellular concentrations of ATP decrease with catecholamine stimulation, which also might reflect a decrease in glycolytic activity.

Flux analysis of central carbon metabolism (**Figure 29**) showed both trauma patient and control models having upregulated reactions in glycolysis. The reaction of phosphoglycerate kinase (PGK) which normally removes a phosphate group from 1,3-phosphoglycerate to produce 3-phosphoglycerate is misdirected in the model, which interferes with the flow of metabolites through the pathway and makes comparisons of *in silico* and *in vitro* results difficult. This misdirection of PGK renders the two following reactions, phosphoglycerate mutase (PGM) and enolase (ENO) inactive, resulting in an alternative production of PEP. That being said, the curation of the GEM is an ongoing process.

Glucose uptake/lactate secretion ratios decrease from 0µM to 5µM after 4 hours of catecholamine stimulation. The variability of the data makes it difficult to draw any conclusions but they might suggest that sooner rather than later after catecholamine stimulation, lactate is being produced by other means than from pyruvate derived from glucose. A feasible explanation could be that the HUVECs consume pyruvate from the media for lactate production. In experiments not expanded within the thesis, we measured pyruvate from media and showed that HUVECs consume pyruvate from the media.

It can be concluded that catecholamine stimulation causes decreased glycolytic activity, but the mechanism behind this observed effect cannot be asserted at this point in time. A realistic explanation could be that catecholamines indirectly interfere with the transcription of pyruvate kinase (PK), which catalyses the final glycolysis reaction, via the induction of cAMP. It has been demonstrated that cAMP decreases the transcription of pyruvate kinase (PK) by inhibiting a transcription factor of the L-type PK gene(69), therefore interfering with the progression of glycolysis. It has very recently been demonstrated (in mice) that the M2 isoform of PK has a role in maintaining vascular integrity, researchers found that PKM2 suppressed NF-kB and its downstream target, the vascular permeability factor angiopoietin-2 and that loss of PKM2 in ECs predisposed mice to VEGF-induced vascular leak(70). Hence, these processes describe a mechanistic link between decreased glycolytic activity and vascular leakage.

It has been well established that shock states such as trauma are characterized by a hypermetabolic condition with raised blood lactate concentration(71), which does not reflect these results. That being said, the metabolism of a single cell type does not reflect the metabolic state of the entire bodily system. It has been demonstrated that stimulation of HUVECs with bioactive molecules can influence the progression of glycolysis. For example, advanced glycation end products (AGEs)

have been reported to cause decline of glycolytic activity(72), while another study found that stimulation with oxidized phospholipids induced glycolysis(73). These studies demonstrate that metabolism in cultured HUVECs can be influenced with addition of specific reagents. Interestingly, a study using guinea pig hearts found that coronary flow stimulated glycolytic flux, possibly through shearing forces acting upon specific EGL components(74). That being said, the HUVEC culture established in this thesis was static which could have presented a skewed image of their metabolism.

No articles researching the direct effects of catecholamine stimulation on HUVEC glycolysis were found and so these results cannot be evaluated in the context of other results.

5.4 TCA cycle activity is decreased following catecholamine stimulation

The investigation of catecholamine effects on the TCA cycle led to the discovery that intracellular concentrations and in most cases rates of synthesis decreased. Results for TCA cycle intermediates and anaplerotic measurements are outlined in **Table 7**.

A drop in intracellular concentrations of TCA cycle intermediates was observed in all cases, excluding the 50µM measurement of 24 hour citrate and the 5µM measurement of 24 hour succinate.

The observed increase in citrate synthesis after 24 hours might be in accordance with the increase in intracellular concentrations at 24 hours, although the concentration increase was measured for 50µM catecholamines. The dose-dependent decrease in the synthesis of citrate after 4 hours of stimulation suggests slower metabolic activity of the TCA cycle at least at the early stages after catecholamine stimulation.

The observed decrease in intracellular concentrations and synthesis rates of L-glutamine and L-glutamate observed strongly indicate that decreased intracellular concentrations of these metabolites stem from slower synthesis rates. Slower synthesis of these metabolites could also suggests decreased metabolic activity of the TCA cycle, but then again L-glutamine is involved in many metabolic processes so its concentration levels not only reflect the metabolic activity of the TCA cycle(75).

In silico flux analysis further suggest that the TCA cycle flux is a victim of endothelial dysfunction, as healthy controls had far greater shunt of pyruvate into the TCA cycle than the trauma patients. Furthermore, flux analysis of ASGR1 models which both represent healthy endothelium, showed the same shunt of pyruvate into the TCA cycle. This indicates that plasma metabolomics of healthy individuals maintain the normal progression of the TCA cycle.

The decrease in extracellular L-glutamate after 24 hours suggests greater uptake or less secretion as a response to catecholamine stimulation, the measurements had some degree of standard deviation.

Extracellular measurements of L-glutamate had very high degrees of standard deviations and as such are not necessarily significant, despite of that some trends were observed. The elevated concentrations after 24 hours suggest increased secretion rates or decreased uptake as a response to catecholamines. L-glutamine is involved in many biosynthetic, regulatory and energy producing processes(75), and therefore decreased uptake could reflect less metabolic activity within the cell. On

the other hand, increased secretion of L-glutamine could stem from amino acid transporter activities, whereas L-glutamine is often used to transport other amino acids into cells via L-glutamine transporters and antiporters who regulate the balance between pools of glutamine and other amino acids(75). Interestingly, the gene with the greatest overrepresentation in MOMA/FEA analysis for control to trauma was SLC7A6, which happens to belong to the most acknowledged glutamine transporter family(75). Whether the extracellular increase in L-glutamine reflects increased secretion rates or decreased uptake rates as a response to catecholamines is difficult to assert at this point.

In summary, the metabolic *in vitro* experiments and *in silico* analysis demonstrate decreased metabolic activity of the TCA cycle as a response to catecholamine stimulation. The decrease in intracellular metabolite concentrations and the lowered synthesis rates observed are at least strong indicators of decreased metabolic activities, despite some irregularities in results. It is therefore concluded that catecholamine stimulation causes decreased metabolic activity of the TCA cycle. At this point it is only possible to conclude that these changes are observed but the mechanism behind this cannot be asserted.

It has been demonstrated in mouse models that the TCA cycle and mitochondria mass are early victims of endothelial dysfunction(76). Another recent study found that impaired NO production, such as observed in dysfunctional ECs, contributed to impaired TCA cycle activity(77). Decreased metabolic activity of the TCA cycle under trauma-simulated conditions would fall into the same category as these kind of research, whereas the TCA activity is a victim of endothelial dysfunction.

Interestingly, it has recently been demonstrated that TCA cycle activity slows down when cells change from a proliferative to a quiescent state(78), this means that the TCA cycle is upregulated when the cells energy requirements are at its highest. Possibly, cells that are undergoing catecholamine stimulation decrease their energy metabolism to compensate for adverse metabolic effects caused by the stress condition. The ATP results demonstrating decrease in intracellular ATP concentrations after 4 and 24 hours of catecholamine stimulation supports this.

No articles researching the effects of catecholamine stimulation on HUVECs TCA cycle were no found and so these results cannot be evaluated directly in the context of other results.

5.5 Synthesis and concentrations of EGL precursors are affected by catecholamine stimulation

Last but certainly not least, the investigation of catecholamine effects on EGL metabolism led to the discovery that EGL precursors indeed decrease in concentration as a response to catecholamines, and also that their synthesis rates are effected. Results for EGL precursors are outlined in **Table 8**.

According to intracellular concentration measurements, there is less supply of important EGL precursors after catecholamine stimulation, strongly suggesting that EGL synthesis might be halted or slowed sown as a response to the catecholamines.

Measurements of synthesis rates showed a clear dose-dependent decrease of ^{13}C-6 incorporation into UDP-glucose after 4 hours, where no trend was observed after 24 hours. This could suggest that catecholamine effects on glycan metabolism is greater at earlier hours after stimulation. The no trend observed for ^{13}C-6 labelling of UDP-N-acetylglucosamine and the decrease in uniformly ^{15}N-2 labelled

UDP-N-acetylglucosamine after 4 hour stimulation might suggest that the carbon source for production of this metabolite is available when the nitrogen source is sparser. The observed increase in single ^{15}N-2 labelled (m+1) UDP-N-acetylglucosamine at 24 hours suggest that some hours after EGL breakdown, nitrogen sources are used to a greater extent to rebuild GAGs for the endothelial cell surface. The decrease observed in double (m+2) ^{15}N-2 labelled UDP-N-acetylglucosamine shows that at this later timepoint, nitrogens from the labelled glutamine are being incorporated into the UDP moiety of the metabolite, but to a less extent with increased catecholamines.

The catecholamines definitely exert their effects on the synthesis of these metabolites. After the initial stimuli, synthesis of UDP-glucose slows down but is recovered at 24 hours. Synthesis of UDP-N-acetylglucosamine suggest carbons are readily available for its synthesis, but that nitrogen sources are sparse after the initial stimuli, but are recovered at later timepoints. The double ^{15}N-2 labelled UDP-N-acetylglucosamine after 24 hours also goes to show that the synthesis of this metabolite is recovered at later timepoints and more so with less catecholamine stimulation, since no double labelled molecules are measured at 4 hours. In summary, the effects of catecholamine stimulation exert their effects on the synthesis of EGL precursors at earlier stages after stimulation, with synthesis rates recovering over time. In agreement to these results, *in silico* flux analysis of central carbon metabolism showed greater flux of carbons into the hexosamine biosynthetic pathway (producing EGL precursors) for healthy controls than trauma patients. Flux analysis also showed greater flux of carbons into production of EGL precursors and building blocks in all cases for healthy controls.

According to this data, EGL metabolism is affected by catecholamine stimulation, more so at earlier hours after stimulation, and by the plasma metabolome as well. It is concluded that catecholamine stimulation and possibly the plasma metabolomics of trauma patients halt the production of these EGL precursors.

It has previously been demonstrated that treatment of ECs with bioactive molecules affect the synthesis rates of GAGs. Treatment of bovine glomerular ECs with a nephrosis-inducing agent for 72 hours found that GAG synthesis decreased by 31% as compared to normal cells and that treatment with IL-1β increased synthesis by 141%(65). Another study concerned with HUVEC GAG metabolism in response to inflammatory stimuli found that IL-1, TNF, and IFN-gamma influenced sulphated GAG metabolism(55). It has previously been demonstrated that factors in plasma of kidney patients influence GAG metabolism, possibly reflecting decreased turnover rates of GAGs(79). The effect of catecholamines on EGL metabolism has not been researched directly before, at least not to our knowledge, and no articles researching the effects of catecholamines on HUVEC or endothelial EGL metabolism were found, making these results harder to contextualise beyond isolated cells used in our experiments.

5.6 Predictions of NO and MTP exchange directions reflect most likely *in vivo* conditions

Table 20 shows results for predictions of uptake and secretion of known endothelial biomarkers, both of endothelial health or dysfunction. The decreased secretion of NO observed for trauma patients as compared to healthy controls is interesting as endothelial dysfunction is characterized in many cases

by impaired NO synthesis. The SLC7A6 gene (also abbreviated YLAT2) which was highlighted as a difference between healthy controls and trauma patients mediates the uptake of arginine and therefore plays a role in NO synthesis(80). The observed increase in NO synthesis for ASGR1 carriers, which presumably maintain a healthier endothelium than the standard non-carrier is also interesting in this context. Uptake of S1P observed for trauma patients and healthy controls is probably an artefact of the modelling process since it is a lipid mediator that ECs are known to synthesize and secrete, allowing it to exerts its vasculoprotective roles through G-protein coupled receptors(81,82). The decreased secretion of MTP observed in trauma patients would concur with endothelial dysfunction. It has been demonstrated *in vitro* and *in* vivo in murine models that ECs release MTP to protect their barrier function, which are exerted via blockage of p38 MAPK activation(83). MTP has also been demonstrated to block systemic inflammation such as observed in multiorgan injury(84). Interestingly, the supposedly hyper healthy carriers of the ASGR1 variant had an increase in secretion of this vasculoprotective biomarker. The uptake of GABA observed in all four models is probably not very realistic since ECs synthesize and release GABA into the bloodstream where it exerts its vasculoprotective effects such as inhibition of ROS generation(13,14). The increase in uric acid secretion for trauma patients describes endothelial dysfunction, since uric acid induces ECs to release an inflammatory cytokine, inducing oxidative stress and inflammatory responses(86). Although ECs would not necessarily be secreting uric acid in the first place, it is even more unlikely that they would be taking it up seeing as most of it is excreted in urine and the rest is consumed and metabolized by liver cells(87).

The model predicts expected behaviour for two out of five biomarkers, NO and MTP, in the trauma and ASGR1 conditions. It should be kept in mind that excess amounts of otherwise helpful molecules can have negative effects.

5.7 Glycine as a novel vasculoprotective metabolite in trauma

Out of the 24 metabolites not used for generating the ASGR1 models (see **Table 10**), 16 were dipeptides that were not accounted for in our GEM, and neither in RECON1 or 2. Thereof 3 were glycine peptides: glycylglycine, glycilvaline and N-acetylglycine, which all measured higher amongst the ASGR1 variant carriers than non-carriers. Plasma glycine has been shown to be inversely associated with vascular or metabolic disease such as obesity, hypertension, diabetes and acute myocardial infarction, implying that increased circulatory glycine levels are beneficial for the vasculature(88).

It has been demonstrated that glycine is required for purine synthesis to compensate for purine loss in ECs in response to oxidized phospholipids such as produced in atherosclerosis. Researchers further proposed that ECs undergo methylenetetrahydrofolate dehydrogenase (MTHFD2)-mediated reprogramming toward serine-glycine and mitochondrial one-carbon metabolism to compensate for loss of ATP in response to oxidized phospholipids formed during atherosclerosis(89). Interestingly, FPGS was overrepresented in MOMA and FEA analysis between ASGR1 variant carriers and non-carriers. FPGS is involved in one-carbon metabolism, where it catalyzes the conversion of folates to polyglutamate derivatives which are consumed for purine synthesis. It just so happens that glycine is

used in the synthesis of polyglutamate derivatives as well. These publications might suggest a link between levels of glycine in plasma and one-carbon metabolism.

The natrium-dependent antiport of glycine and tyrosine (reaction r1678) was identified as the reaction that had been reversed the most between ASGR1 variant carriers and non-carriers, flux analysis of this reaction showed that carriers secreted glycine in far greater amounts.

The literature and the analysis of the ASGR1 models suggest that increased glycine levels aid in endothelial health and as such glycine would be an intresting metabolite to investigate in that context. To do so, ECs in culture could be stimulated with catecholamine in the presence of heavy isotope nutrient labelling to investigate glycine synthesis in endothelial dysfunction like conditions.

5.8 Pros, cons and future studies

Generating and continuing to improve a GEM for endothelial metabolism should be considered to be of great importance since research on the endothelium has been haltered due to technical difficulties. A well-built GEM should be able to elucidate many of the cells mechanisms and predict outcomes of experiments and in that way minimize the cost of endothelial research. To our knowledge, iEC2997 is the only endothelial cell-specific GEM that has been generated using transcriptomic data and extent of manual curation. It is not the only endothelial specific GEM, but Patella et al generated one in 2015, using proteomics data(12). Furthermore, iEC2997 has already been used in a study that has been accepted for publication in Annals of surgery, the world's most referenced surgery journal. The GEM is not perfect but its predictive power is quite impressive as can be seen from this thesis results, and it can only be improved from this point on.

A downside to this study, as with many cell focused studies is that the cells have been taken out of their natural habitat, which in this case is quite special due to circulatory shear stress and the dense one-layered morphology of the cells. Therefore, an obvious fault in this research is the static HUVEC cell culture used to collect endothelial data since ECs change their morphology whilst exposed to shear stress in the circulatory system(90). We opted to set up a flow model using a specialized pump system and cell culture plates from Ibidi to conduct the metabolic experiments, but technical difficulties stood in the way. Establishing a flow model for collection of metabolic data would be the preferred method as the metabolic measurements would probably represent real life metabolism better. Another downside to using HUVECs is that every experiment uses cells from a different donor, which is a source of variability between measurements.

By generating a GEM for a more biologically relevant endothelial cell type reflecting the circulatory system better, and establishing a flow model to collect metabolic constraint data from cells under flow, a more specific and predictive endothelial model could be generated. Human pulmonary microvascular ECs (HPMECs) would be ideal for the study of trauma as endothelial dysfunction in the pulmonary microvasculature contributes to lung failure, a significant cause of death in many forms of shock(91).

In order to analyse the metabolomics plasma data, it is assumed that the metabolites are exclusively the products of or nutrients for ECs, when e.g. immune cells and platelets also exert their effects on the plasma metabolome as they also maintain metabolism. An idea to compensate for this

is the collection of metabolic data from ECs that have been treated with 10-20% plasma from healthy controls and/or patients, and take metabolic samples which would demonstrate what metabolites in the plasma are taken up by the cells and in what quantities. The metabolome obtained might be more specific to ECs but then again these measurements would be *in vitro* while the plasma metabolomics datasets used in this thesis were generated from *in vivo* measurements of human blood plasma. This is probably one of the hardest aspects of modelling we have come by thus far. These kinds of measurements would be used to generate metabolic constraints for an endothelial model. Another option would be to design a multi-compartment model representing multiple cell types.

Further research could focus on the modelling process, by generating a more relevant endothelial model by constructing it around another cell type and establishing a flow model to generate metabolic constraints to impose on the model. The model could also be improved by conducting plasma experiments in an effort to obtain a more realistic image of the utilization of plasma metabolites by ECs. Furthermore, the results of metabolic experiments conducted for this thesis could be used to generate catecholamine-specific constraints and impose on the model, making the trauma patient model more specific to metabolic alterations caused by increased circulatory catecholamines. The same methodology has been utilized in our lab, where HUVECs in culture were stimulated with LPS and IFNγ, metabolic data collected and imposed as constraints to generate a sepsis GEM(49).

The model curation could be expanded by fixing reactions such as the wrongly directed glycolysis reaction and more reactions that do not reflect metabolism *in vivo*. Constraints for pyruvate could be added to the model by measuring uptake of pyruvate from the medium, since we do know that the cells are doing so.

The very high throughput and reliable detection method of mass spectrometry was used to analyse intracellular metabolic samples. The magnitude of differences in measurements of metabolites might not seem so great as the closest differences observed are on the scale of 0,1 or less. This in fact is a real difference and mass spectrometry research with similar or less differences have been published in well-established journals such as Cell Metabolism(78).

The effects of catecholamine stimulation on the EGL phenotype could be investigated further by quantitatively measuring EGL components after catecholamine stimulation using a kit such as the Blyscan assay(49). The EGL biomass was calculated to be 5% out of the total biomass weight in the model by literature review. That being said, the EGL is a constantly changing structure that makes its final quantitation not possible, which is why we decided to define it in terms of building block ratios. These ratios could be made clearer by using the Blyscan kit. In the light of the newly demonstrated roles of endothelial FAO for maintaining barrier functions (such as compromised in trauma), using the Seahorse XF analyser to analyse FAO in catecholamine treated cells would be a great expansion of these results.

Expansion of the labelling experiments would give a clearer image as to what is happening in EC metabolism under catecholamine stimulation. The ^{15}N-2 labelling of arginine would allow to investigate the rate of NO synthesis and the same labelling of aspartate would give more information on the TCA cycle anaplerosis as aspartate can be converted into oxaloacetate and shunted into the TCA cycle (anaplerosis).

Extracellular amino acids could be measured by another methods to confirm that extracellular levels of glutamine increase as a response to catecholamines. Other amino acids could be measured to investigate which amino acids the cells are oxidizing (utilization of carbon skeletons in the TCA cycle and NH_4^+ in amino group metabolism), and weather the utilization of glycine changes with catecholamine stimulation.

As mentioned before, glycolytic activity could be haltered by catecholamine stimulation and the subsequent cAMP increase which results in the inhibition of PKM2, which normally maintains vascular permeability by blocking NF-kB and inhibiting release of angiopoietin-2(70). This mechanism proposes a link between catecholamine stimulation, the decrease of glycolytic flux and increased endothelial permeability. This link could be investigated by measuring the release of angiopoietin-2 and NF-kB after catecholamine stimulation by probing techniques.

6 Conclusions

The work presented in this thesis indicated that catecholamine stimulation resulted in changes to endothelial metabolism as far as energy- and signalling metabolism, glycolytic and TCA cycle activity, and EGL metabolism. It also indicated that the iEC2997 combined with the utilization of plasma metabolomics data did provide adequate predictive power into dysfunctional EC metabolism.

First, we set out to decide if increased catecholamine resulted in changes to endothelial metabolism, and particularly to examine if they exerted their effects on EGL metabolism. We conclude that catecholamine stimulation effects energy metabolism by decrease in intracellular ATP, possibly via decreased glycolytic activity. We furthermore conclude that catecholamine stimulation results in decreased glycolytic and TCA cycle activity, but we do not assert anything on the mechanisms involved. Last but certainly not least we conclude that synthesis rates of the EGL precursors UDP-glucose and UDP-N-acetylglucosamine decrease after the first 4 hours of catecholamine stimulation, and that they do recover with time. We conclude that this initial decrease in synthesis is enough to decrease intracellular concentrations. Again, we do not conclude anything on the mechanisms behind these alterations.

Secondly, we set out to decide if differences in plasma metabolomics between trauma patients and healthy controls could influence EC metabolism, and specifically EGL metabolism. We conclude that the plasma metabolomics data were indeed usable to construct predictive trauma patient and healthy control models, as model analysis did in many cases concur with results from metabolic experiments. Furthermore, we conclude that the plasma metabolomics profiles of trauma patients resembles metabolism of catecholamine stimulated cells *in vitro*.

References

1. Deanfield JE, Halcox JP, Rabelink TJ. Endothelial Function and Dysfunction. *Circulation*. 2007 Mar 13;115(10):1285–95.
2. Reitsma S, Slaaf DW, Vink H, van Zandvoort MAMJ, oude Egbrink MGA. The endothelial glycocalyx: composition, functions, and visualization. *Pflugers Arch*. 2007 Jun;454(3):345–59.
3. Chappell D, Jacob M, Hofmann-Kiefer K, Rehm M, Welsch U, Conzen P, et al. Antithrombin reduces shedding of the endothelial glycocalyx following ischaemia/reperfusion. *Cardiovasc Res*. 2009 Jul 15;83(2):388–96.
4. Rehm M, Zahler S, Lötsch M, Welsch U, Conzen P, Jacob M, et al. Endothelial glycocalyx as an additional barrier determining extravasation of 6% hydroxyethyl starch or 5% albumin solutions in the coronary vascular bed. *Anesthesiology*. 2004 May;100(5):1211–23.
5. Jacob M, Bruegger D, Rehm M, Welsch U, Conzen P, Becker BF. Contrasting effects of colloid and crystalloid resuscitation fluids on cardiac vascular permeability. *Anesthesiology*. 2006 Jun;104(6):1223–31.
6. Rahbar E, Cardenas JC, Baimukanova G, Usadi B, Bruhn R, Pati S, et al. Endothelial glycocalyx shedding and vascular permeability in severely injured trauma patients. *J Transl Med*. 2015 Dec 12;13(117):1–7.
7. Eelen G, de Zeeuw P, Simons M, Carmeliet P. Endothelial Cell Metabolism in Normal and Diseased Vasculature. *Circ Res*. 2015 Mar 27;116(7):1231–44.
8. Florian JA, Kosky JR, Ainslie K, Pang Z, Dull RO, Tarbell JM. Heparan Sulfate Proteoglycan Is a Mechanosensor on Endothelial Cells. *Circ Res*. 2003 Nov 14;93(10):e136-42.
9. Mochizuki S, Vink H, Hiramatsu O, Kajita T, Shigeto F, Spaan JAE, et al. Role of hyaluronic acid glycosaminoglycans in shear-induced endothelium-derived nitric oxide release. *Am J Physiol Circ Physiol*. 2003 Aug;285(2):H722–6.
10. Alberich R, Castro JA, Llabrés M, Palmer-Rodríguez P. Metabolomics analysis: Finding out metabolic building blocks. *PLoS One*. 2017;12(5):e0177031.
11. Kalucka J, Bierhansl L, Conchinha NV, Missiaen R, Elia I, Brüning U, et al. Quiescent Endothelial Cells Upregulate Fatty Acid β-Oxidation for Vasculoprotection via Redox Homeostasis. *Cell Metab*. 2018 Dec 4;28(6):881–894.e13.
12. Patella F, Schug ZT, Persi E, Neilson LJ, Erami Z, Avanzato D, et al. Proteomics-Based Metabolic Modeling Reveals That Fatty Acid Oxidation (FAO) Controls Endothelial Cell (EC) Permeability. *Mol Cell Proteomics*. 2015 Mar;14(3):621–34.
13. Zhu Z, Shi Z, Xie C, Gong W, Hu Z, Peng Y. A novel mechanism of Gamma-aminobutyric acid (GABA) protecting human umbilical vein endothelial cells (HUVECs) against H2O2-induced oxidative injury. *Comp Biochem Physiol Part C Toxicol Pharmacol*. 2019 Mar;217:68–75.
14. Sen S, Roy S, Bandyopadhyay G, Scott B, Xiao D, Ramadoss S, et al. γ-Aminobutyric Acid Is Synthesized and Released by the Endothelium. *Circ Res*. 2016 Aug 19;119(5):621–34.

15. Giacco F, Brownlee M. Oxidative Stress and Diabetic Complications. Schmidt AM, editor. *Circ Res*. 2010 Oct 29;107(9):1058–70.

16. Rajendran P, Rengarajan T, Thangavel J, Nishigaki Y, Sakthisekaran D, Sethi G, et al. The Vascular Endothelium and Human Diseases. *Int J Biol Sci*. 2013;9(10):1057–69.

17. Johansson P, Stensballe J, Ostrowski S. Shock induced endotheliopathy (SHINE) in acute critical illness - a unifying pathophysiologic mechanism. *Crit Care*. 2017 Dec 9;21(1):25.

18. Dennis JW, Nabi IR, Demetriou M. Metabolism, Cell Surface Organization, and Disease. *Cell*. 2009 Dec 24;139(7):1229–41.

19. Giantsos-Adams KM, Koo AJ-A, Song S, Sakai J, Sankaran J, Shin JH, et al. Heparan Sulfate Regrowth Profiles Under Laminar Shear Flow Following Enzymatic Degradation. *Cell Mol Bioeng*. 2013 Jun 20;6(2):160–74.

20. Becker BF, Jacob M, Leipert S, Salmon AHJ, Chappell D. Degradation of the endothelial glycocalyx in clinical settings: searching for the sheddases. *Br J Clin Pharmacol*. 2015 Sep;80(3):389–402.

21. Nelson A, Berkestedt I, Schmidtchen A, Ljunggren L, Bodelsson M. Increased levels of glycosaminoglycans during septic shock: relation to mortality and the antibacterial actions of plasma. *Shock*. 2008 Dec;30(6):623–7.

22. Lukasz A, Hillgruber C, Oberleithner H, Kusche-Vihrog K, Pavenstädt H, Rovas A, et al. Endothelial glycocalyx breakdown is mediated by angiopoietin-2. *Cardiovasc Res*. 2017 May 1;113(6):671–80.

23. Sorriento D, Trimarco B, Iaccarino G. Adrenergic mechanism in the control of endothelial function. *Transl Med @ UniSa*. 2011 Sep;1:213–28.

24. Jensen BC, Swigart PM, Montgomery MD, Simpson PC. Functional alpha-1B adrenergic receptors on human epicardial coronary artery endothelial cells. *Naunyn Schmiedebergs Arch Pharmacol*. 2010 Dec 22;382(5–6):475–82.

25. SPINDLER V, WASCHKE J. Beta-Adrenergic Stimulation Contributes to Maintenance of Endothelial Barrier Functions Under Baseline Conditions. *Microcirculation*. 2011 Feb;18(2):118–27.

26. van Mourik JA, Romani de Wit T, Voorberg J. Biogenesis and exocytosis of Weibel-Palade bodies. *Histochem Cell Biol*. 2002 Feb 19;117(2):113–22.

27. Fiedler U, Scharpfenecker M, Koidl S, Hegen A, Grunow V, Schmidt JM, et al. The Tie-2 ligand Angiopoietin-2 is stored in and rapidly released upon stimulation from endothelial cell Weibel-Palade bodies. *Blood*. 2004 Jun 1;103(11):4150–6.

28. Ostrowski SR, Pedersen SH, Jensen JS, Mogelvang R, Johansson PI. Acute myocardial infarction is associated with endothelial glycocalyx and cell damage and a parallel increase in circulating catecholamines. *Crit Care*. 2013 Feb 22;17(R32):1–12.

29. Nioi P, Sigurdsson A, Thorleifsson G, Helgason H, Agustsdottir AB, Norddahl GL, et al. Variant ASGR1 Associated with a Reduced Risk of Coronary Artery Disease. *N Engl J Med*.

2016/05/19. 2016;374(22):2131–41.

30. Palsson B. Metabolic systems biology. *FEBS Lett*. 2009 Dec 17;583(24):3900–4.

31. Becker SA, Feist AM, Mo ML, Hannum G, Palsson BØ, Herrgard MJ. Quantitative prediction of cellular metabolism with constraint-based models: the COBRA Toolbox. *Nat Protoc*. 2007 Mar 1;2(3):727–38.

32. Duarte NC, Becker SA, Jamshidi N, Thiele I, Mo ML, Vo TD, et al. Global reconstruction of the human metabolic network based on genomic and bibliomic data. *Proc Natl Acad Sci U S A*. 2007 Feb 6;104(6):1777–82.

33. Brunk E, Sahoo S, Zielinski DC, Altunkaya A, Dräger A, Mih N, et al. Recon3D enables a three-dimensional view of gene variation in human metabolism. *Nat Biotechnol*. 2018;36(3):272–81.

34. Vlassis N, Pacheco MP, Sauter T. Fast Reconstruction of Compact Context-Specific Metabolic Network Models. Ouzounis CA, editor. *PLoS Comput Biol*. 2014 Jan 16;10(1):e1003424.

35. Mardinoglu A, Shoaie S, Bergentall M, Ghaffari P, Zhang C, Larsson E, et al. The gut microbiota modulates host amino acid and glutathione metabolism in mice. *Mol Syst Biol*. 2015 Oct 16;11(10):1–15.

36. Gatto F, Nielsen J. In search for symmetries in the metabolism of cancer. *Wiley Interdiscip Rev Syst Biol Med*. 2016 Jan;8(1):23–35.

37. Gatto F, Miess H, Schulze A, Nielsen J. Flux balance analysis predicts essential genes in clear cell renal cell carcinoma metabolism. *Sci Rep*. 2015 Sep 4;5(1):10738.

38. Jerby-Arnon L, Pfetzer N, Waldman YY, McGarry L, James D, Shanks E, et al. Predicting Cancer-Specific Vulnerability via Data-Driven Detection of Synthetic Lethality. *Cell*. 2014 Aug 28;158(5):1199–209.

39. Agren R, Mardinoglu A, Asplund A, Kampf C, Uhlen M, Nielsen J. Identification of anticancer drugs for hepatocellular carcinoma through personalized genome-scale metabolic modeling. *Mol Syst Biol*. 2014 Mar 28;10(721):1–13.

40. Mardinoglu A, Agren R, Kampf C, Asplund A, Uhlen M, Nielsen J. Genome-scale metabolic modelling of hepatocytes reveals serine deficiency in patients with non-alcoholic fatty liver disease. *Nat Commun*. 2014 Dec 14;5(3083):1–11.

41. Väremo L, Scheele C, Broholm C, Mardinoglu A, Kampf C, Asplund A, et al. Proteome- and Transcriptome-Driven Reconstruction of the Human Myocyte Metabolic Network and Its Use for Identification of Markers for Diabetes. *Cell Rep*. 2015 May 12;11(6):921–33.

42. Shoaie S, Karlsson F, Mardinoglu A, Nookaew I, Bordel S, Nielsen J. Understanding the interactions between bacteria in the human gut through metabolic modeling. *Sci Rep*. 2013 Dec 28;3(2532).

43. Mardinoglu A, Agren R, Kampf C, Asplund A, Nookaew I, Jacobson P, et al. Integration of clinical data with a genome-scale metabolic model of the human adipocyte. *Mol Syst Biol*. 2014 Apr 28;9(649):1–15.

44. Fouladiha H, Marashi S-A. Biomedical applications of cell- and tissue-specific metabolic

network models. *J Biomed Inform*. 2017 Apr 1;68:35–49.

45. Orth JD, Thiele I, Palsson BØ. What is flux balance analysis? *Nat Biotechnol*. 2010 Mar;28(3):245–8.

46. Feist AM, Palsson BO. The biomass objective function. *Curr Opin Microbiol*. 2010 Jun 1;13(3):344–9.

47. Schellenberger J, Palsson BØ. Use of Randomized Sampling for Analysis of Metabolic Networks. *J Biol Chem*. 2009 Feb 27;284(9):5457–61.

48. Segrè D, Vitkup D, Church GM. Analysis of optimality in natural and perturbed metabolic networks. *Proc Natl Acad Sci U S A*. 2002 Nov 12;99(23):15112–7.

49. McGarrity S, Anuforo Ó, Halldórsson H, Bergmann A, Halldórsson S, Palsson S, et al. Metabolic systems analysis of LPS induced endothelial dysfunction applied to sepsis patient stratification. *Sci Rep*. 2018 Dec 1;8(1):6811.

50. Kanehisa M, Goto S. KEGG: kyoto encyclopedia of genes and genomes. *Nucleic Acids Res*. 2000 Jan 1;28(1):27–30.

51. King ZA, Lu J, Dräger A, Miller P, Federowicz S, Lerman JA, et al. BiGG Models: A platform for integrating, standardizing and sharing genome-scale models. *Nucleic Acids Res*. 2016 Jan 4;44(D1):D515–22.

52. Schellenberger J, Que R, Fleming RMT, Thiele I, Orth JD, Feist AM, et al. Quantitative prediction of cellular metabolism with constraint-based models: the COBRA Toolbox v2.0. *Nat Protoc*. 2011 Sep 4;6(9):1290–307.

53. Swainston N, Smallbone K, Hefzi H, Dobson PD, Brewer J, Hanscho M, et al. Recon 2.2: from reconstruction to model of human metabolism. *Metabolomics*. 2016 Jul 7;12(7):109.

54. Hefzi H, Ang KS, Hanscho M, Bordbar A, Ruckerbauer D, Lakshmanan M, et al. A Consensus Genome-scale Reconstruction of Chinese Hamster Ovary Cell Metabolism. *Cell Syst*. 2016 Nov 23;3(5):434–443.e8.

55. Klein NJ, Shennan GI, Heyderman RS, Levin M. Alteration in glycosaminoglycan metabolism and surface charge on human umbilical vein endothelial cells induced by cytokines, endotoxin and neutrophils. *J Cell Sci*. 1992 Aug;102 (Pt 4:821–32.

56. Han J, Zhang F, Xie J, Linhardt RJ, Hiebert LM. Changes in cultured endothelial cell glycosaminoglycans under hyperglycemic conditions and the effect of insulin and heparin. *Cardiovasc Diabetol*. 2009 Aug 20;8(1):46.

57. Ramasamy S, Lipke DW, McClain CJ, Hennig B. Tumor necrosis factor reduces proteoglycan synthesis in cultured endothelial cells. *J Cell Physiol*. 1995 Jan;162(1):119–26.

58. Arisaka T, Mitsumata M, Kawasumi M, Tohjima T, Hirose S, Yoshida Y. Effects of shear stress on glycosaminoglycan synthesis in vascular endothelial cells. *Ann N Y Acad Sci*. 1995 Jan 17;748:543–54.

59. Gouverneur M, Spaan JAE, Pannekoek H, Fontijn RD, Vink H. Fluid shear stress stimulates incorporation of hyaluronan into endothelial cell glycocalyx. *Am J Physiol Circ Physiol*. 2006

Jan;290(1):H458–H452.

60. Alavi M, Moore S. Glycosaminoglycan composition and biosynthesis in the endothelium-covered neointima of de-endothelialized rabbit aorta. *Exp Mol Pathol*. 1985 Jun;42(3):389–400.

61. Robinson J, Gospodarowicz D. Glycosaminoglycans synthesized by cultured bovine corneal endothelial cells. *J Cell Physiol*. 1983 Dec;117(3):368–76.

62. Kobayashi M, Shimada K, Ozawa T. Human Platelet-Derived Transforming Growth Factor-β Stimulates Synthesis of Glycosaminoglycans in Cultured Porcine Aortic Endothelial Cells. *Gerontology*. 1992;38(1):36–42.

63. Knudson W, Subbaiah S, Pauli BU. Proteoglycan synthesis by normal and neoplastic human transitional epithelial cells. *J Cell Biochem*. 1990 Jul;43(3):265–79.

64. Bar RS, Dake BL, Spanheimer RG. Sulfated glycosaminoglycans in cultured endothelial cells from capillaries and large vessels of human and bovine origin. *Atherosclerosis*. 1985 Jul;56(1):11–26.

65. Sörensson J, Björnson A, Ohlson M, Ballermann BJ, Haraldsson B. Synthesis of sulfated proteoglycans by bovine glomerular endothelial cells in culture. *Am J Physiol Physiol*. 2003 Feb;284(2):F373–80.

66. Datta PK, Deshmane S, Khalili K, Merali S, Gordon JC, Fecchio C, et al. Glutamate metabolism in HIV-1 infected macrophages: Role of HIV-1 Vpr. *Cell Cycle*. 2016 Sep;15(17):2288–98.

67. Gao MH, Lai ; N Chin, Roth DM, Zhou J, Zhu J, Anzai T, et al. Adenylylcyclase Increases Responsiveness to Catecholamine Stimulation in Transgenic Mice. *Circulation*. 1999;99(12):1618–22.

68. Wiktorowska-Owczarek A, Namiecińska M, Berezińska M, Nowak JZ. Characteristics of adrenaline-driven receptor-mediated signals in human microvessel-derived endothelial cells. *Pharmacol Rep*. 2008;60(6):950–6.

69. Kawaguchi T, Takenoshita M, Kabashima T, Uyeda K. Glucose and cAMP regulate the L-type pyruvate kinase gene by phosphorylation/dephosphorylation of the carbohydrate response element binding protein. *Proc Natl Acad Sci U S A*. 2001 Nov 20;98(24):13710–5.

70. Kim B, Jang C, Dharaneeswaran H, Li J, Bhide M, Yang S, et al. Endothelial pyruvate kinase M2 maintains vascular integrity. *J Clin Investig*. 2018 Sep 17;128(10):4543–56.

71. Barth E, Albuszies G, Baumgart K, Matejovic M, Wachter U, Vogt J, et al. Glucose metabolism and catecholamines. *Crit Care Med*. 2007 Sep;35(9):S508–18.

72. Li Y, Chang Y, Ye N, Chen Y, Zhang N, Sun Y. Advanced glycation end products-induced mitochondrial energy metabolism dysfunction alters proliferation of human umbilical vein endothelial cells. *Mol Med Rep*. 2017 May 1;15(5):2673–80.

73. Kuosmanen SM, Kansanen E, Kaikkonen MU, Sihvola V, Pulkkinen K, Jyrkkänen H-K, et al. NRF2 regulates endothelial glycolysis and proliferation with miR-93 and mediates the effects of oxidized phospholipids on endothelial activation. *Nucleic Acids Res*. 2018 Feb 16;46(3):1124–

38.

74. Suárez J, Rubio R. Regulation of glycolytic flux by coronary flow in guinea pig heart. Role of vascular endothelial cell glycocalyx. *Am J Physiol*. 1991 Dec;261(6):H1994-2000.

75. Pochini L, Scalise M, Galluccio M, Indiveri C. Membrane transporters for the special amino acid glutamine: structure/function relationships and relevance to human health. *Front Chem*. 2014;2(61).

76. Addabbo F, Ratliff B, Park H-C, Kuo M-C, Ungvari Z, Ciszar A, et al. The Krebs Cycle and Mitochondrial Mass Are Early Victims of Endothelial Dysfunction. *Am J Pathol*. 2009 Jan;174(1):34–43.

77. Zhong Q, Li X, Nong Q, Mao B, Pan X. Metabolic Profiling in Association with Vascular Endothelial Cell Dysfunction Following Non-Toxic Cadmium Exposure. *Int J Mol Sci*. 2017 Sep 5;18(9).

78. Kalucka J, Bierhansl L, Conchinha NV, Missiaen R, Elia I, Brüning U, et al. Quiescent Endothelial Cells Upregulate Fatty Acid β-Oxidation for Vasculoprotection via Redox Homeostasis. *Cell Metab*. 2018 Dec 4;28(6):881–894.e13.

79. Wylie E, Foster R, Salmon A, Satchell S. Role of the endothelial glycocalyx in kidney disease and vascular dysfunction. *Lancet (London, England)*. 2014 Feb 26;383(112).

80. Bröer A, Wagner CA, Lang F, Bröer S. The heterodimeric amino acid transporter 4F2hc/y+LAT2 mediates arginine efflux in exchange with glutamine. *Biochem J*. 2000 Aug 1;349(3):787–95.

81. Wilkerson BA, Argraves KM. The role of sphingosine-1-phosphate in endothelial barrier function. *Biochim Biophys Acta*. 2014 Oct;1841(10):1403–12.

82. Xiong Y, Hla T. S1P control of endothelial integrity. *Curr Top Microbiol Immunol*. 2014;378:85–105.

83. Chu L-Y, Wang Y-F, Cheng H-H, Kuo C-C, Wu KK. Endothelium-Derived 5-Methoxytryptophan Protects Endothelial Barrier Function by Blocking p38 MAPK Activation. Fu J, editor. *PLoS One*. 2016 Mar 22;11(3):e0152166.

84. Wang Y-F, Hsu Y-J, Wu H-F, Lee G-L, Yang Y-S, Wu J-Y, et al. Endothelium-Derived 5-Methoxytryptophan Is a Circulating Anti-Inflammatory Molecule That Blocks Systemic Inflammation. *Circ Res*. 2016 Jul 8;119(2):222–36.

85. Wang Y, Liu H, McKenzie G, Witting PK, Stasch J-P, Hahn M, et al. Kynurenine is an endothelium-derived relaxing factor produced during inflammation. *Nat Med*. 2010 Mar 28;16(3):279–85.

86. Cai W, Duan X-M, Liu Y, Yu J, Tang Y-L, Liu Z-L, et al. Uric Acid Induces Endothelial Dysfunction by Activating the HMGB1/RAGE Signaling Pathway. *Biomed Res Int*. 2017;2017:4391920.

87. So A, Thorens B. Uric acid transport and disease. *J Clin Invest*. 2010 Jun;120(6):1791–9.

88. Ding Y, Svingen GFT, Pedersen ER, Gregory JF, Ueland PM, Tell GS, et al. Plasma Glycine

and Risk of Acute Myocardial Infarction in Patients With Suspected Stable Angina Pectoris. *J Am Heart Assoc*. 2016 Jan 13;5(1):e002621.

89. Hitzel J, Lee E, Zhang Y, Bibli SI, Li X, Zukunft S, et al. Oxidized phospholipids regulate amino acid metabolism through MTHFD2 to facilitate nucleotide release in endothelial cells. *Nat Commun*. 2018 Dec 12;9(2262).

90. Alphonsus CS, Rodseth RN. The endothelial glycocalyx: a review of the vascular barrier. *Anaesthesia*. 2014 Jul;69(7):777–84.

91. Gill SE, Taneja R, Rohan M, Wang L, Mehta S. Pulmonary Microvascular Albumin Leak Is Associated with Endothelial Cell Death in Murine Sepsis-Induced Lung Injury In Vivo. *PLoS One*. 2014;9(2):e88501.

Supplementary data / published articles

The supplementary data can be requested from Rósa Sigurðardóttir (rss10@hi.is / rosasig1993@gmail.com) or Óttar Rolfsson (ottarr@hi.is).

An article where iEC2997 was utilized has been accepted for publication in Annals of surgery and is awaiting publication.